NORTHWESTERN UNIVERSITY

Use of Complementary Approaches to Imaging Biomolecules and Endogenous and Exogenous Trace Elements and Nanoparticles in Biological Samples

A DISSERTATION

SUBMITTED TO THE GRADUATE SCHOOL
IN PARTIAL FULFILLMENT OF THE REQUIREMENTS

for the degree

DOCTOR OF PHILOSOPHY

Field of Driskill Graduate Program in the Life Sciences

By

Koshonna Dinettia Brown

EVANSTON, ILLINOIS

December 2017

ABSTRACT

Use of Complementary Approaches to Imaging Biomolecules and Endogenous and Exogenous Trace Elements and Nanoparticles in Biological Samples

Koshonna Brown

X-ray Fluorescence Microscopy (XFM) is a useful technique for study of biological samples. XFM was used to map and quantify endogenous biological elements as well as exogenous materials in biological samples, such as the distribution of titanium dioxide (TiO_2) nanoparticles. TiO_2 nanoparticles are produced for many different purposes, including development of therapeutic and diagnostic particles for cancer detection and treatment, drug delivery, and induction of DNA breaks. Delivery of such nanoparticles can be targeted to specific cells and subcellular structures. In this work, we develop two novel approaches to stain TiO_2 nanoparticles for optical microscopy and to confirm that staining by XFM. The first approach utilizes fluorescent biotin and fluorescent streptavidin to label the nanoparticles before and after cellular uptake; the second approach is based on the copper-catalyzed azide–alkyne cycloaddition, the so-called CLICK chemistry, for labeling of azide conjugated TiO_2 nanoparticles with "clickable" dyes such as alkyne Alexa Fluor dyes with a high fluorescent yield. To confirm that the optical fluorescence signals of nanoparticles stained *in situ* match the distribution of the Ti element, we used high resolution synchrotron X-Ray Fluorescence Microscopy (XFM) using the Bionanoprobe instrument at the Advanced Photon Source at Argonne National Laboratory. Titanium-specific X-ray fluorescence showed excellent overlap with the location of Alexa Fluor optical fluorescence detected by confocal microscopy. In this

work XFM was also used to investigate native elemental differences between two different types of head and neck cancer, one associated with human papilloma virus infection, the other virus free. Future work may see a cross between these themes, for example, exploration of TiO_2 nanoparticles as anticancer treatment for these two different types of head and neck cancer.

ACKNOWLEDGEMENTS

First and most importantly, I would like to thank Dr. Gayle Woloschak, for being a mentor, an advisor, and an all-around exceptional human being. You have embraced me in a way that I never knew was possible. Thank you for supporting me and standing by my side through some of the most challenging moments in life and in this program. It is because of you that I am able to enter the ranks of the academy and I will be forever grateful for you. I only hope that I am able to give to someone all that you have to me over this last decade. Secondly, I want to thank Tatjana Paunesku or Tanja as we all call you. You have been a God send. Thanks for all your assistance, life lessons, discussions, encouragement, and (most importantly) your psychic coffee ground readings. I probably don't show it or say it enough, but I really do appreciate you and am eternally grateful for your support. I hope you're okay with having me in your life forever because I intend to stay.

To my committee-I still think this may have been the one decision I made in graduate school that didn't turn out to be a disaster. Brian, you have challenged me to dig deep and never settled for whatever half-baked answer or explanation I gave you and for that I thank you. Thank you for being a candid open voice I could speak to over the years. I really appreciate you fighting for me when I wasn't in the room and never letting me settle for less. I still wonder at times what this whole experience would have been like if you would have let me join your lab and play with your new microscope. Leong, there just aren't enough words to express how much I truly appreciate your expertise, support and honesty. Dr. Bergan you have been immensely helpful and thank you for stepping into such a precarious situation and providing much needed stability and guidance.

To former Wololabers, Ye and Will, thanks for answering my frantic questions about nanoparticles and characterization techniques. Ruben and Ben thanks for being great conference buddies. Ruben thanks for just being who you are, in all of your magnificence. Who will I discuss my reality TV show additions with now? Beau thank you for being a breath of fresh air in the lab and taking care of all my orders and tissue sectioning; I really appreciate it. Shout out to Carissa, Alia, Sumita, and Salida thanks for being great labmates. Big thanks also to Kate Poropatich and Barat Mittal for making it possible to investigate head and neck cancer patient samples and include these data into this thesis.

A special thank you to Judy Brown, Adam Goodman, Marshall Lindsey, Joanna Walker, Kesi Mercano, Amirah Sevilla, Nyron Crawford, Sheena Baskin, Inez Moore, and all my friends who have heard all my gripes over the years. Thank you all for the encouragement and heart felt words. To Kyle Laster, I know you'll never read this and you'll probably shake your head that I even included you in something you'll never read, but I want you to know that you mean that much to me that I mentioned you even though you could care less.

Most of all, thank you Mom for believing in me and never letting me punk out (as you would say). I know the whole process came with a lot tears that you never wanted to hear, since you only wanted to hear solutions. I hope by finishing this chapter in life I have in some way made you proud. Thank you for instilling in me an immeasurable amount of strength, grace, and character. I think you were the originator of "when they go low, we go high" (no offense Michelle Obama), but mom you were the personification of this phrase every day of your life and I assure you that I will continue to live life as you would have wanted for me. To you I dedicate this thesis.

LIST OF COMMONLY USED ABREVIATIONS

ANL	Argonne National Laboratory
APS	Advanced Photon Source
DLS	Dynamic Light scattering
DNA	Deoxyribonucleic Acid
DOPA	Dopamine
DOPAC	3,4-dihydroxyphenylacetic acid
DOX	Doxorubicin
DOX NC	Doxorubicin Nanoconjugate
e^-	Electron
h^+	Electropositive hole (electron vacancy)
ICP-MS	Inductively coupled plasma-mass spectrometry
MR	Magnetic resonance
MRI	Magnetic resonance imaging
NP	Nanoparticle
PBS	Phosphate Buffered Saline
PEG	Polyethylene Glycol
RNA	Ribonucleic Acid
ROS	Reactive Oxygen Species
TEM	Transmission Electron Microscopy
TiO_2	Titanium Dioxide
UV	Ultraviolet
XFM	X-ray Fluorescence Microscopy
BNP	Bionanoprobe

TABLE OF CONTENTS

LIST OF TABLES AND FIGURES

CHAPTER 1: Introduction

1.1 TiO_2 Nanoparticles

The bulk form of titanium dioxide (TiO_2) is inert; however, nanoparticles made of this material are not: particle sizes below 20 nm result in surface instability that confers chemical reactivity to the TiO_2 nanoparticles[1-4]. Specifically, bulk forms of TiO_2 have their surface titanium atoms in a hexa-coordinated geometry, but in nanoparticles 20 nm or less in size, the geometry of surface titanium atoms becomes penta-coordinated and highly reactive. This makes titanium atoms on the nanoparticle surface very reactive, especially for binding with catechols[4-6]. An especially high affinity covalent bond is created between the nanoparticles and enediol ligands (e.g. alizarin, dopamine) thereby forming stable complexes. This unique feature has been exploited in coating these nanoparticles with various agents[1, 3, 4, 7-21].

Titanium dioxide has many useful photophysical properties, most especially photocatalytic properties. The ability of titanium dioxide to act as a photocatalyst has been known for 90 years, but this was applied to biology only recently[3, 13, 20, 22]. Due to their unique photocatalytic and physical properties, TiO_2 nanoparticles and TiO_2 shell nanoparticles have been investigated for use in diagnostic assays, as gene targeting agents, radiosensitizers, and as cargo delivery vehicles[3, 7, 12, 14, 18, 19]. TiO_2 nanoparticles are especially attractive for use in cancer therapy, because they can be, for example, passively or actively targeted to neoplastic cells and then actively targeted to subcellular locations such as cell nuclei; once there, TiO_2 nanoparticles can be activated to release reactive oxygen species (ROS) that result in DNA oxidation and double stranded breaks in the genomic DNA *in situ* [13, 20].

Ionizing radiation generates reactive oxygen species (ROS) [23]. ROS can cause damage to all biological molecules - nucleic acids, proteins, sugars and lipids; in addition, ionizing radiation can also cause damage by direct energy deposition and ionization of biological molecules. Due to their short half-life in cells ROS traverse no more than 1.1 μm in aqueous solutions [24]; therefore, ROS formation close to DNA is the most damaging for cells. Both direct energy deposition and ROS lead to the formation of single and double stranded DNA breaks (DNA SSBs and DSBs); DNA breaks are handled by an extensive cellular repair machinery. Misrepaired or unrepaired DNA damage can lead to cell death via apoptosis, autophagy, necrosis, or mitotic catastrophe. In addition, ROS react with cellular lipids and proteins often leading to the loss of membrane integrity and cell death [25, 26]. The presence of nanomaterials in cells can perturb the biological, physical, and/or chemical outcomes of radiation or the cellular capacity to repair radiation-induced damage leading to nanoparticle-mediated radiosensitization. Furthermore, nanoparticles can enhance the effects of radiation by producing additional ROS or free electrons or electropositive holes on their own, after they are exposed to photons of different energies [27]. In particular, TiO_2 is a semiconductor with a band gap of 3.2 eV, therefore its exposure to photons with incident energies greater than the band gap e.g. light of wavelengths below 388 nm, will lead to the promotion of valence band electrons (e^-) to the conduction band [28][58]. This process leaves behind electropositive holes (h^+) in the valence band that can react with molecules close to nanoparticle surface. When this occurs with water molecules adsorbed to the nanoparticle surface hydroxyl radicals ($OH\cdot$) are formed. Similarly, conduction band e^- on nanoparticle surface (electrons released from chemical bonds) can react

with molecules close to nanoparticle surface; when oxygen molecules are involved in such a reaction they yield superoxide radicals ($O_2^{\cdot -}$) [29] (Figure 1.1).

For cell-type specific nanoparticle-mediated radiosensitization, targeting of nanomaterials to specific cell types or subcellular organelles plays a significant role. While selection of best targeting moiety is in and of itself a complicated task, it should be remembered that surface modifications on nanomaterials are not static—nanomaterials accumulate and exchange components of tightly and loosely bound surface protein corona as they progress through cells and their environment [30]. The specific effect of TiO_2 activation on cells is further discussed in Chapter 4.

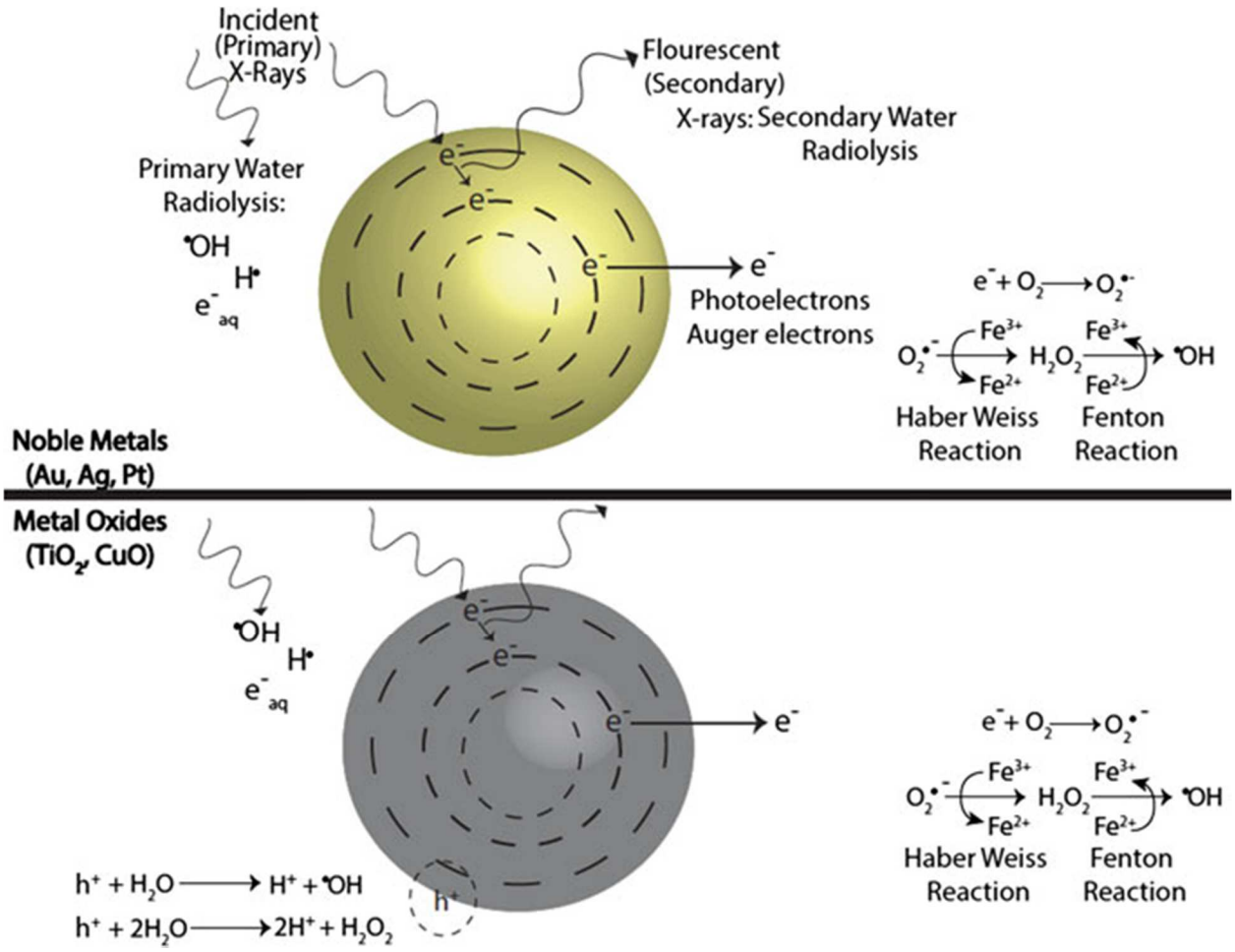

Figure 1.1 Physico-chemical events following exposure of metal and metal oxide nanoparticles to ionizing radiation (e.g. X-rays). Interaction between ionizing radiation and noble metal nanoparticles leads to production of photoelectrons and Auger electrons (e^-); these electrons are ejected from the nanoparticles as well as photons of different energies, including secondary fluorescent X-rays. Interaction between ionizing radiation and semiconductor nanoparticles leads to re-distribution and release of electrons as well as formation of reactive electropositive holes (h^+) on nanoparticle surface. Free electrons and electropositive holes on nanoparticle surface can damage cellular components directly or indirectly through production of reactive oxygen species (superoxide $O_2^{\bullet-}$, hydroxyl radical $^{\bullet}OH$, hydrogen peroxide H_2O_2) which are also formed by radiolysis of water [31].

1.2 Nanoparticle Production and Characterization

Numerous procedures for synthesis of TiO_2 nanoparticles exist. Most control over shape, crystalline phase and size of nanoparticles is provided by synthesis approaches that use organic compounds; unfortunately, the same compounds remain attached to the nanoparticle surface after synthesis. Organic materials-free methods for TiO_2 nanoparticle synthesis, on the other hand, make nanoparticles of variable sizes. A good compromise for TiO_2 nanoparticle synthesis clean from organic materials is controlled hydrolysis of $TiCl_4$ [32]. In this procedure, the most important feature important in order to achieve uniform nanoparticle size and crystalline form is careful maintenance of temperature. Abbas and others have determined that post-synthesis dialysis of nanoparticles in water while the pH gradually increases to 2.5 is the critical step for nanoparticle size "fixing". While dialysis at room temperature produces nanoparticles larger than 20 nm, dialysis at 5°C produces nanoparticles of 15±3 nm and dialysis at 0°C produces nanoparticles of smaller than 10 nm [32]. Nanoparticles prepared for work presented here were dialyzed at 1°C and nanoparticle size was 5 nm on average, with anatase crystal structure. This structure was not changed when nanoparticles were coated by dopamine-biotin, for example, as established by nanoparticle imaging with high resolution TEM and by diffraction (Figure 1.2).

In order to evaluate the appearance of nanoparticles in aqueous solution, and to compare naked and coated nanoparticles, cryo-TEM imaging was done as well. This work constitutes part of the manuscript Brown et al 2017 [33] and will be shown in Chapter 3.

a)

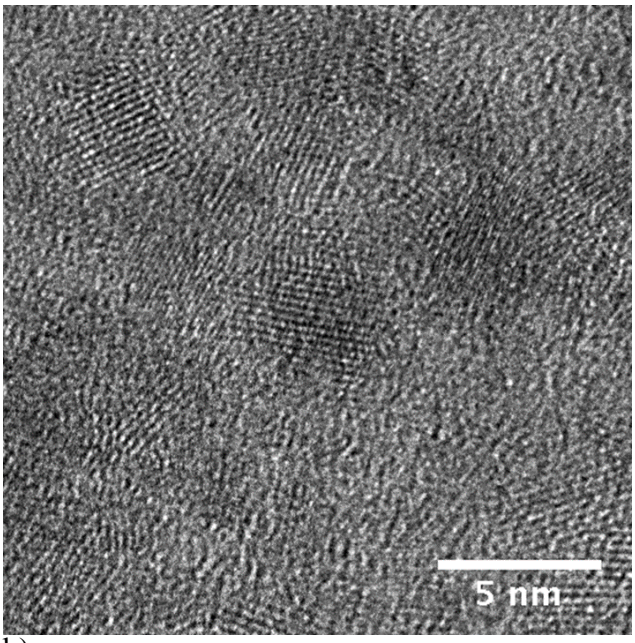

b)

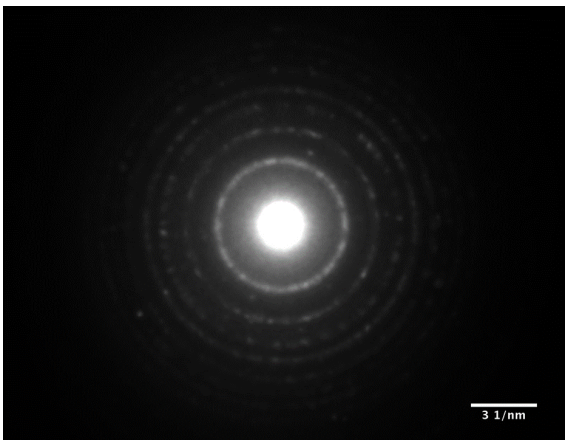

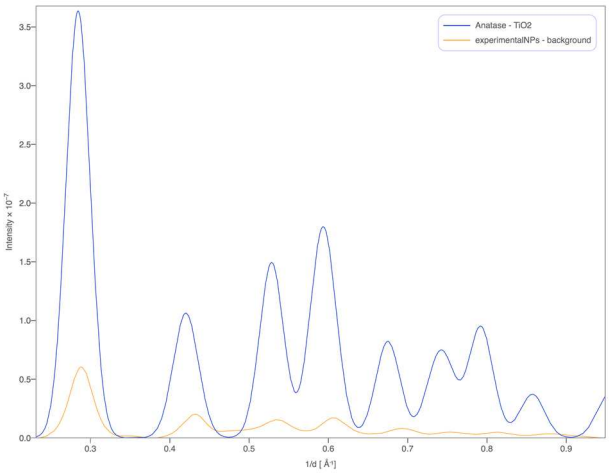

Figure 1.1 Characterization of TiO_2 nanoparticles coated with dopamine-biotin. (a) High resolution TEM shows crystalline structure of nanoparticles and size of about 5 nm; (b) Diffraction pattern of same nanoparticles and its reconstruction (orange) matches the pattern characteristic for anatase (blue) TiO_2 crystal structure. (Images courtesy of DiCorato and Smeets, joint manuscript in preparation)

The physical attributes of nanoparticles such as such as size, surface charge, metal composition and concentration are key factors that contribute to a nanomaterial's intracellular stability. As the determinates of nanoparticle behavior depend on their physical properties it is particularly important to measure and characterize each newly synthesized nanomaterial and evaluate suitability of synthesis route to maintain batch to batch reproducibility. Some of the characterization assays typically used for determining physical properties of TiO_2 nanoparticles include dynamic light scattering (DLS), zeta potential, induced-coupled particle mass spectroscopy (ICP-MS), and cryogenic-transmission election microscopy (Cryo-TEM). These techniques were used to characterize nanoparticles used in this study.

Dynamic Light Scattering measures a particles size and size distribution in aqueous solutions. This is particularly useful for nanobiotechnology work involving nanoparticles introduced to cells. DLS measures particles size through determining the mean nanoparticle size or hydrodynamic diameter in dilute aqueous suspensions. The hydrodynamic diameter is the diameter of an equivalent hard sphere that diffuses at the same rate as the analyte. Although particle size is the primary determinant of the measured diffusion coefficient, other parameters can impact these measurements and influence the measured size [34]. For example – it is known that in DLS the largest size particles or even particle aggregates dominate the readout; for that reason, DLS is used primarily to evaluate how nanoparticles behave in solution (especially after surface modifications) and not for nanoparticle sizing. Nanoparticles used in this thesis were characterized by DLS. This, however, represents part of the manuscript Brown et al 2017 [33] and these data will be shown in Chapter 3.

Zeta Potential analysis is a technique for determining the surface charge of nanoparticles in aqueous solutions. Particle surface characteristics and charge play an important role in the particle's physical state, stability in different media, agglomeration tendencies, and interaction with biological systems. Zeta potential measurement provides an indirect measure of the net charge of nanoparticles. This technique is often used as a tool to test batch-to-batch nanoparticle consistency and the effect of different nanoparticle surface coatings. Nanoparticles have a surface charge that attracts a thin layer of ions of opposite charge to the nanoparticle surface. This double layer of ions travels with the nanoparticle as it diffuses throughout the solution. The electric potential at the boundary of the double layer is known as the Zeta potential of the particles and it has values that typically range from +100 mV to -100 mV. The magnitude of the zeta potential is predictive of nanoparticle stability. Nanoparticles with Zeta Potential values greater than +25 mV or less than -25 mV typically are considered stable and unlikely to precipitate from solution. Dispersions of nanoparticles with a zeta potential value close to 0 will eventually aggregate due to Van Der Waal's inter-particle attractions [34]. Zeta Potential is an important tool for understanding the state of the nanoparticle surface and predicting the long-term stability of the nanoparticle. We used zeta potential analysis to determine nanoparticle stability after a surface modification (see Chapter 3).

ICP-MS measures the mass fractions or concentration of elements in aqueous solutions. The mass fraction of nanoparticles in a given suspension is defined as the mass of element bound into nanoparticles per mass of suspension [34]. Samples of TiO_2 nanoparticles are digested with acid, and the Ti mass fractions of solutions are measured. The mass fraction of Ti nanoparticles in each suspension is calculated as the difference between the value obtained for the

corresponding digested samples and the value obtained for the corresponding particle-free solutions. In order to establish nanoparticle concentration in experiments shown in manuscript Brown et al 2017 [33] (Chapter 3) we performed the ICP-MS evaluation of nanoparticle samples and diluted nanoparticle samples used for cell treatments (see Methods, Chapter 7).

CHAPTER 2: Elemental Mapping in Biology

(adapted from Brown, K., Paunesku, T., Chen, S., and Woloschak G. E. Elemental Mapping in Biology using X-ray Fluorescence Microscopy: A Review)

2.1 Introduction

X-ray Fluorescence Microscopy (XFM) also known as Synchrotron Radiation based X-Ray Fluorescence (SRXRF) or Microprobe Synchrotron X-ray fluorescence (mSXRF) is a technique that detects X-rays emitted by atoms irradiated with hard X-ray photons of an energy higher or equal to the binding energy of the inner shell electrons of the sample's atoms [35, 36]. The characteristic X-rays from each element in the sample are emitted and elemental K alpha and K beta X-rays produced by elements between Si and Zn are especially suited to create an elemental map of a biological sample. This elemental map is quantitative—concentrations of all different elements are detected simultaneously pixel by pixel, as the fluorescence radiation emitted is proportional to the atom's concentration within the sample. XFM imaging allows detection of metals with detection limits as low as 0.1–5 parts per million (ppm) while most other micro-analytical techniques have 10 ppm as a detection limit. Moreover, XFM recognizes chemical elements regardless of their chemical environment. While histological staining for some elements is possible and can provide detailed information, it is relatively crude and destructive; it is also often specific to the chemical speciation of an element and only semi-quantitative [37]. The sensitivity of existing histochemical staining methods is often low as they frequently detect only relatively highly concentrated metal deposits, making a detailed relative distribution of the contents impossible [38].

Customarily, X-rays sources are considered soft or hard, based on their penetrance [39]. Preferred hard X-ray energy for work with biological samples is 10 kilo electron Volts (keV) or higher. Imaging at this energy is compatible with large focal depth and penetration of 10 microns or more. At the same time, this X-ray energy excites K line fluorescence for majority of

biologically relevant trace elements. Therefore, specimens do not need to be sectioned, but can be investigated close to their natural, frozen hydrated state with cryogenic approaches, without the introduction of artificial dyes. Additionally, X-ray fluorescence is induced throughout the thickness of a whole cell and can therefore be used to quantify elements on a per cell basis and, when sample rotation is possible, provide tomographic images of whole cells as well. Many different X-ray synchrotron facilities were used for studies of biological samples presented here, such as the Advanced Photon Source (APS) and the National Synchrotron Light Source (NSLS) in the USA, the Diamond Light Source in UK, the European Synchrotron Radiation Facility (ESRF) in France, the Berliner Elektronenspeicherring-Gesellschaft für Synchrotronstrahlung (BESSY II) and the Deutsches Elektronen-Synchrotron (DESY) in Germany, the Super Photon Ring-8 GeV (SPring8) and Photon Factory in Japan, and the Shanghai Synchrotron Radiation Facilities (SSRF) in China and Australian Synchrotron (AS) .

Different instruments and sample preparation techniques were used in the studies shown here. Accurate measurement of the distribution of trace elements within cells and tissues requires that the possible elemental redistribution due to preparation does not exceed spatial resolution of the imaging instrument. Thus, sample preparation approaches that include freezing followed by imaging under cryogenic conditions allow imaging with highest resolution [20, 40, 41]. Freeze dried samples can also be well preserved, although they do not allow tomographic 3D imaging which is possible with frozen samples imaged under cryogenic conditions. Sample prepared with the use of chemical crosslinking on the other hand, always suffer from some elemental redistribution especially for most diffusible ions such as potassium (K) and calcium (Ca). Therefore, data obtained from such samples requires careful consideration and analysis [42, 43].

With regard to XFM instruments, the so-called X-ray microprobes and nanoprobes, one finds great variation of X-ray focusing approaches and focused beam spot sizes range extends from 35nm to decades of microns. Sample environments differ as well and allow sample sizes from 1x1mm to several centimeters, surrounded by anything from ambient air, to helium gas to nitrogen gas as a cryo-jet, to vacuum. Despite these apparent variations, sample imaging with all these instruments is non-destructive, allowing complementary imaging at several instruments (provided that the sample mounting approaches are compatible) as they all use hard X-rays that can penetrate samples of 10 micron thickness or more and allow true whole cell imaging without the need for sectioning.

2.2 XFM exploration of elemental concentration, distribution and translocation in differentiation and normal homeostasis

Metals and non-metal trace elements such as iron (Fe), copper (Cu), zinc (Zn), selenium (Se) etc. are essential to most forms of life. They serve as components of proteins and nucleic acids that are critical to a number of biological processes necessary for survival [42, 44-47]. These trace elements have important roles in proliferation, differentiation, and development. During cellular differentiation and biological development trace elements localize in specific areas of tissue or subcellular locations and are then redistributed; often, such redistribution signals new stage of development etc. Previous studies examining role of metals in cellular development made use of chelating techniques, or metal removal, to assess functional differences in growth and differentiation as a result of changes in metal concentration or localization. For many elements however, chelation would not be a suitable approach for exploration because of their critical cellular functions. In such cases information about different element roles may be gleaned from information about their distribution, concentration, and translocation under different circumstances. However, this information too remains largely unknown due to the lack of analytical techniques that can image elements with sufficient sensitivity and resolution. XFM provides a solution for this problem. XFM can act as a definitive *in situ* elemental imaging technique and provide data that need not be supplemented by optical microscopy with special dyes. Few examples below show how XFM can be used to monitor subcellular elemental redistribution as cells undergo differentiation as well as monitor elemental distribution in homeostasis in whole animals.

XFM was used to support immunocytochemistry investigation of human embryonic stem cells line H9. The loss of pluripotency is a key step in cellular development and differentiation of stem cells; this process is marked not only by protein expression changes but also alterations in elemental content. As H9 cells began to differentiate under the influence of retinoic acid, protein Oct4 characteristic for non-differentiated cells decreased while Zn concentration increased. This process was monitored qualitatively by fluorescent microscopy, using the dye FluoZin-3,AM and quantitatively by XFM work conducted at the APS [48]. Interestingly, high resolution XFM images in this study showed that Zn is excluded from the chromosomes of mitotic cells.

A different study investigating elemental changes in the course of cell cycle affirmed the latter finding using a mouse fibroblast cell line—NIH 3T3[49]. Moreover, a complete elemental overview of cells undergoing mitosis has shown that Cu and Fe are also excluded from the cell region with condensed mitotic chromosomes. At the same time, Cu and Zn concentrations immediately adjacent to chromosomes were shown to be higher than in the remainder of the cytoplasm.

Angiogenesis is the process of forming of blood vessels through endothelial cell division and subsequent differentiation. Growth of blood vessels is stimulated by Cu [50]; one of the earliest indications of this mechanism came from XFM studies on microvascular endothelial cells conducted at the APS. These cells were induced to mimic early angiogenesis and a shift of Cu from the nuclear periphery to the cellular periphery extended to filopodia extensions, process extensions, and cell to cell contacts during tubulogenesis. Importantly, XFM scans demonstrated that copper relocalization in these cells was not matched by distribution changes of any of the other elements [51].

In addition to their intrinsic interest, these XFM studies also opened a new area of study in elementalomics: the study of dynamic spatial regulation of transition metals such as Cu and Zn. Prior to this work only fluxes of Calcium (Ca), Potassium (K), and Sodium (Na) were considered as appropriate subjects for study of dynamic elemental regulation. Historically, Fe, Cu and Zn were considered as comparatively static. It is possible that this view was based on the inability to sensitively measure and spatially localize these metals. Traditionally, metal sensing fluorophores are used for imaging of elemental distribution in live cells by optical microscopy; however, the data produced in such studies is subject to different types of artifacts and difficult to interpret quantitatively. Often, procedures for optical imaging require a significant degree of sophistication to ensure accuracy such as, for example Ca^{++} imaging by fluorescent calcium indicators such as fura dyes [52, 53]. In other cases, the problem with metal ion imaging lies in their inaccessibility; the affinity of endogenous metalloproteins for metal atoms studied is often higher than the affinity of the metal sensing fluorophore. Thus, these compounds interact only with the cellular pool of 'free' or 'available' metal. The selectivity of optical imaging fluorophores for free copper was used in an interesting way in combination with XFM to show the differences between dynamic Cu redistribution against the backdrop of "stabile" cellular Cu associated with Cu binding proteins [54]. Coppersensor-3 is a fluorescent probe that images only labile copper pools in cells; this dye was used in combination with Ca chelator BAPTA in optical microscopy to show the interconnectedness between Ca and labile Cu. At the same time –a complete elemental overview of samples prepared in parallel for XFM provided information about distribution of all Cu in these cells, including Cu stably bound to proteins and inaccessible to Coppersensor-3 dye.

XFM was also used to examine the cellular and subcellular localization and quantity of Se during development of spermatids (male germ cells) in the course of spermatogenesis. Se is concentrated in late spermatids due to elevated levels of selenoproteins [55]. Furthermore, high-resolution scans revealed that Se is specifically enriched near the lumen side of elongating spermatids, where the tail is developed. During spermatogenesis, phosphorus is inversely correlated with Se and it was concentrated at the place where the head of the sperm forms. In mature sperm extracted from mouse testis however, Se was detectable in the head and co-localized with P and Zn. Se was also accumulated in the midpiece of the sperm tail where it co-localized with Cu and Fe. It is of interest to note that in these samples Se was well above toxic levels indicating the ability of sperm cells to handle excessive Se amounts [55].

Se differences were found to be associated with healthy ovarian follicles as well. XFM at AS was used to measure Cu, Fe, Zn, Se and Br distribution in bovine ovaries focusing on follicles at different stages of development (from pre-ovulatory to those undergoing atresia). Significant elemental differences between follicle groups were found and Se appeared to be the element with greatest concentration difference between large pre-ovulation follicles and their smaller counterparts [56]. The authors postulate that selenoprotein glutathione peroxidase 1, an innate repressor of oxidative stress, may be responsible for these differences.

Some of the medium and lower resolution XFM setups allowed imaging of whole animals and study of elemental distribution in normal organisms. For example, XFM was used at the AS to examine the distribution of K, Ca, Mn, Fe, Zn in anesthetized and immobile, whole, hydrated adult *Caenorhabditis elegans* without any additional processing. Genetically identical and developmentally synchronous animals were used to show similarity in elemental content and

distribution across specimens. For example, the anterior part of the body was enriched for Ca and Fe, while Mn enrichment was found towards the animal's posterior [57].

Similarly, XFM was used to visualize elemental distribution in whole zebrafish embryos at the APS [58, 59]. However, in these studies samples were embedded in Lowicryl K4M resin as solid substrate. This approach allowed both good preservation of elemental distribution due to low temperature during embedding process and enabled 3D imaging at room temperature. A special setup for sample rotation coupled with fast raster scanning permitted imaging of a few millimeters large sample –48h old zebrafish embryo, with X-ray beam spot of 3.5 micron over an angular space of 180 degrees at 3 degree intervals; this data was reconstructed topographically using a combination of several approaches. Ultimately, qualitatively new data was obtained, offering unique insight into the trace metal distribution at key stages of embryonic development. For example, total Zn content of the entire 48h old embryo was 8.2 ng and this information was in good agreement with prior "bulk" elemental studies. However, this study also documented a clear segregation between Zn and Fe into different parts of the animal with the highest Fe concentration in the yolk syncytial layer, for example.

Special attention should be given to studies of human tissue samples because they form a baseline against which patient samples from different diseases can be compared. A particularly interesting work with 37 samples of brain tissue from the region of substantia nigra [60] was done at BESSY II. In this work samples from healthy individuals were grouped based on age into three groups (61–70, 71–80 and 81–90 years old) and screened for P, S, Cl, K, Ca, Fe, Cu and Zn content with the idea that some of the aging related changes may be associated with gradual development of neurodegenerative diseases [60]. Interestingly, neuronal bodies and

extraneuronal matter did not match each other with regard to elemental concentrations; moreover, while extraneuronal elemental concentrations did not vary much with age, concentrations of redox-relevant elements Fe and Cu in neuronal bodies followed inverse trends.

An excellent example of a human tissue study is a recent XFM exploration of human placental tissue conducted at the APS [61]. In addition to information about this important tissue, this work provides a comparison of different sample preparation techniques: (i) fixation in formalin; (ii) fixation in a mixture of 3% glutaraldehyde and 1% paraformaldehyde in 0.1 M phosphate buffer; (iii) and fixation in a mixture of 3% glutaraldehyde and 1% paraformaldehyde in 0.1 M HEPES buffer, with or without prior freezing at -80°C and thawing; finally, these samples were also embedded in LR resin. Two instruments were used for this work as well, a "standard" microprobe with beam spot size of 500nm and Bionanoprobe instrument with spot size of 30nm; X-ray fluorescence data were analyzed (as always at the APS) using MAPS software developed by Stefan Vogt [62]. Greatest variations in elemental abundance in this study, dependent on sample preparation approach, were noted for Ca and Cu. As recognized by this team, use of different preparation approaches is often necessitated by clinical work conditions; variations in sample "quality" with regard to particular elements should be recognized if change of sample preparation approach is not possible.

2.3 Use of XFM for examination of pathological elemental misbalance in disease

Information on elemental distribution in samples from different disease conditions has the potential to provide insights in normal and toxic variations in concentration, trafficking, distribution, and storage of different elements. For instance, it is known that during the degeneration of dopaminergic neurons in Parkinson's Disease (PD) proteins accumulate and form inclusions in substantia nigra region of the brain. Up to 24h postmortem samples of substantia nigra from PD patients were sectioned at 20 micron thickness, dried at -30°C and imaged with 15x15 micron steps at BESSY II [63]. Elemental maps of dopaminergic nerve cells and extraneuronal spaces for P, S, Cl, K, Ca, Fe, Cu, Zn, Bromine (Br) and Rubidium (Rb) were generated for Parkinson's disease sample and compared to control. PD neurons had significantly higher content of S, Cl, Ca, Fe, and Zn in substantia nigra compared to control groups. Additionally, P, S, Cl, Zn and Rb were increased in areas outside of nerve cell bodies in PD samples.

Another interesting example of work done with human samples utilized the large sample instrument at the AS where specimens of tens of centimeters can be accommodated. Chronic anemia sufferers who depend on blood transfusion often experience iron overload that often leads to cardiac toxicity. Recently, investigators at AS were able to image a 5mm tick cross section of a postmortem heart of a transfusion dependent patient [64]. XFM iron maps with 500x500 micron resolution displayed the iron distribution of the heart in great detail. A gradient in Fe distribution was found, with concentrations decreasing from the outer to the inner side of the heart muscle; however, it should be noted that this sample was stored formalin prior to sectioning and in that process, some of the Fe could have been redistributed.

A different Fe investigation study was done with the liver from patients with chronic liver diseases. The histochemistry stain Berlin blue is used most often to determine Fe in such samples, however, work by Kinoshita and others who used XFM at SPring-8 has documented that the latter approach shows superior sensitivity. Fe accumulation was noted especially in periportal area of the liver samples from patients with chronic hepatitis C (CHC) or cirrhosis. Interestingly, even in healthy livers hepatocytes in the periportal area showed higher Fe concentration, suggesting that these cells may be exposed to some degree of iron-induced free radical damage at all times [65].

Menkes disease (MD) is caused by mutations in the Cu-transporting ATPase gene (ATP7A). This protein transports Cu from the cytosol to the trans-Golgi network and enables synthesis of cuproenzymes. In addition, under elevated Cu conditions this protein translocates to plasma membrane and begins with efflux of Cu across the plasma membrane in order to maintain cellular Cu homeostasis. XFM was used to study many aspects of these processes both in patient samples and in experimental model systems. For example, cell culture studies focused on ATP7A were done with patient fibroblasts and mouse 3T3-L1 cells in which this protein was knocked out using CRISPR/Cas9 [66]. In both cases, XFM mapping (conducted at the APS) confirmed increase in Cu concentration throughout the cell volume – in cytosol, nuclei and mitochondria. Interestingly, this study found that ATP7A removal had the most profound effect on mitochondria as reflected by glutathione oxidation and increased concentration of H_2O_2. An exploratory study of Menkes disease focused primarily on patient samples was done at SPring-8 and Photon Factory in Japan. A portion of the work was done on cultured keratinocyte cells lines from two Menkes disease patients and four matched healthy individuals; this work documented

that patient cells could not maintain physiologic Cu concentrations under a mild Cu overload. Patient samples form intestine, kidney and spinal cord were also included in this work. Excess Cu was found in the mucosal epithelial cells of the intestine, in tubular cells of the kidney, endothelial cells of blood and lymph vessels as well as some parts of the spinal cord [67].

In the cytosol, Cu incorporation into secretory enzymes is mediated by Cu chaperone protein Antioxidant-1 (Atox1); in the nucleus, this protein acts as a Cu-dependent transcription factor. This protein is necessary for development of neovasculature and wound healing through regulation of vascular endothelial growth factor 1. Effects of Cu deprivation and absence of Atox1 protein in $Atox1^{-/-}$ mice on wound healing were investigated recently through a series of *in vitro*, *ex vivo* and *in vivo* experiments [68]. XFM imaging at the APS was done to corroborate Cu concentration differences and confirm that presence of Cu in the absence of Atox1 protein does not suffice for successful wound healing process.

Another interesting example of XFM use with human samples comes from an NSLS XFM study of cadaveric human eyes [69]. In the human eye, age-related macular degeneration was associated with metal-rich deposits, but the concentration and distribution of metals in deposits was not known. Interestingly, this study established that Ca and Zn were present in all deposits, Fe only occasionally, while Cu concentration in deposits could not be differentiated from the background.

Use of XFM for work with animal models of elemental misbalance is particularly popular, because animal models allow controlled genetic manipulations. For example, James and others used XFM at AS to investigate deposition of Fe, Cu and Zn in extracellular plaques forming in brains of animals with cerebral amyloidosis caused by expression of mutant human

amyloid precursor protein (APP) and presenilin 1 [70]. This work follows a study at the APS and NSLS where whole brain sections from animals of the same genotype but of different ages were scanned by XFM and Zn accumulation was found to be pronounced only in animals with fully developed plaques, with a period of more diffuse increased Fe accumulation prior to plaque formation [71]. Interestingly, while plaques could be detected by infrared spectroscopy [71, 72], they could be identified by Compton inelastic scattering as well [70].

2.4 XFM analyses of elemental content in cancer

Despite the fact that the majority of XFM studies with cells in culture are done with cancer cells, relatively few studies compared trace element status in different cancers, possibly because imaging of patient samples requires high throughput and large area scans for comprehensive, statistically significant comparisons. Nevertheless, it is probable that such work will increase in volume with the development of faster data acquisition approaches.

Work done at the APS by Chandler and others has shown that subcellular Zn accumulation in breast cancer depends on cancer subtype [73]. Zn accumulation in luminal breast tumors was found at the tissue periphery, while it was more evenly distributed in the basal breast tumors. The authors continued onward to investigate Zn transporters by microarray analysis and extend the study to breast cancer cells *in vitro*. Ultimately, Zn comparison between luminal type breast cancer cell line T47D, basal-like cell line MDA-MB-231 and non-malignant breast cell line MCF10A has shown different staining patterns and Zn accumulation according to FluoZin-3 dynamic labeling. It should be noted that Zn concentration in non-malignant cell line was the lowest. This was in keeping with previous work done at the APS where benign breast cancer screening by XFM was done with 252 matched pairs of benign breast cancer samples [74]; in that work increased Zn concentrations were associated with an increased cancer risk. It is interesting to note that a study of esophageal samples, also conducted at the APS associated increased Zn concentrations with decreased risk of subsequent cancer development [75].

Recently, XFM was used to examine and compare trace metals concentration at the micro- and nanometer scale in patient derived human glioblastoma cells (11ST, 36ST, 86ST) and commercially available cell culture cell line (U87MG). The work was done at the APS using

flash-frozen cells at the high resolution cryogenic instrument Bionanoprobe and at the microprobe at sector 2ID-D equipped with a cryo-jet. Quantities of P and Zn were found to be increased in the cell nuclei while Fe, Mn and Cu accumulated in cytoplasm and perinuclear region. Fe and Mn accumulated in different regions of U87MG cells. In the patient-derived cell lines 11ST, 36ST and 86ST Fe accumulated mostly in perinuclear space with Zn and K. Interestingly, the patient derived 86ST cell line presented the highest content for most metals in comparison to other cell lines. In these cells Cl, Fe, Ni, Cu and Zn were increased at least twice compared to other samples [76].

Cancer related animal model studies have used XFM as well. For example, in order to identify the relationship between selenium intake and breast cancer progression Seleno-L-Methionine supplement was tested in mice with developed 4T1 murine mammary carcinoma. Oral treatment was done for 28 days and the effect of SeMet on tumor growth was assessed. XFM was done at the SSRF and Se accumulation detected in tumor tissues, surprisingly, overlapping with the highest Fe distribution (and possibly tumor vasculature). Immunohistochemistry for Se binding proteins: glutathione peroxidase 1 and Selenium-binding protein 1 showed inverse pattern in treated and untreated tumors, the latter protein more increased in animals exposed to Seleno-L-Methionine supplement. Tumor growth in these mice was decreased [77].

2.5 XFM investigation of (experimental) elemental overload

Successful use of XFM to investigate elemental homeostasis served as a basis to inspire studies of elemental "overload" either to investigate processes involved in elemental storage or to attempt to exploit accumulated elements in order to achieve better diagnostic imaging using only "native" elemental content of cells.

For example, the idea to use Mn to increase native tissue contrast for magnetic resonance imaging (MRI) was entertained by researchers interested in functional imaging of pancreatic β-cells during activation. In an *in vitro* study conducted at the APS, XFM was used to visualize and quantify Mn in pancreatic β-cells and their subcellular regions. As a model system MIN-6 insulinoma cells were used. When these cells were grown in standard tissue culture conditions with only a trace amount of Mn, this element was present in low 22 μM concentration and equally distributed across the cell. Exposure of cells to higher Mn concentration (50μM $MnCl_2$) in medium with 2mM glucose did not activate cells but resulted in non-glucose-dependent Mn uptake (250 μM cellular Mn concentration). However, when cells were activated by 16mM glucose in the presence of exogenous $MnCl_2$ cellular Mn concentration increased to 590 μM. Interestingly, Mn distribution in these cells was uneven – with Mn both in the cytoplasm and accumulated in a perinuclear region, possibly corresponding to the Golgi apparatus and involving the secretory pathway [78].

A different group of researchers focused on iron accumulation in cells exposed to inorganic iron (Fe(III) citrate, Fe(III) chloride and Fe(II) sulfate) and iron associated with its natural carrier protein - transferrin [79]. Two cell lines (colorectal cancer cell lines HT-29 and HCA-7) with different expression of transferrin receptors were studied using several X-ray

techniques – XFM at the Diamond Light Source and X-ray absorption near edge structure (XANES) spectroscopy at HASYLAB beamline at DESY synchrotron. While XFM mapping demonstrated Fe accumulation in cytoplasmic regions, XANES could be used to complement this study and determine relative ratios of Fe(III) sulfate vs. ferritin in HT-29 cells treated with different sources of iron. Comparisons with known XANES profiles for pure chemical/biological compounds was done using ATHENA software package analysis [80].

2.6 XFM exploration of exogenously added elements in cells and tissues

XFM is often used to inform researchers about the intracellular distribution of exogenous molecules and (nano)particles deliberately introduced into cells, e.g. for diagnostic or therapeutic purposes, or in order to study the first steps underlying different types of toxic exposures. This approach is especially simple when (some of) the elements that make these exogenous treatments are not native to cells, although this is not necessary for successful imaging. Often, such chemicals and/or nanomaterials combine several elements – in such cases elemental co-registration which is inherent to XFM imaging data, can be used to increase confidence in the data, or, conversely, to document material degradation caused by interaction with biological system under study.

Many agents used to increase contrast in magnetic resonance imaging contain elements that are not native to cells. This is convenient for XFM studies and it was used by Karczmar laboratory in order to establish pattern of contrast agent accumulation in different disease conditions. Frequently, dynamic contrast material–enhanced (DCE) MRI is used to detect invasive breast cancer since the sensitivity and specificity of DCE-MR for the early detection of invasive disease is equal or superior to X-ray mammography. Animal studies coupled with XFM at the APS established that gadolinium accumulates in ductal carcinoma *in situ* (DCIS). Therefore, it is probable that during DCE-MR imaging gadolinium penetrates the basement membrane to enter mammary ducts distended with DCIS. Elemental gadolinium concentrations measured in animal experiments showed average concentration of 0.475 mmol/L [81]. Similarly, newly developed Gd contrast agent gadodiamide was evaluated in an animal model of prostate cancer. XFM imaging of mouse prostates harvested 10 minutes after IV injection of

gadodiamide (0.13 mmol/kg) was done at the APS. The mean concentrations of gadolinium in the epithelia and lumens of prostatic glands from six animals were 1.00 and 0.36 mM, respectively, suggesting that uptake of contrast agent occurs in both prostate compartments [82]. Finally, the same group of researchers investigated new vanadium contrast agents for MRI [83]. This investigation involved mouse colon cancer model. Animals given contrast agents based on vanadium-based chelates were imaged by MRI, and sacrificed 2h later. Colon tissue samples from animals developing cancer contained many vanadium hot spots.

It is important to note that gadolinium has been reported as a cause of nephrogenic systemic fibrosis – a disease with decreased kidney function and a fibrosing disorder of the skin and systemic tissues. Tissue samples from patients with nephrogenic systemic fibrosis have micron-sized insoluble deposits containing gadolinium. To clarify the precise chemical structure of these deposits, skin samples from a patient were examined using synchrotron XFM. The deposits contained Gd, Ca and P, suggesting that chemical release of gadolinium from a contrast agent molecule occurs in human tissue. This supports the idea that there is a link between development of this disease and dose and stability of the contrast agent [84].

Stability of a chemical compounds is often critical for obtaining desired effects. For example, a new group of chemotherapy drugs based on ruthenium-iodine complexes was explored in cell culture experiments and the samples were investigated by XFM at the APS [85]. Persistent co-localization of the two elements suggested that the new compounds are stable in medium, during cellular uptake and processing.

Other chemical agents, including some that are present in everyday products may have adverse health effects. For example, standards for chromium content in water apply to the total

of Cr(VI) and Cr(III); however, while Cr(III) was found to be harmless in rodent models, Cr(VI) was associated with increased incidence of duodenal cancer. XFM imaging at NSLS was done, finding 30 times more Cr in duodenal villi than crypt regions of intestinal samples from exposed mice. A parallel investigation of DNA damage in these samples documented elevated numbers of gamma H2AX foci (loci of DNA double strand breaks) in the same tissue region [86].

Studies of interactions between cells and exogenous compounds and nanomaterials are often conducted *in vitro* or *ex vivo*. The latter approach was used to study interaction between peripheral blood cells and technetium-tin (^{99m}TcSn) colloid in order to provide deeper insight into a procedure routinely used in clinic to label phagocytic leukocytes and image sites of infection. XFM mapping of neutrophils allowed examination of changes in element distribution that accompany neutrophil phagocytosis of TcSn colloid, presumably via a Complement Receptor 3 mediated process. Uptake occurred in half the neutrophils from a healthy individual. Within cells, Sn co-localized with iron (Fe) and sulfur (S), and it was negatively associated with calcium (Ca). The subcellular colocalization of Sn with Fe was consistent with fusion of the colloid-containing phagosome with neutrophil granules. The negative colocalization with Ca indicates that ongoing maturation of the TcSn colloid phagosome is no longer calcium dependent one hour after phagocytosis. It should be pointed out that co-localization between tin and technetium and ^{99m}Tc decay products could not be found despite the high sensitivity of XFM [87]. This study is nevertheless particularly interesting for future XFM research because it details a pixel by pixel analysis and mapping approach that incorporates cluster analysis in order to differentiate Sn pixels in neutrophils from those in artefactual contaminants.

Another study working with radioactive elements was the work of Jensen and others that quantified and imaged plutonium (^{242}Pu) in rat pheochromocytoma cells (PC12) [88-91]. Importantly, this work used micro XANES at the 2ID-D beamline at the APS to evaluate chemical state of Pu inside cells, and small angle X-ray scattering (SAXS) beamlines of the APS to determine that Pu can be incorporated into transferrin protein without disturbing its tertiary structure. Pu was taken up by cells most efficiently when it was associated with transferrin and taken up by cells via transferrin receptor endocytosis.

Platinum-based chemotherapy agents such as cisplatin have long history as anticancer drugs. Most of the FDA approved Pt based compounds carry the most reactive chemical state of Pt: Pt(II), and while they are effective against cancer cells, toxicity of such drugs for normal tissues (such as, for example sensory neurons) is significant [92-94]. Different strategies are developed to lessen this problem, from Pt compounds that are less reactive prior to uptake by cancer cells, to development of delivery vehicles such as liposomes: spherical lipid bilayers. For example, high resolution XFM at the beamline ID22 at ESRF was used to investigate the changes in elemental composition, distribution, and concentration of Pt inside F98 glioma cells following treatment with cisplatin associated liposomes. While Pt and Zn content decreased in live cells, higher levels of calcium and lower levels of potassium are found in dead cells; this knowledge was used to interpret the data additionally. These results suggested that the liposomes could provide an effective method for platinum administration [95]. Likewise, when XAFS experiments were done at SPring8 it was found that chemical speciation changes of Pt (IV) into Pt(II) depended on uptake of newly developed Pt(IV) compounds by cancer cells [96].

Many other chemotherapeutic drugs are compounds made of elements that match cellular elemental content (C, H, O); doxorubicin (also known as Adriamycin) is such an example. While this chemotherapy drug does not "stand out" in XFM imaging, this molecule is optically fluorescent. The possibility to use optical fluorescence imaging and couple it with XFM imaging was used by researchers from Woloschak laboratory [12, 33, 87] both to investigate stability of nanoparticle-doxorubicin complexes and for different purposes. Most recently, exploration of more efficient ways to label TiO_2 nanoparticles for optical imaging was corroborated by high resolution XFM imaging at the Bionanoprobe instrument at the APS [33]. In previous work, combined optical imaging and XFM were used to study targeted distribution of nanoparticles [8], as well as to register separation between Fe_3O_4@TiO_2 nanoparticles and doxorubicin when doxorubicin-coated nanoparticles were taken up by ovarian cancer cells [12]. XFM was used very effectively by the same group for evaluation of nanoparticle uptake in single cells as a primary mode for nanoparticle detection. This work included the very first foray in subcellular targeting of TiO_2–nucleic acids nanoparticles [3] and the subsequent refinements of subcellular nanoparticle targeting dependent on cellular uptake by electroporation [17]; exploration of TiO_2 nanoparticles as a platform for delivery of MRI contrast agent gadolinium [7, 16]; and the most recent work on targeting genomic DNA for damage by mimicking native cell ligands with nanoparticles and employing cell surface receptors that translocate the nanoparticles to cell nuclei [20]. In this study, about 20% of Fe_3O_4@TiO_2 nanoparticles inside cells were found inside cell nuclei. This work was the very first example of hard X-ray fluorescence tomography accomplished by cryogenic imagining of frozen hydrated flash frozen nanoparticle treated cells.

It showcased the new XFM nanoprobe – the Bionanoprobe, a unique instrument located at the APS [40, 41].

As nanoparticle research advances, there is particular interest in targeting nanoparticles and nanoconstructs for the treatment of cancer. Understanding the transport of targeted nanomaterials in tumor tissues *in vivo* is important for optimizing their therapeutic properties and developing the next generation of nanomedicines. In addition to cells, Fe_3O_4@TiO_2 nanoparticles were also given to rabbits that were implanted with VX2 cells in order to develop liver cancer. Two different modes of nanoparticle delivery were tested, "regular" intravenous delivery and trans catheter delivery directly to liver arteries supplying the VX2 tumor. The latter was shown to be more efficient even though nanoparticles were targeted for delivery to neovasculature [97]. Low resolution XFM imaging at sector 8 of the APS was used to screen for nanoparticle accumulation in tumor parenchyma as well as liver, kidney, spleen and lung and evaluate of-target delivery of the same nanoparticle formulation under two different delivery modes.

Many other groups have used XFM as well, as the means to gain quantitative insights into the tumor targeting and tissue penetration ability of nanoconstructs. A recent study conducted at the Australian Synchrotron used XFM to map and quantify distribution of transferrin-conjugated gold nanoparticles in human breast cancer cell line MCF-7 grown as spheroids. Despite their high targeting efficiency, these nanoparticles had limited penetration (less than 50 microns) when they were mixed with spheroids, even after 48 hours long incubation [98].

2.7 XFM exploration beyond mammals: elemental concentration, distribution and speciation in bacteria, eukaryotic single cell organisms and plants

In addition to work with mammalian cells and samples discussed so far, XFM is also often used to quantify elements in bacteria and other single cell organisms, all of them of greatest importance for maintenance of the biosphere. For instance, marine cyanobacterium *Trichodesmium erythraeum* is made of groups of single cells – trichomes, and has a special adaptation that allows it to sequester CO_2 by photosynthesis and do nitrogen fixation at the same time. If both processes were in the same cell, oxygen produced by photosynthesis would interact with iron from the enzyme nitrogenase and interfere with the nitrogen-fixing process, therefore, two functions are segregated into separate compartments – trichomes. The spatial distribution of Fe, S, and P in trichomes was mapped by XFM during exponential and growth phases of this organism. About 16% of trichomes sections (up to 25 cells) have 2-fold more Fe and S and 2-fold less P compared to neighboring trichome sections. This ability to re-allocate elements indicates that *Trichodesmium* is a community of cells with specialized regions of multiple cells with unique chemical composition and specialized "tasks" [99].

Sulfate-reducing bacteria can produce sulfide that reacts with metals to form insoluble products such as ZnS. Spherical aggregates of ZnS (sphalerite) 2-5 nm diameter in size are formed within natural biofilms dominated by sulfate-reducing bacteria of the family Desulfobacteriaceae. Zinc concentration in these biofilms can be as much as 100-fold higher than Zn concentration of groundwater in which the biofilm is growing. XFM analysis done at the APS showed that ZnS aggregates in addition to these core atoms, also contain arsenic (As), Se, and Fe

but exclude lead despite of its presence in the groundwater. This finding suggests that microbes and microbial biofilms control metal concentrations in groundwater [100].

Traditionally, the metal composition of bacterial cells has been measured by bulk elemental analysis and averaged, with little interest in possible alterations of elemental composition in response to substrate sufficiency vs. starvation vs. toxic stress. XFM at the APS was employed to determine changes in the elemental composition of bacterium *Nitrosomonas europaea* 19718 caused by growth and/or exposure to Cu(II). Exposure to Cu(II) caused statistically significant increase in cellular Cu concentration, while different growth status had little effect on Cu and Fe concentration. Ratio of Fe and Cu to other elements in this organism was higher than in *Pseudomonas fluorescens.* This suggests that that the former bacterium may have higher demand for Fe and Cu because of enzymes involved in nitrogen fixation need metal cofactors for electron transport [101].

Phytoplankton in the coastal seas of West Antarctica leads to substantial loss of iron from marine ecosystems because it incorporates it into biogenic silica (Si). XFM was used to analyze Fe and Si quantity and distribution in these organisms and confirm this hypothesis. In each specimen Fe and Si were co-localized, confirming structural incorporation of iron into cell walls made of silica [102].

Arbuscular mycorrhiza is a symbiosis between plants and fungi. Cooperation between the species improves the supply of water and macro-elements such as phosphate and nitrogen to the host plant, while as much as 20% of plant-fixed biomass supplies the fungus as a source of energy. XFM at SPring-8 was used to find that exposure to cadmium (Cd) leads to accumulation of this toxic element in cells and cell walls of both symbiotic organisms [103]. Further research

may be able to establish how to reduce or increase Cd accumulation when plant production is done for the purposes of food production or heavy metal decontamination, respectively.

Fe is an essential element for plant growth and development; however, its potential interaction with oxygen produced by photosynthesis requires compartmentalization and tightly regulated Fe acquisition and allocation. To evaluate Fe in tomato plant roots and cucumber leaves, XFM was done at DESY. Inside root, Fe was found in the outer layer - the rhizodermis. The Fe concentration there was two to three orders of magnitude more than in the inner portion of this organ where it averaged 10 μg/g. In cucumber leaf Fe concentration was highest in the midrib, with 600 μg/g, up to 60 fold higher than in the cells of parenchyma [104].

Similar to compartmentalization of iron, Ca^{++} distribution in *Arabidopsis thaliana* is tightly regulated. Proteins called cation exchangers (CAXs) are involved in this process. XFM imaging of wild type and mutant *Arabidopsis* seeds was done at the NSLS. Elemental maps showed that altered Ca localization within cells and reduced partitioning into organelles in mutated seeds. Interestingly, changes in Ca distributions were different in CAX1 and CAX3 single and double mutants, suggesting that these two genes play distinct roles in different seed compartments. In addition, K, Mn and Fe were also redistributed in mutant seeds [105].

XFM at the SSRF was done to investigate accumulation of Pb in plant *Elsholtzia splendens*—a copper accumulator plant exposed to Pb. This toxic element was mostly accumulated in the roots but also stems and leaves. In latter organs, Pb was restricted to the vascular bundles and epidermis. A significant positive correlation between Pb, Ca, K, and Zn distribution was found and correlation between Pb and Ca was the greatest. This insight could be exploited either to decrease or increase accumulation of Pb in this species [106].

Production of biofuels and chemicals from plants requires chemical pretreatments that could be made simpler if iron was present in plant material. To enrich plant matter with iron, transgenic *Arabidopsis* plants expressing heterologous ferritin gene were engineered. These plats accumulate iron under both control and iron-fertilized growth conditions. Growth in the presence of Fe fertilizer led to an increase in plant height and dry weight by more than 10%. Fe accumulation in these plants occurred in cell walls as determined by XFM studies conducted at the APS [107].

2.8 Conclusions

XFM is a powerful and versatile technique for investigation of elemental content in biological samples. The most accurate results are obtained without chemical fixation with flash frozen samples imaged under cryogenic conditions. XFM qualified by these conditions is unequivocally better than any other approach with respect to accuracy and sensitivity of elemental mapping and concentration evaluation. Whole cells can be imaged with resolutions better than 100nm and their content 3D reconstructed despite cell thickness of 10 microns or more; with some compromises in the spatial resolution samples as thick as 100s of microns can also be imaged in 3D. Other compromises in XFM are also often unavoidable due to exigencies of biomedical research. Various sample manipulations are sometimes necessary, from freeze drying, to chemical fixation to air drying. Despite the fact that such preparation approaches alter some of the elemental concentrations – it rarely happens that it is not possible to decide which elements are most relevant for a study in question and find a proper preparation approach. With new technical developments such as "fourth generation" synchrotrons, faster detectors and even "X-ray focusing" optics it is likely that XFM will continue to develop toward ever higher resolution and speed of data acquisition.

CHAPTER 3: Labeling and *In Situ* Detection of TiO_2 Nanoparticles

(adapted from Brown, K., Thurn, T., Xin, L., Liu, W., Bazak, R., Chen, S., Lai, B., Vogt, S., Jacobsen, C., Paunesku, T., and Woloschak, G. (2017). Intracellular *in situ* Labeling of TiO_2 Nanoparticles for Fluorescence Microscopy Detection. Nano Research. (*In press*)

3.1 Introduction

Despite the extensive body of research exploring the interactions between TiO_2 nanoparticles and neoplastic cells, the chemical techniques to fluorescently label TiO_2 nanoparticles *in vitro*, *in vivo*, and *ex vivo* are limited and primarily depend on use of Alizarin Red S (ARS) [8, 10, 13, 15, 19]. Although this molecule binds well to the nanoparticle surface as an enediol ligand, its fluorescent yield is small and in the range of 0.001 units at best [108], while, for example, fluorescence quantum yield for Alexa Fluor 488 is 0.92 units (according to Invitrogen). In addition to ARS, chemotherapy drug doxorubicin also fluorescently labels TiO_2 nanoparticles however, its binding to the surface of TiO_2 nanoparticles is mediated by single OH groups, and labeled nanoparticles shed doxorubicin molecules after cellular internalization [12]. Additionally, illumination of nanoparticles by light of UV-range wavelengths used for fluorescent microscopy excites TiO_2, causing ROS release, which results in rapid bleaching of the samples. To make things more complicated, TiO_2 nanoparticles quench fluorescence from immediately adjacent fluorophores such as Cy3 and FAM when they are used to label single-stranded DNA oligonucleotides, and these in turn are adsorbed onto 20nm nanoparticles by phosphate groups [109]. Several studies attached biotin to TiO_2 nanoparticles [1, 9]; however, this route for indirect labeling of nanoparticles in cells is challenging because of possible artifacts associated with background streptavidin labeling of cells. This has hindered our ability to gain in-depth knowledge of the details and mechanisms of TiO_2 nanoparticle cellular targeting, internalization, and subcellular localization. Techniques that do not rely on fluorescent labeling such as transmission electron microscopy (TEM) and X-ray fluorescence microscopy (XFM or SXRF) are often used to determine TiO_2 internalization and intracellular stability [3, 7,

8, 10-12, 15, 110]. XFM is a quantitative technique used to detect and map nanoparticles directly in whole cells based on titanium-specific K-alpha X-ray fluorescence emitted from titanium (Ti) atoms. XFM scanning registers a quantitative and qualitative map of the distribution of cellular elements such as sulfur (S), phosphorus (P), and zinc (Z) [110]. Similarly, energy dispersive electron spectroscopy (EDS, EDX, or XEDS) can be used to identify the elemental signature of titanium, but this technique does not function in combination with whole cells. However, both EM and XFM suffer from low throughput and other limitations. TEM requires biological sample sectioning and permits analysis of only a small number of cells. Similarly, XFM is not readily available and requires synchrotron-quality X-rays. Both techniques can be expensive and technically challenging, and neither allows analysis of large numbers of cells.

In order to meet the demands of the growing body of research exploiting TiO_2 nanomaterials, it has become necessary to develop an *in situ* post-treatment labeling approach capable of precisely detecting the subcellular localization of nanomaterials in cells as well as tissue samples; such a technique also must be quick and produce consistent results. Herein, we describe two *in situ* labeling techniques to label TiO_2 nanoparticles in order to image them using fluorescence microscopy. In addition, XFM was used to confirm the co-registration of the Ti elemental signature and nanoparticle optical fluorescence.

3.2 Fluorescein-biotin Labeling and Detection

We attached FITC-biotin to the TiO_2 nanoparticle surface through hydroxyl groups on the FITC part of the molecule (indicated by dashed lines in Fig. 1(a)). Due to the distance between these two OH groups, it is unlikely that both of these attach to the nanoparticle at the same time. Nevertheless, a single OH group binding to the nanoparticle surface is sufficient for nanoparticle coating; we have found this to be true in the past, e.g., for binding of doxorubicin [12]. Labeled nanoparticles (Figure 3.1(a)) were incubated with MCF-7 breast cancer cells and imaged first using confocal microscopy (Figure 3.1(b)) and then XFM (Figure 3.1(c)) to detect the intracellular localization of the nanoparticles in a single cell. Because TiO_2 nanoparticles are surface reactive and may bind to additional parts of FITC-biotin instead of to hydroxyl groups only, we were concerned about quenching of some of the fluorescent signal (similar to quenching of Cy3 and FAM[9]). To prevent this, binding between nanoparticle and FITC-biotin was performed in the presence of glucose to additionally coat the surface of TiO_2.

After a 16 h treatment with nanoparticles, the cells were sorted by flow cytometry, seeded on formvar-coated gold TEM grids, and allowed to attach for 3 h prior to fixation and confocal fluorescence imaging. After optical fluorescence imaging, during which the grids were submerged in mounting media, the grids were rinsed in PBS, dehydrated in ethanol, and air dried prior to XFM.

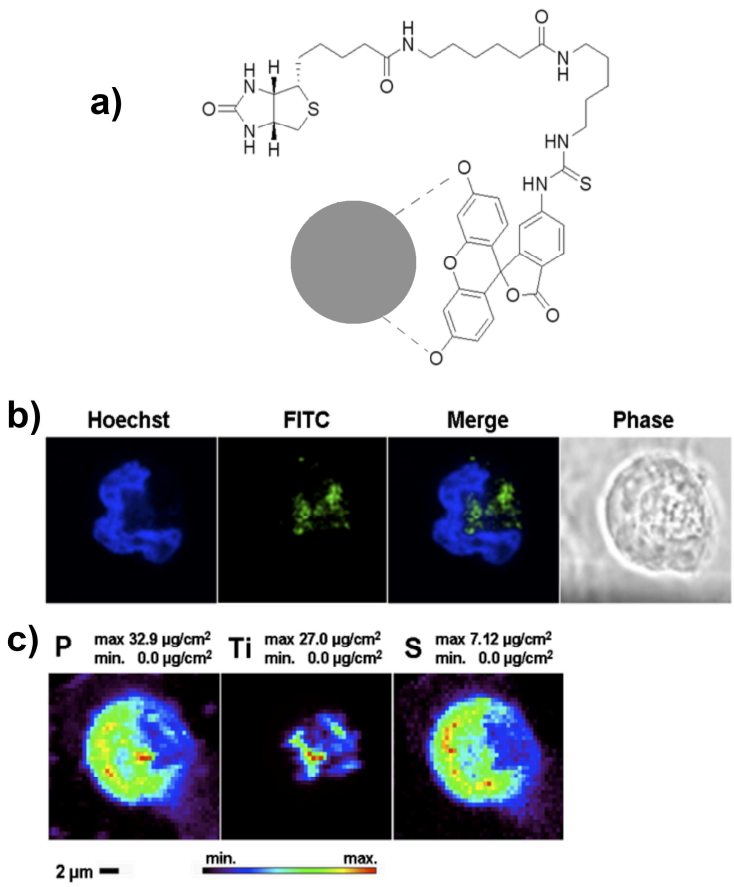

Figure 3.1. Fluorescent labeling and uptake of TiO2 nanoparticles. (a) Possible interactions between nanoparticle and fluorescein biotin. There are two free OH groups on fluorescein molecule that are able to bind the TiO_2 surface, similar to doxorubicin molecules [12]; they are indicated by dashed lines between oxygen atoms and nanoparticle (gray circle). (b) Confocal imaging of MCF-7 cell treated with TiO_2 nanoparticles coated with fluorescein (FITC)-biotin. Separate and overlapping images of Hoechst (nuclear DNA) and FITC (nanoparticles) are shown as well as matching phase contrast image. (c) X-ray fluorescence microscopy (XFM) maps show the distribution and concentration of phosphorus (P), titanium (Ti), and sulfur (S) in the same MCF-7 cell treated with the FITC-biotin coated TiO_2 nanoparticles. The positions of FITC signal in confocal image and Ti signal in the XFM map are well matched.

XFM was performed using the X-ray microprobe instrument with 2ID-E beamline at the APS, ANL. The X-ray fluorescence map of sulfur showed the boundaries of the cell as expected [3, 7, 8, 10, 16-18, 20, 40, 111] and corresponded well with the cells' outlines in optical fluorescence microscopy. Similarly, the strongest phosphorus signal area in the phosphorus XFM map overlapped with the cell nucleus; again, this matched well with the DNA (Hoechst) fluorescent signal obtained by confocal microscopy. A strong titanium signal (per-pixel signal of up to 27 μg cm^{-2}) was detected by XFM inside the cells but outside of the nuclei. The distribution of titanium and, therefore, TiO_2 nanoparticles showed a good overlap with the FITC fluorescence signal in images obtained by confocal fluorescence microscopy. The slight discrepancies between the images are expected since the cells were hydrated for confocal light microscopy but dried for XFM measurements. Moreover, imaging by XFM is performed with the sample mounted vertically into a special sample holder and positioned at 45° to the incident beam direction and detector, making direct comparisons between images impossible. It should also be noted that the substrates suitable for imaging by XFM are not ideally suitable for confocal fluorescence microscopy. In many cases, when formvar-coated TEM grids are used for cell growth, cells detach from the substrate during manipulations that remove mounting media necessary for fluorescence microscopy, and often only clusters of cells remain attached to the substrate, as happened with the cells shown in Figure 3.1.

3.3 Streptavidin Secondary *In Situ* Detection of Fluorescein-Biotin Labeling

In order to show the selectivity and specificity of labeling TiO_2 nanoparticles with FITC-biotin and mitigate the potential problem of signal quenching when nanoparticles are directly labeled with FITC-biotin, we decided to expose nanoparticle aggregates inside cells to secondary *in situ* labeling and use the interaction between fluorescent streptavidin and biotin attached to the nanoparticle to confirm that the two fluorescent signals overlap. Cells that contained nanoparticles modified with FITC-biotin were purified by flow cytometry sorting, seeded on formvar-coated TEM grids, fixed, permeabilized, and stained with streptavidin-Cy3. Confocal imaging of biotin-FITC, streptavidin-Cy3, and Hoechst was performed (Figure 3.2(a)), and the TEM grids with cells were rinsed in PBS, dehydrated in ethanol, and air died to be imaged by XFM. Several single cells and cell clusters were imaged by confocal microscopy, but only the cluster shown in Figure 3.2 remained attached to the formvar substrate at the time of XFM imaging. The localizations of the optical fluorescence signals were compared to the 2D XFM map of titanium in the same whole cells (Figure 3.2). Several cells depicted in Figure 3.2 demonstrate an overlap between the position of titanium (maximal per-pixel concentration of titanium up to 44 μg cm^{-2}) determined by XFM and sites of FITC and Cy3 dual fluorescence detected by confocal optical microscopy.

Although this approach for optical labeling of nanoparticles is currently shown to be feasible, the presence of biotin may significantly affect interactions between the cells and the nanoparticles. For example, biotin uptake occurs both in cancer cells [112] and cells of normal tissues [113]. Biotin enters cells via the ubiquitously present protein-solute carrier family 5 member 6 (SLC5M6), also known as the sodium-dependent multivitamin transporter. It is

probable that the nanoparticles coated with biotin would engage in biotin receptor-mediated uptake by many different cell types *in vivo*. This would interfere with the intended cellular targets of nanoparticles by creating a "targeting competition" between biotin receptors and the intended cell surface epitopes.

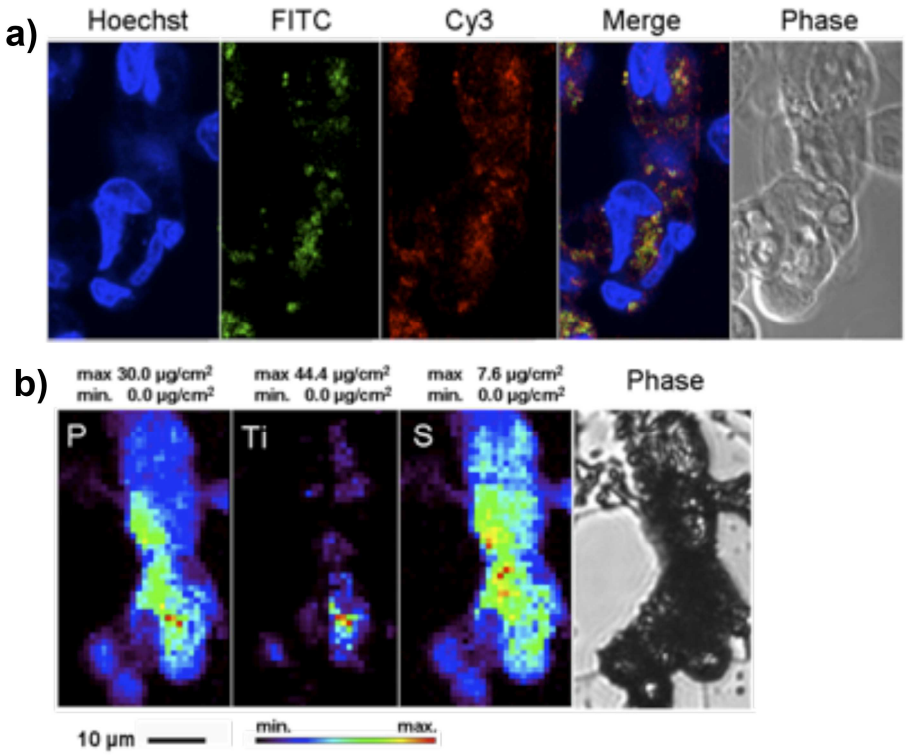

Figure 3.2. Secondary *in situ* fluorescent labeling of TiO2 nanoparticle aggregates. A cluster of MCF-7 cells treated with FITC-biotin TiO_2 nanoparticles was chemically fixed, permeabilized and subsequently treated with Cy3 labeled streptavidin. (a) Confocal microscopy shows matching positions of florescent signal of FITC-biotin coated nanoparticles (green) and fluorescent signal of Cy3 streptavidin (red) interacting with biotin on nanoparticles after post-fixation labeling of nanoparticle treated cells. Nuclear DNA was labeled by Hoechst. (b) XFM maps show cytoplasmic distribution of titanium (Ti) as well as 2D distribution of native cell elements P and S (last image in top row shows a phase contrast image of the sample prior to XFM). In this instance combined FITC and Cy-3 (a) signals and Ti fluorescent signal (b) show similar pattern of distribution.

3.4 Streptavidin-Alexa 488 *In Situ* Detection of Dopamine-Biotin Labeling

In order to create a labeling and detection system that was more stable than labeling TiO_2 nanoparticles with FITC-biotin and secondary detection with Streptavidin-Cy3, we decided to label nanoparticles with dopamine-biotin (see Figure 1.2). Dopamine binds to TIO_2 through two hydroxyl groups rather than single hydroxyl binding through FITC; in these experiments biotin was conjugated to dopamine using the free amino group of dopamine (Figure 3.3).

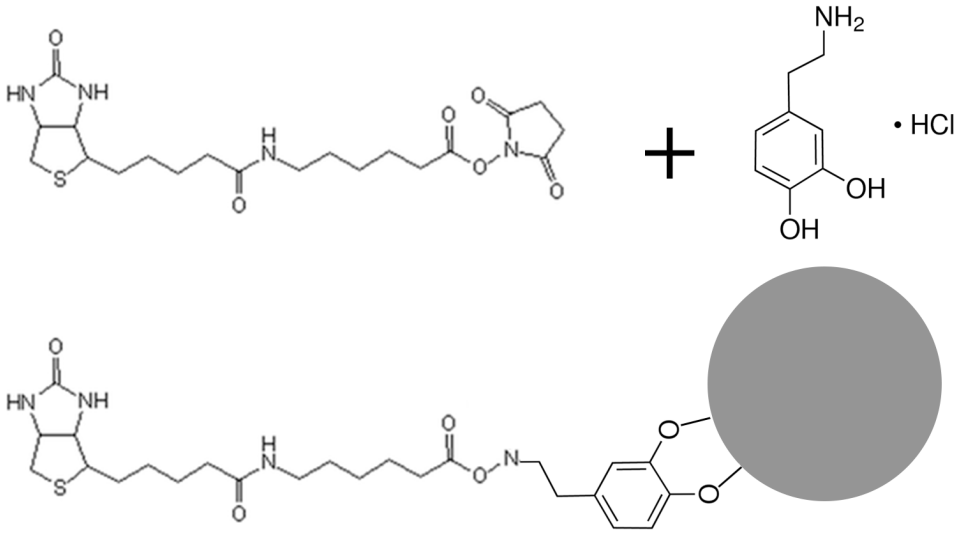

Figure 3.3. Secondary *in situ* fluorescent labeling of TiO2 nanoparticle aggregates. Biotin-NHS compound was conjugated with amino group of dopamine using a standard chemistry procedure. Resultant molecule – biotin dopamine was attaches to nanoparticle surface via hydroxyl groups of dopamine.

Dopamine-biotin labeled nanoparticles were introduced into HeLa cells seeded on barrier slides, cells were fixed, permeabilized and stained with streptavidin-Alexa 488. We expected that the interaction between biotin on the nanoparticle surface and streptavidin would be more exclusive than in the case to biotin-FITC labeled nanoparticles. In this experiment, biotin was attached covalently to dopamine and the dopamine was attached covalently to the nanoparticle; we therefore used the harshest washing procedures for further processing of these samples that would still permit binding between biotin and streptavidin. At the conclusion of these washing procedures, cellular nuclei were labeled with Hoechst 33324. Confocal imaging of Alexa 488 (streptavidin, on or off nanoparticles) and Hoechst (cell nuclei) was done (Figure 3.4). The fluorescence pattern in cells without nanoparticles was similar to cells with nanoparticles suggesting that a streptavidin-Alexa 488 detection system was not specific enough to image TiO_2 nanoparticles intracellularly. It is possible that the biotin on the nanoparticle surface was not able to interact with streptavidin e.g. because of the relatively short distance between biotin and the particle surface or because of the rigidity of chemical bonds in this type of nanoconstruct. Alternatively, it may be that the endogenous biotin was as abundant as biotin on the nanoparticle surface and no specific difference between nanoparticle aggregates and cytosol could be detected. In order to address the second type of labeling complications, we continued to modify the experimental conditions in order to reduce the fluorescent intensity in cells without nanoparticles. For example, we changed cell permabilization detergents and wash buffers. We also varied washing times, permabilization times, used different cell types, changed the detection fluorophore, reduced the concentration of streptavidin-Alexa 488 and pre-blocked cells with streptavidin and neutravidin. Despite these changes in experimental conditions the outcome of

the experiment did not change significantly (data not shown). Our ultimate conclusion was that the former explanation of the situation is more likely – geometry of biotin – dopamine molecule attached to nanoparticle surface did not allow the subsequent interaction between biotin and streptavidin. While we could have continued to test different linkers to distance dopamine from nanoparticle and ease access for streptavidin, we decided to turn instead to the use of smaller chemical molecules and use CLICK chemistry to label nanoparticles *in situ* rather than continue to develop streptavidin-dependent staining procedures.

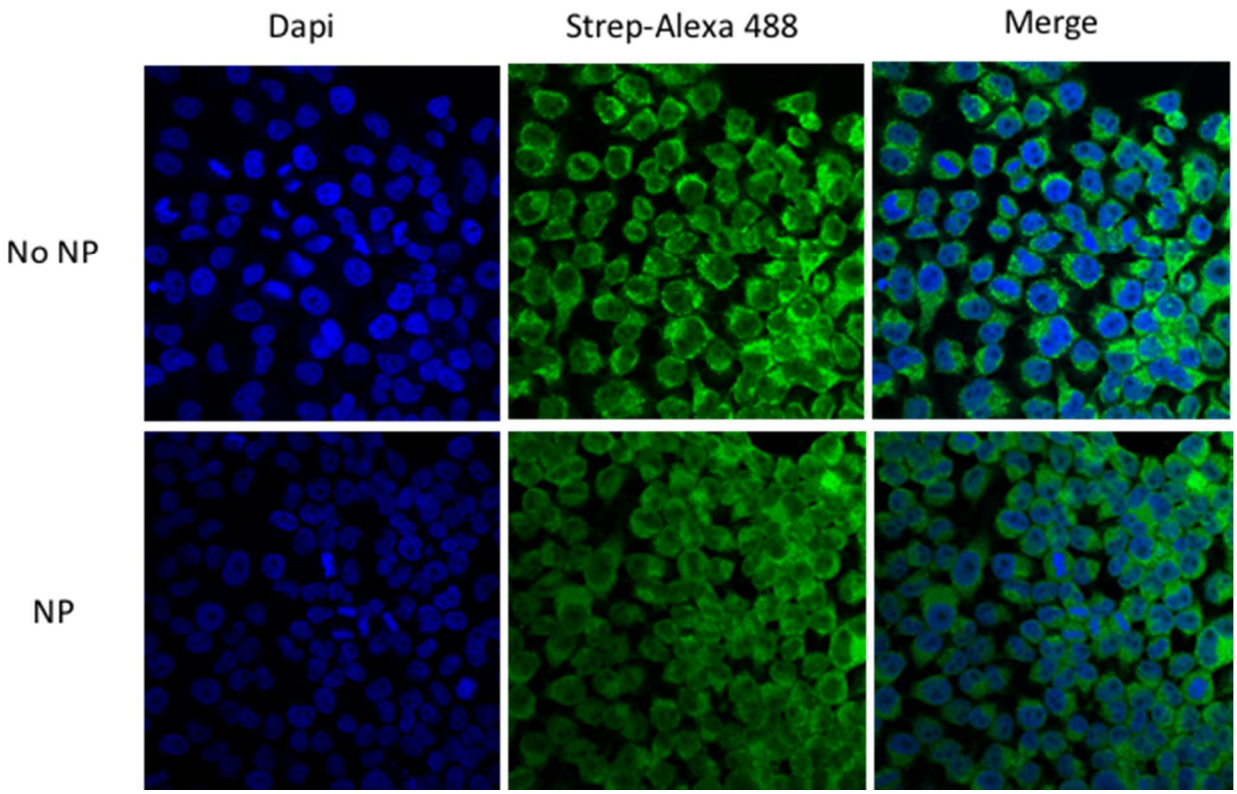

Figure 3.4. Streptavidin-Alexa 488 staining of control cells (No NP) and cells treated with dopamine-biotin coated TiO_2 nanoparticles (NP). No significant difference in labeling of these two samples was noted. Streptavidin distribution in both samples has shown the same non-specific pattern.

3.5 Nanoparticle labeling with dopamine-azide and detection by CLICK Chemistry

Since we were unable to develop a robust procedure for biotin-streptavidin labeling of TiO_2 in cells, we decided to investigate alternative approaches for nanoparticle labeling *in situ*. Seeking nanoparticle coatings that would not target any specific cell receptors, we decided to investigate azide-PEG_4-dopamine (Figure 3.5) as a surface modification of TiO_2 nanoparticles and use it as a basis for subsequent *in situ* CLICK reaction with commercially available Alexa Fluor 488 alkyne [56]. Azide moieties in cells are sparse, making CLICK labeling suitable for cell biology. In its interaction with TiO_2 nanoparticles smaller than 20 nm, dopamine is known to form stable covalent bonds spontaneously; the present study and previous studies used dopamine and dopamine-linked molecules for stable surface modification of TiO_2 and TiO_2 shell nanoparticles [1, 3, 4, 8, 11, 13, 14, 17, 18, 20]. Nanoparticles conjugated to dopamine-azide showed some increase in hydrodynamic diameter compared with that of bare nanoparticles alone when assessed using dynamic light scattering (Table 3.1). In addition, we noted small differences between zeta potentials of azide-coated nanoparticles; they shifted from -34.07 ± .91 to -31.30 ± .78 mV in comparison with those of uncoated nanoparticles (Table 3.1). Finally, size and aggregation of azide-coated nanoparticles were slightly increased compared with that of bare nanoparticles by cryo-TEM (Figure 3.6).

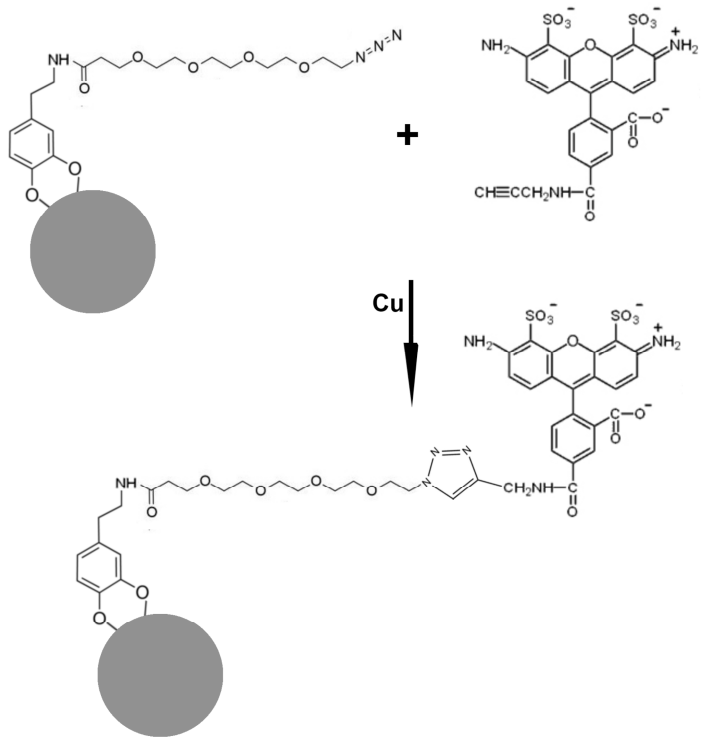

Figure 3.5. Schematic Diagram of CLICK labeling. Steps of *in situ* chemical reaction between azide-PEG_4-dopamine (MWT426.47) conjugated to the surface of TiO_2 nanoparticle (gray circle) and alkyne-modified Alexa-Fluor 488. This CLICK reaction is done in presence of Cu *in situ*, in permeabilized cells.

Nanoparticle (dispersant)	Zeta Potential	Hydrodynamic Diameter
Bare NPs (1:200) dH2O	-34.07 ± .91	364.7 ± 18nm
NP-azide (1:200) dH2O	-31.30 ± .78	387.9 ± 79nm

Table 3.1. Zeta Potentials and Dynamic Light Scattering of NPs. Bare TiO_2 nanoparticles and azide-coated nanoparticles were diluted 1:200 in water and their hydrodynamic diameters and zeta potentials measured. Due to aggregation and the non-spherical shape of aggregates, sizing data obtained were deemed not reliable and cryo TEM images were used for nanoparticle sizing.

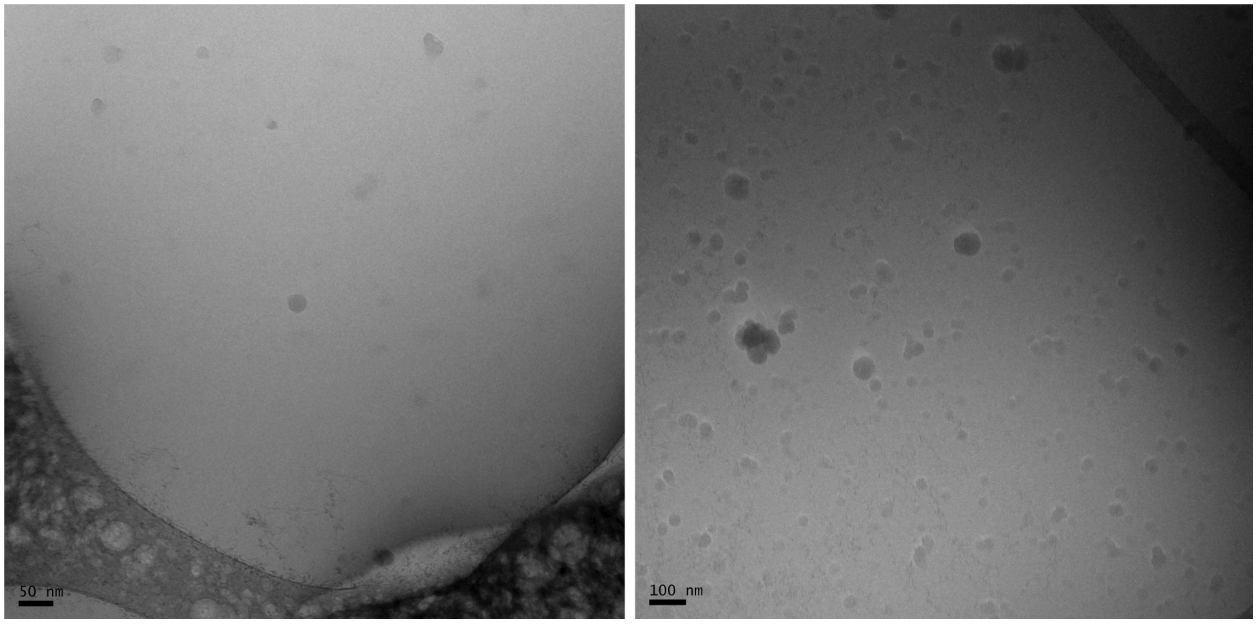

Figure 3.6. Cryo-TEM images of bare and dopamine-azide coated TiO2 nanoparticles. Bare TiO_2 nanoparticles and azide-coated nanoparticles were diluted 1:50 in distilled H_2O, plunge frozen in liquid ethane and imaged. Compared to uncoated nanoparticles (left), azide-coated (right) nanoparticles and aggregate sizes appear slightly increased.

HeLa cells grown on microscope slides and serum-starved for 1h were treated with azide-coated nanoparticles for 1h because we have noticed previously that non-specific uptake of nanoparticles is already substantial at this nanoparticle concentration [19]. Initially, in order to obtain a quick confirmation that new fluorescent staining matches the pattern that would be obtained by already established fluorescent dyes, we added ARS to azide-coated nanoparticles and used these doubly coated nanoparticles for cell labeling (Figure 3.7). The overlap between ARS and Alexa Fluor 488 fluorescence we obtained was encouraging, therefore we proceeded to optimize the CLICK reaction.

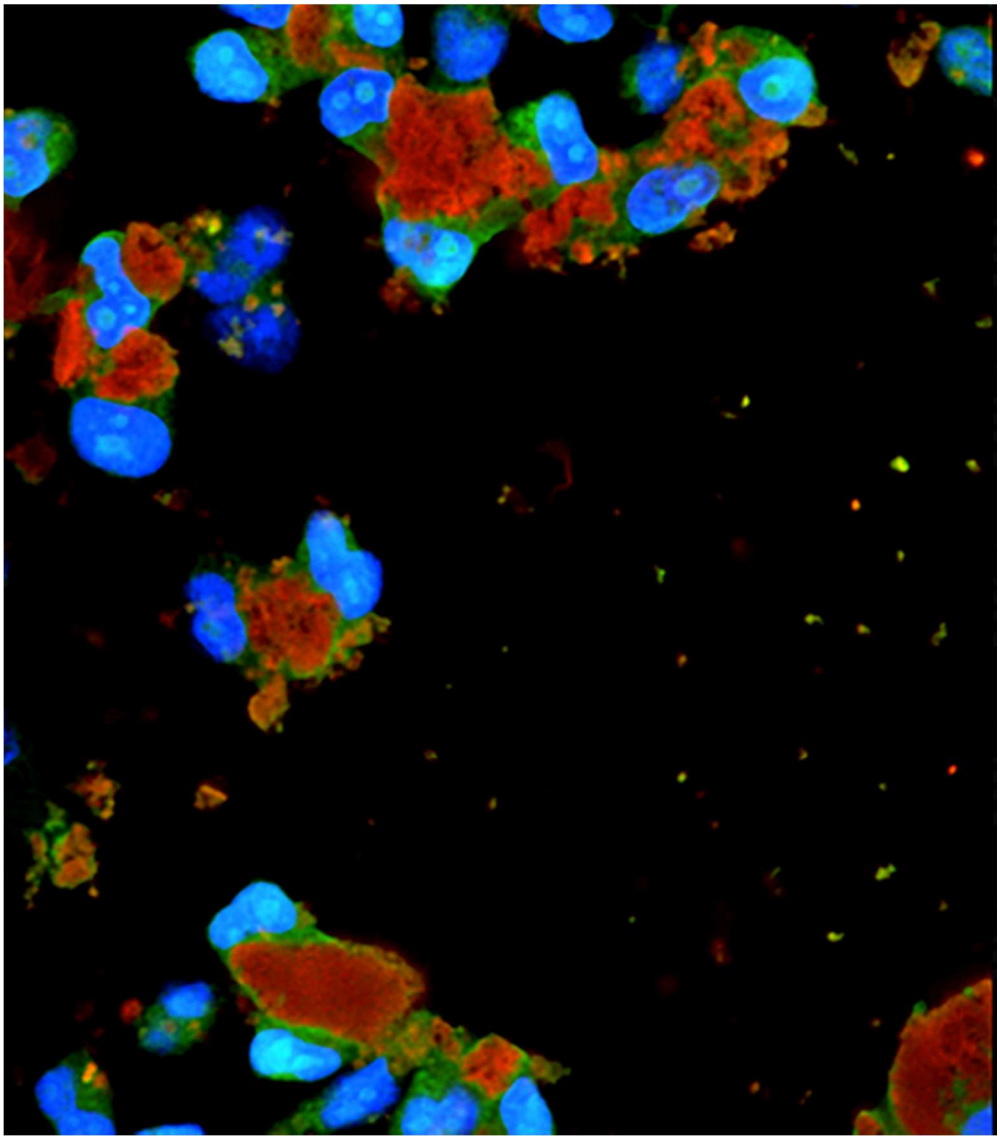

Figure 3.7. Cells treated with nanoparticles simultaneously coated with ARS and dopamine-azide and stained *in situ* by CLICK reaction with Alexa-Fluor 488 alkyne. The high nanoparticle concentration in this experiment (20 fold higher than e.g. in Figure 3.8) lead to the formation of substantial cell associated aggregates. This thickness of nanoparticle deposits was not compatible with proportional CLICK labeling; therefore, only those areas of nanoparticle aggregates that are relatively thin show an obvious red (ARS) and green (Alexa-Fluor 488) fluorescence overlap. Importantly, this early experiment has also shown that a CLICK reaction with Alexa-Fluor 488 alkyne may result in weak staining of nucleoli. In our subsequent experiments, we have decreased nanoparticle concentration and refined CLICK reaction (1500x dilution of Alexa-Fluor 488 alkyne) to develop the procedure used in subsequent experiments.

Our focus in the next set of experiments was to obtain minimal Alexa Fluor 488 background coupled with bright labeling of nanoparticle aggregates *in situ* (Figure 3.8). We noted that oversaturation of cells with the alkyne-modified fluorophore (alkyne-Alexa 488) can produce background despite the lack of azide groups in nanoparticle-free cells; therefore, we fine-tuned the labeling reaction to prevent non-specific background fluorescence in untreated cells. Cells without nanoparticles (untreated) exhibited a very dim fluorescent signal (Figure 3.8) that was easily recognized as background, non-specific fluorescence. Comparatively, cells with azide-coated TiO_2 nanoparticles showed a strong fluorescent signal when excited with a 488-nm laser (Figure 3.8). Using these experimental conditions, we noticed even subtle differences in treatment and staining conditions such as a two-fold increase in concentration of alkyne-Alexa 488 or a twofold increase in concentration of nanoparticles (Figure 3.8). Thus, for example, we noticed little difference in the Alexa 488 background when two different concentrations of alkyne-Alexa 488 were used and at the same time noted much stronger signal intensity in nanoparticle-treated cells. Similarly, doubling the nanoparticle concentration increased the volume of Alexa 488-positive pixels in nanoparticle-treated cells (Figure 3.8). We proceeded to test these signal intensity differences more quantitatively using Nikon Elements software (Table 3.2). The data about pixel numbers and signal intensities confirmed our visual impressions.

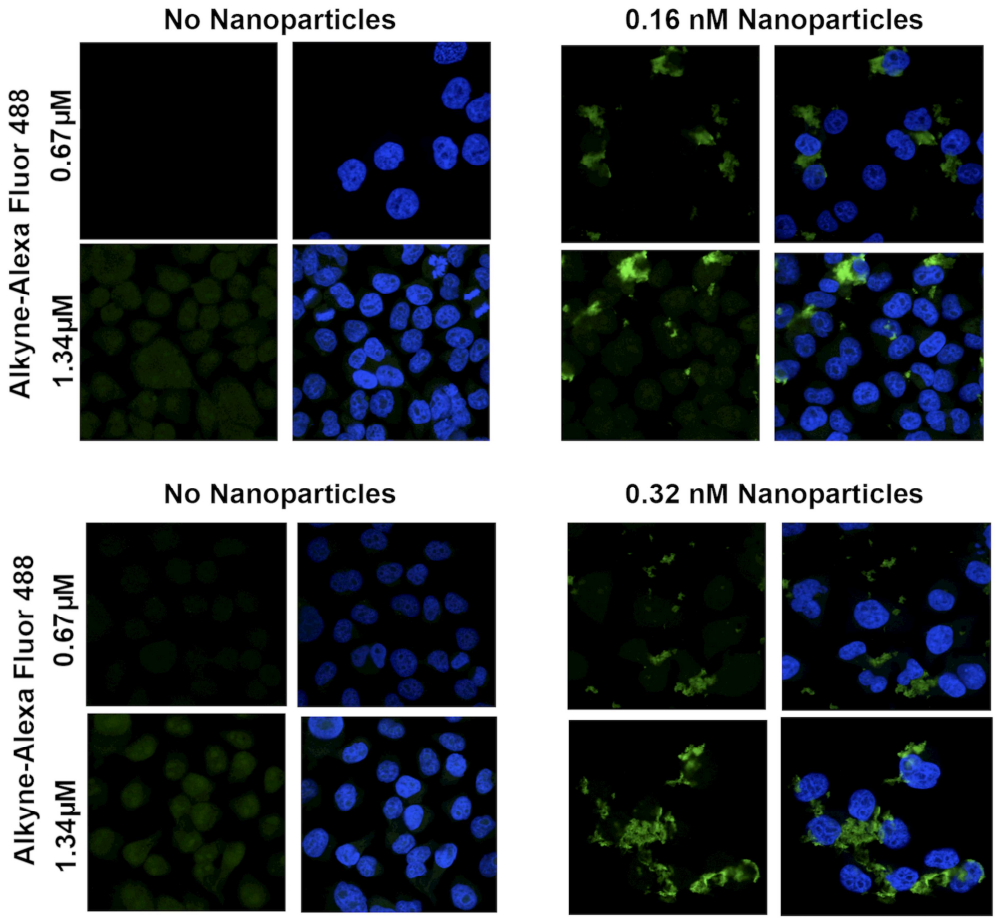

Figure 3.8. Labeling specificity of CLICK reaction. Increased concentration of alkyne Alexa-488 increases fluorescent signal intensity of nanoparticle aggregates in nanoparticle treated cells (right hand panels), while increased concentration of nanoparticles leads to greater nanoparticle uptake (bottom right panels). Cells not treated with nanoparticles (left panels) have low background Alexa-488 signal under the same staining and imaging conditions.

Alkyne-Alexa Fluor 488 Concentration	Nanoparticle Concentration			
	No Nanoparticle		0.16 nM Nanoparticle	
	Nucleus Hoechst area/Alexa area	Alexa signal mean intensity	Nucleus Hoechst area/Alexa area	Alexa signal mean intensity
0.67 µM	0.533039984	27.05	1.713822631	655.4
1.34 µM	0.319612203	110.8	0.749564841	346.48
	No Nanoparticle		0.32 nM Nanoparticle	
	Nucleus Hoechst area/Alexa area	Alexa signal mean intensity	Nucleus Hoechst area/Alexa area	Alexa signal mean intensity
0.67 µM	0.534795386	304.05	3.978723404	1129.95
1.34 µM	0.505167368	330.91	1.235462941	1026.54

Table 3.2. Quantitative analysis of fluorescent intensity in images presented in Figure 3.8. We analyzed the fluorescent intensity signals of Hoechst and Alexa-488 in samples presented in Figure 3.8 in several different ways. Considering that the non-specific Alexa staining can be expected throughout the cell in nanoparticle free samples, we predicted that the ratio of Hoechst stained areas divided by Alexa-488 stained area will be close to 0.5 in nanoparticle free samples. On the other hand, in nanoparticle treated samples, nanoparticles absorbed majority of the Alexa-488 and concentrated this signal into a smaller area and the ratio of nucleus vs. Alexa stained area increased (because Alexa stained area decreased to the area containing nanoparticles). Mean intensity of Alexa signal at each nanoparticle concentration increased more (in comparison to matching control) at lower azide Alexa 488 concentration, although total Alexa signal intensity was higher in samples containing more nanoparticles.

Several factors were considered in this analysis. For example, in cells without nanoparticle treatment ratio of nucleus associated pixels vs. Alexa associated pixels was close to 0.5 suggesting a diffuse staining of whole cells by the alkyne-Alexa 488 detector molecule. In contrast, in cells treated with azide coated nanoparticles the ratio of Hoechst stained areas to Alexa-488 stained areas were greater than 0.5 suggesting staining specificity (Table 3.2). Furthermore, mean per pixel Alexa-488 signal intensity was about 3 times higher in cells treated with azide-coated nanoparticles then in matching no nanoparticle controls; this difference was slightly less dramatic in cells stained with higher concentration of click reagent.

The final refined procedure for CLICK labeling of nanoparticles *in situ* yielded a bright signal and low background; however, it was important to confirm that the bright green signal shown in Figures 3.7 and 3.8 entirely depends on the presence of nanoparticles. For the ultimate confirmation of the presence of nanoparticle, we used XFM. In the period between experiments shown in Figures 3.1 and 3.2, and at present, the APS Synchrotron obtained a new, higher resolution instrument for XFM—the Bionanoprobe [20, 40]. As detailed in the Experimental section and described in Chapter 2, the X-ray beam focus of the Bionanoprobe is several fold better than that of the X-ray microprobe instrument at sector 2ID-D used to obtain XFM data in Figures 3.1 and 3.2. We decided to image the same sample by both confocal microscopy and then by XFM at the Bionanoprobe, replicating the work performed with biotin-FITC – streptavidin nanoparticles. In this case, cells were grown on silica nitride windows, processed, imaged by optical microscopy as if on glass slides, and finally washed, dehydrated by ethanol, and air dried as it was performed earlier. This approach for sample preparation is suboptimal with regard to both preservation of cell morphology and preservation of native cellular elemental

components, but the nanoparticle localization inside the cell remains unchanged. Thus, we anticipated that the only clear elemental signals from the cell would be phosphorus (indicating cell nucleus) and titanium (indicating nanoparticles); this was confirmed as anticipated, with an additional finding that copper from the CLICK reaction also incorporated into the cellular matter, providing (as an artifact) a clear cellular outline (Figure 3.9). As anticipated, the Alexa Fluor 488 signal from confocal microscopy within the cell cytoplasm matched well with the Ti signal obtained by XFM (Figure 3.9). More importantly, maximum per-pixel intensity of Ti in this image was 3.89 micrograms per cm^2, seven times lower than the maximum signal in Figure 3.1, while at the same time, signal for P differed only by threefold. Although some of these elemental signal differences could be ascribed to a different way of sample preparation, it is still likely that the cells in Figure 3.9 contain less TiO_2 than their counterparts in Figures 3.1 and 3.2. However, at the same time, confocal fluorescence signal intensity is much clearer in Alexa Fluor 488 CLICK-labeled samples (Figure 3.9) than in FITC-labeled cells (Figures 3.1 and 3.2). Therefore, CLICK chemistry provides staining not only lower in background but also more sensitive labeling for nanoparticles.

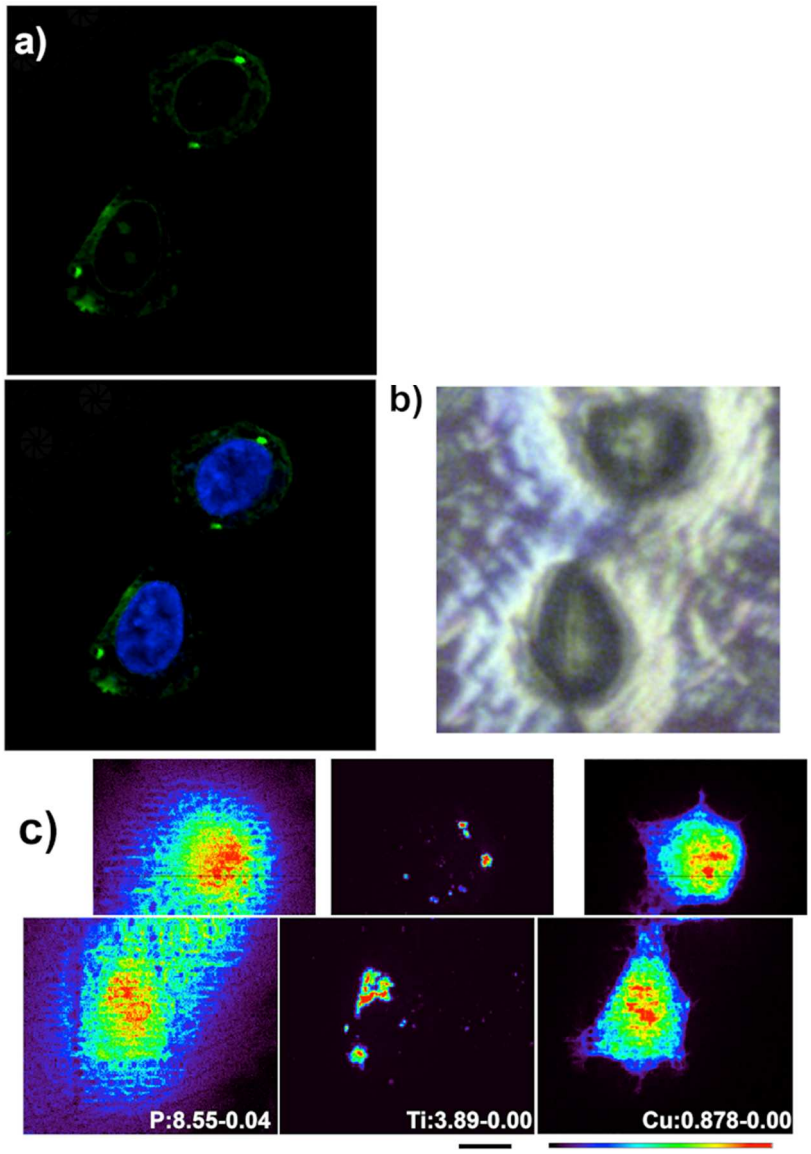

Figure 3.9. Confocal microscopy of nanoparticles using CLICK chemistry and XFM elemental mapping of titanium in cells. Cells seeded on Si_3N_4 windows, a substrate suitable for XFM, were treated with nanoparticles, labeled by CLICK and stained by Hoechst to be imaged by confocal microscopy (a). Next, cells were rinsed with PBS, dried (b) and subjected to XFM at a high resolution XFM instrument–Bionanoprobe (c). a) Optical microscopy, confocal image of the cell pair that was investigated by XFM; b) Dried Si_3N_4 window with the same pair of cells air-dried on its surface c) high resolution XFM images (beam size of ~85 nm; pixel size 100 nm) of the two cells. Element and maximal elemental concentration in micrograms per cm^2 are given in white letters. Scale bar (black) is 2 microns; color scale defines false colors map with minimal signal in black and maximal signal in red.

3.6 Conclusions

Three new approaches for labeling of TiO_2 nanoparticles *in situ* were tested and two of them developed for labeling for confocal microscopy and successfully confirmed by XFM. Although confocal fluorescence imaging and XFM imaging are not easily paired with each other, we managed to preserve the integrity of substrates (fragile formvar-coated TEM grids and Si_3N_4 windows) carrying some of the cells (many detached in the process of multiple manipulations) imaged by confocal microscopy. Thus, dual imaging was achieved, and it confirmed that the fluorescent signal and the metal oxide (elemental) signal are co-registered. XFM imaging of cells pre-screened by confocal microscopy has been accomplished only once before to our knowledge [8], showing that, as in this case, Ti signal obtained by XFM spans the entire cell volume, while confocal microscopy provides images of nanoparticles only in a given optical slice [8]. An excellent overlap was found between optical fluorescence signals (FITC and Cy3 in one case and Alexa 488 in the other) and the position of Ti in XFM-generated elemental maps. This suggests that the following can be achieved: (1) successful labeling of nanoparticles with optically competent dyes; (2) retention of fluorescent dyes on nanoparticles during cell treatments; and (3) washing out and removing sources of non-specific optical fluorescence from nanoparticle-treated cells pre- or post-stained with optically fluorescent dyes.

Labeling based on the use of FITC-biotin and streptavidin is often associated with a slightly higher background fluorescence due to the interactions between streptavidin-Cy3 and endogenous, not-nanoparticle-bound biotin. It is possible that such background could be decreased by pre-treating cells with streptavidin or neutravidin, which have been used to reduce endogenous biotin *in vitro* [114] and *in vivo* [115]; nevertheless, in this case it is possible that

residual non-labeled avidin-like molecules could interact with the nanoparticles as soon as they enter the cells and reduce subsequent labeling with fluorescent avidin-like compounds.

In order to detect TiO_2 nanoparticles *in situ* and do so with a single step without background fluorescence and without concern that biotin import into cells may be triggered, we developed a CLICK chemistry approach for labeling and detecting TiO_2 nanoparticles *in situ*. The copper-catalyzed azide–alkyne cycloaddition, also known as a CLICK reaction, was developed in 2008, and the following year it became a method of choice for use with biological samples [116, 117]. In nanotechnology, specifically with TiO_2 nanoparticles, CLICK chemistry was used for the preparation of hybrid nanomaterials [118-121]. In biology, CLICK chemistry reactions have been used for various cell biology and biomedical applications; the virtual absence of azide-carrying moieties in cells makes this an excellent approach for labeling with low background [122]. Specifically, several CLICK-based techniques were developed to investigate post-translational protein modifications to identify newly synthesized proteins and to examine DNA replication in proliferating cells [123-125]. During the reaction process, a stable triazole forms in the course of a copper-catalyzed reaction between azide and alkyne moieties; this can be exploited as a simple chemical reporter to label and detect biomolecules of interest.

Commercially available kits such as those from Life Technologies can be used for labeling of nucleic acids and proteins in combination with different “standard” cell biology techniques [56]. We used components from one of such kits to label azide groups, which were attached to the nanoparticle itself, with Alexa Fluor 488 alkyne in order to label *in situ* azide-conjugated TiO_2 nanoparticles with Alexa Fluor 488. CLICK chemistry staining showed the high signal intensity of Alexa Fluor 488 in confocal imaging without prominent background

fluorescence, thereby permitting accurate intracellular detection of even small nanoparticle aggregates. There was an evident overlap between the strong fluorescent signal of Alexa Fluor 488 within the cytoplasm (Fig. 8), and the XFM detected localization of Ti. It is worth mentioning that the molecular weight (M_W) of azide-PEG_4-dopamine is about 400, while the M_W of molecules used for targeted nanoparticle coating generally exceeds this by several fold. For example, the M_W of B-loop peptide dopac conjugate we used previously is close to 1500 [20]. It will remain to be evaluated whether azide-PEG_4-dopamine may interfere with nanoparticle targeting or not and whether access to the azide group may be affected by the presence of targeting molecules on the nanoparticle surface. Considering the large surface area of nanoparticles and the fact that B-loop peptide covered no more than 30% of the nanoparticle surface for successful targeting [20], adapting the nanoparticles for targeting and *in situ* staining should be easily accomplished.

A chemical reporter labeling technique such as CLICK chemistry as an *in situ* staining approach has clear advantages over the use of nanoparticles labeled with fluorescent molecules prior to cell treatment. Moreover, the availability of alkyne-conjugated fluorescent dyes is increasing, allowing for more flexibility in the choice of detection molecules. CLICK chemistry itself is simple, highly selective, efficient, and reproducible. Finally, similar staining and detection techniques could be applicable to other metal oxide nanoparticles like iron oxide, which also has a high affinity for dopamine [126, 127].

Nevertheless, because CLICK chemistry reactions introduce a substantial amount of copper into cells (Fig. 8), the elemental content of cells treated by CLICK chemistry shows high Cu content as an artifact. It is possible, nevertheless, that a copper-free CLICK reaction can be

used instead of the approach used here. Although CLICK chemistry may be suitable in most situations, a dual labeling approach such as the biotin-streptavidin labeling approach described in the present study has utility in pre- and post-detection studies, specifically in nanoparticle studies that requires labeling through hydroxyl groups.

In conclusion, the results of this study show that it is feasible to label TiO_2 nanoparticles both sequentially by biotin-FITC and then *in situ* by fluorescent streptavidin as well as strictly *in situ* by CLICK chemistry. Both approaches are capable of detecting TiO_2 nanoparticles intracellularly through optical fluorescent microscopy. Importantly, these labeling techniques can be used as post-treatment labeling techniques (Figure 3.10) to detect TiO_2 nanoparticle internalization, localization, and activation. To the best of our knowledge, this is the first report on TiO_2 nanoparticle detection using CLICK chemistry coupled with XFM (Figure 3.11). In this study, we used XFM to confirm that fluorescent signals are indeed co-localized with the nanoparticles; however, in the future, only confocal microscopy can be performed, especially with CLICK chemistry-labeled nanoparticles. This will increase throughput for nanoparticle imaging *in situ*, facilitating the evaluation of nanoparticles in a variety of cell biology scenarios.

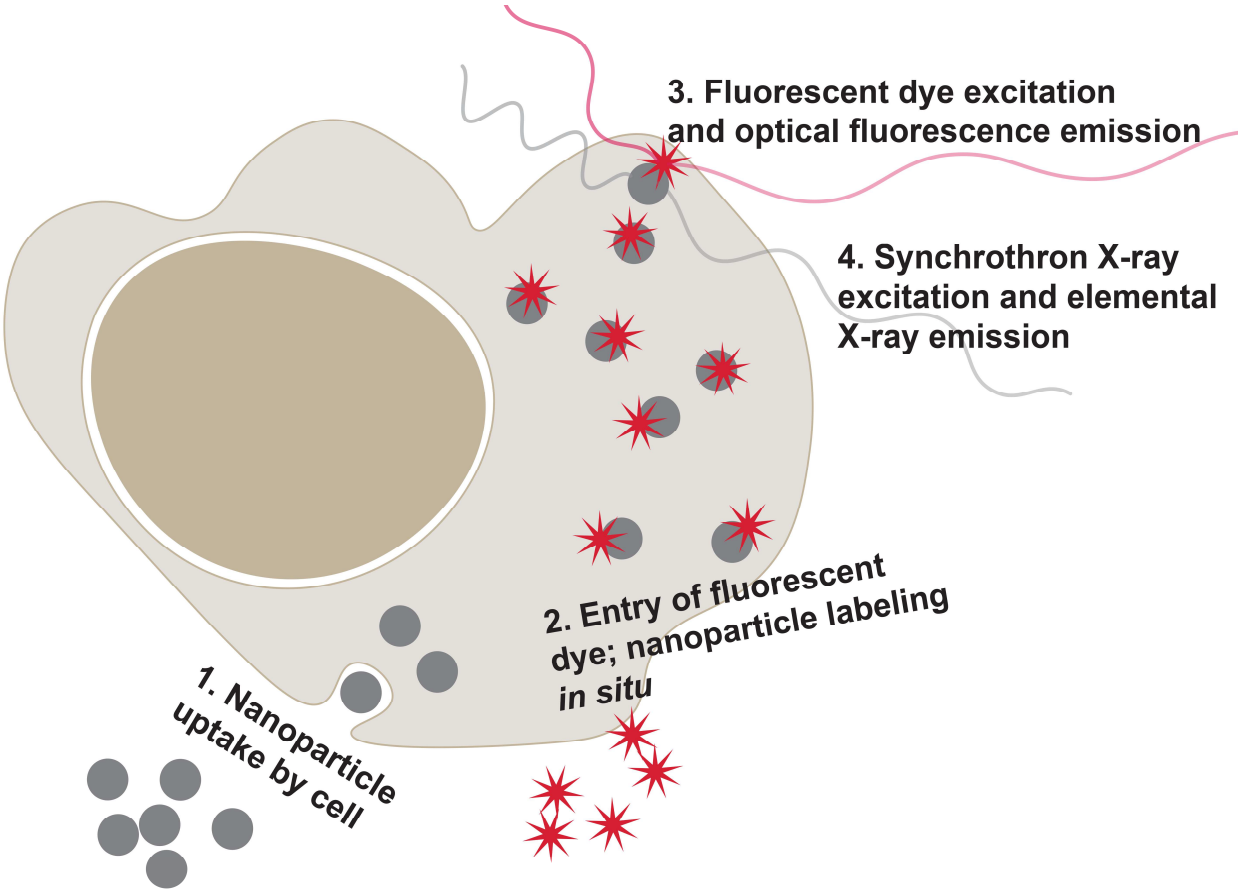

Figure 3.10. Schematic explanation of the benefits of nanoparticle post labeling. TiO_2 nanoparticles have low natural contrast; two novel ways to label them *in situ* to enable optical microscopy were developed, both based on standard tools used in cell biology. In each case, visible fluorescence was achieved *in situ* in cells fixed after nanoparticle uptake; specificity of labeling was confirmed by X-ray fluorescence microscopy.

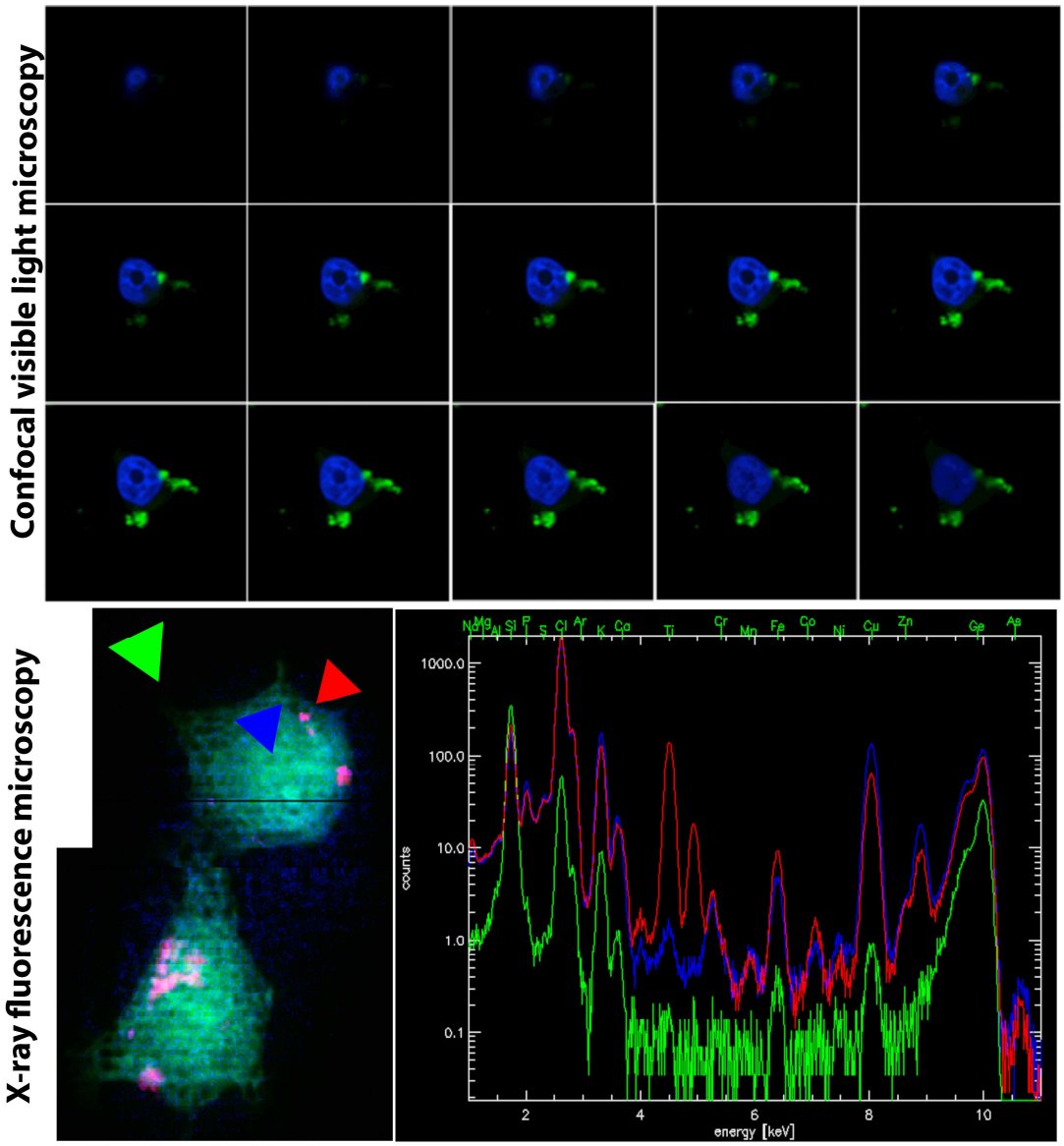

Figure 3.11. Both confocal microscopy and XFM were used in order to understand the distribution of CLICK labeled nanoparticles in cells. Confocal visible light microscopy shows distribution of nanoparticle aggregates in cells (top row); XFM mapping and elemental analysis of different image regions show that, for example, signal intensity of silica (sample substrate was Si_3N_4) is the same in any region of interest: background (green), cytoplasm (blue) or cytoplasmic nanoparticle aggregates (red). On the other hand, in the area of the image corresponding to cytoplasmic nanoparticle aggregates, K alpha and K beta Ti lines show much higher peaks then in cytoplasm or naked substrate, while, for example Fe signal has the same peak intensity in all cytoplasmic regions (with or without nanoparticles).

CHAPTER 4: Nanoparticle Induced Cellular Stress

4.1 Introduction

The physical and chemical properties of nanomaterials and their distinct differences from biological molecules upon internalization by cells or tissues open new avenues for cancer treatments. Specifically, stress increasing nanoparticles are of interest in radiation oncology since radiation therapy is used in treating more than 50% of all cancers. Targeted and stress causing nanoconstructs that improve the effects of radiotherapy are of great interest in the field. Nanomaterials respond to ionizing radiation differently than biological molecules. While chemical bonds of most organic polymers suffer radiation damage, inorganic nanomaterials can accept or release electrons and photons without significant structural changes following radiation exposure. Moreover, depending on their surface modifications, the same nanostructures sometimes have a variety of effects on their immediate biochemical and biological surroundings (Figure 4.1).

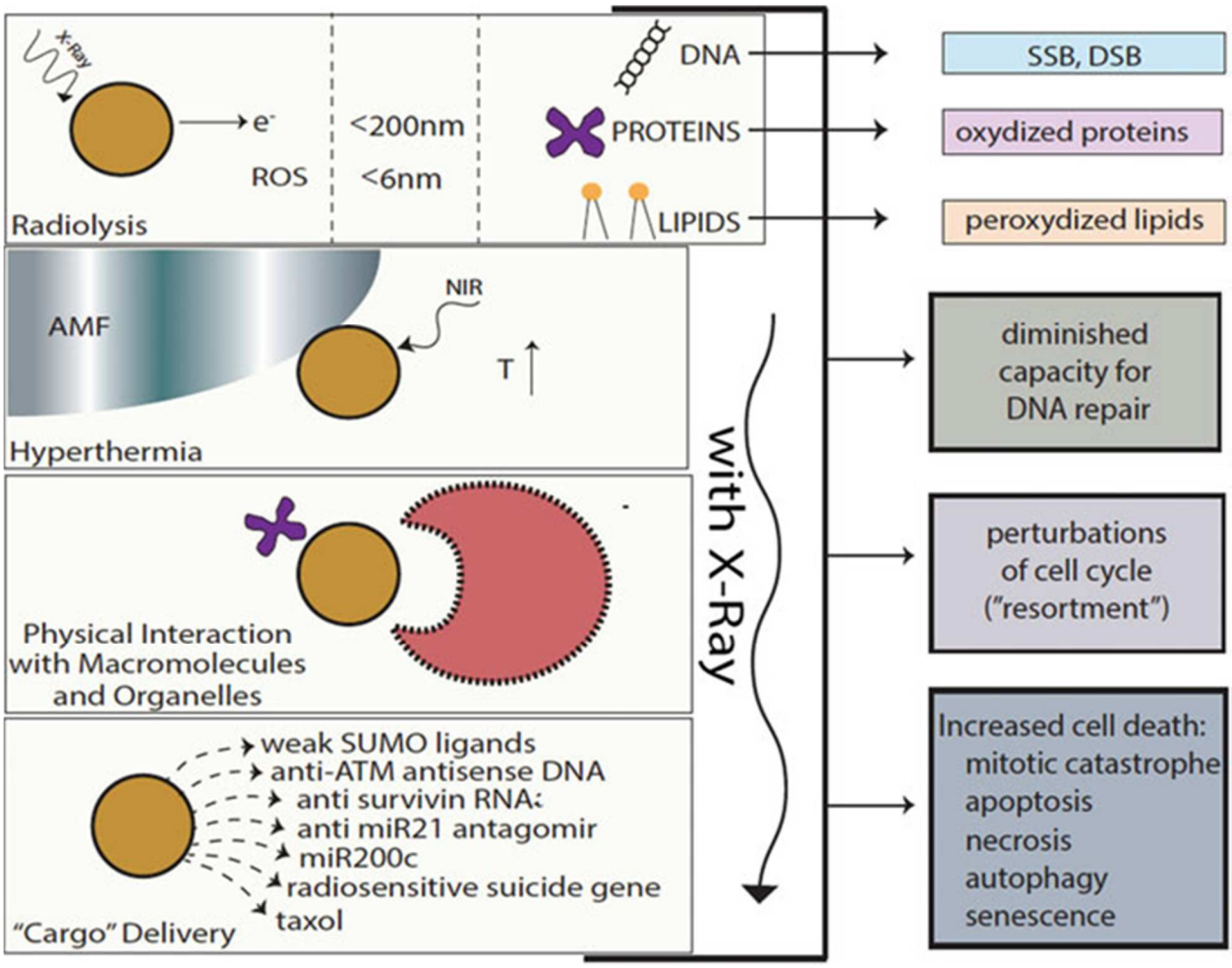

Figure 4.1. Nanoparticle Induced Pathways to Increased Cell Death. Two general paths toward nanomaterial enabled radiosensitization have been explored: 1) improving the effectiveness of ionizing radiation and (2) modulating cellular pathways leading to a disturbance of cellular homeostasis, thus rendering the cells more susceptible to radiation-induced damage [128].

4.2 Nanoparticle-induced Cell Injury

Nanoparticles induce cellular stress in a number of ways. Cellular stress in many cases leads to cell death. For example, copper oxide nanoparticles were found to increase autophagy and apoptosis [129] while palladium nanoparticles primarily induce apoptosis [130] and platinum nanoparticles prevent DNA replication [131].

The effect of nanoparticles on cells is largely modulated by their acquisition of a protein corona and the subsequent intracellular modification of such corona through interactions with intracellular proteins. An *in vitro* study by our laboratory found that several different sizes of polyethylene glycol and tetraethylene glycol-coated iron oxide and titanium dioxide nanoparticles interact with proteasome and alter its activity [132]. Similarly, protein corona of silica nanoparticles was found to contain proteasomal subunits [133]. Considering that ubiquitin proteasome system regulates DNA synthesis and repair [134], it is possible that the rate of DNA repair in cells exposed to these nanomaterials is also altered.

In addition, pre-designed surface modifications on nanoparticles can change native or normal cellular processes thereby inducing cellular stress. For instance, DNA repair can be deliberately modified by NPs. For example, Li and others modified 2 nm gold nanoparticles by the addition of weak SUMO (Small Ubiquitin-like Modifier)-2⁄3 ligands, at a density of 100 per particle [135]. Through this approach, (because of high density of a weak ligand on the particle surface) nanoparticles became able to interact with multiple SUMO molecules in a poly-SUMO chain; inside cells these constructs were found both in cytoplasm and nucleus. Because SUMOylation is a very important molecular modification pathway in the oxidative stress response, use of this type of nanoparticle, in comparison to same type of nanoparticles without

SUMO ligand, led to delayed DNA repair detected by comet assay of breast cancer MCF7 cells exposed to ionizing radiation. Similarly gold nanoparticles inside cells have been shown to deregulate cellular homeostasis in ways that increase ER stress and decreased capacity for DNA damage repair [136]. ER stress is itself responsible for Rad51 degradation and general suppression of DNA DSB repair [137].

Nanoparticle induced perturbation of the cell cycle is an emerging area of research. A recent study using prostate carcinoma cell line DU-145 has documented changes in cell cycle following treatment with 10 nm gold nanoparticles coated with 6-deoxy-6-fl uoro-1-thio-D-glucose (Glu-GNPs) [138]. Glu-GNPs triggered activation of the cyclin dependent kinases and cell accumulation in the G2/M phase at 29.8% versus 18.4% for controls at 24 h. This activation lead to cellular sensitization to ionizing radiation. Similarly, an increased number of cells in G2/M phase of cell cycle was noted in glioblastoma cells (SNB-19 and U87MG) in culture after treatment with titanium dioxide nanotubes [139]. Moreover, in this study it was noted that the DNA repair was reduced in glioblastoma cell lines after they engulfed TiO_2 nanorods. As nanorods remained in vesicles inside the cytoplasm in these cells, the mechanism(s) responsible for these changes in cellular homeostasis are as of yet unclear. Many possible avenues for speculations about decrease of DNA repair in this work can be envisioned. Perturbation of cell cycle by nanomaterials, however, does not always lead to increased numbers of cells in G2/M phase of the cell cycle. On the contrary, Mackey and El-Sayed conjugated gold nanoparticles with nucleus- and cytoplasm-targeting peptides cells and found an accumulation of cells in the S phase with a depletion of cells in the G2/M phase in human oral squamous carcinoma (HSC-3) [140]. Cells are the most radiation sensitive in G2/M phase of the cell cycle, so cell cycle

perturbations that would increase cell numbers in this part of the cell cycle would be the most beneficial as radiation sensitizers.

4.3 Conclusions

Nanomaterials have been shown to have physical and chemical properties that have opened new avenues for cancer diagnosis and therapy. Nanoconstructs that enhance existing treatments for cancer, such as radiation therapy, are being explored in several different ways. Two general paths toward nanomaterial enabled radiosensitization have been explored: (1) improving the effectiveness of ionizing radiation and (2) modulating cellular pathways leading to a disturbance of cellular homeostasis, thus rendering the cells more susceptible to radiation-induced damage (Figure 4.1). A variety of different nanoparticle agents that work via one of these two approaches have been explored, many of which modulate direct and indirect DNA damage and different cellular pathways. There have been many *in vitro* successes with the use of nanomaterials for radiosensitization, but *in vivo* testing has been less efficacious, predominantly because of difficulty in targeting and localizing nanoparticles. There have been some exceptions such as Au nanoparticles in mice [141]. As methods for tumor targeting improve, it is anticipated that nanomaterials can become clinically useful radiosensitizers for radiation therapy. However, precisely because they cause cellular stress without necessarily causing cell death, nanoparticles may be expected to lead to development of somatic mutations and some of these could lead to development of new cancers. Toxicology research of this type, however is still in its infancy.

CHAPTER 5: HPV associated Head and Neck Cancer

(Poropatich, K., Paunesku, T., Brown, K., Mittal, B. and Woloschak G. E. The elemental composition of HPV associated Head and Neck Cancer *(In preparation)*

5.1 Introduction

Similar to nanoparticles, viruses cause cellular stress; unlike nanoparticles, connections between viruses and cancer have been known for some time. As much as 15% of global cancer cases are attributed to infections [142]. Viruses directly contribute to cancer through various mechanisms [143, 144]. Direct mechanisms of virally induced carcinogenesis include cancer caused by genomic perturbations introduced by incorporation of viral genomes and virally induced changes of cellular homeostasis through generation of genomic instability, increase in the rate of cell proliferation, resistance to apoptosis and alterations in DNA repair mechanisms.

5.2 Viruses and Cancer

The remainder of this chapter will focus on human papillomavirus (HPV). Human Papillomavirus (HPV) is a double-stranded, non-enveloped DNA virus that encodes 8 viral proteins that infects epithelial type cells, especially keratinocytes [145]. Over 100 types of HPV have been identified and are divided into low risk and high risk groups based on their capacity to drive malignant transformation. HPV16, 18, 31, 33, 35, 39, 45, 51, 52, 56, 58, 59, 68, 73 and 82 are high risk types of HPV [146]. High risk HPV types have been found to cause cervical, neck, anal, vaginal, vulva, and penile cancers [147]. HPV oncogenes E6 and E7 increase cell proliferation and resistance to apoptosis, disrupt cell cycle checkpoints, compromise DNA repair functions. This is turn leads to increases in DNA mutations, and genomic instability which lead to malignant conversion [148-150]. Human papillomavirus (HPV) infection alone is not sufficient for the development of cancer. Only a small percentage of HPV infections leads to invasive tumor growth suggesting that viral oncogene expression is not sufficient for cancer to

occur and that other cellular events are necessary. Therefore, cell cycle dysregulation and genomic instability caused by HPV allows cells to acquire additional mutations required for malignant transformation.

The molecular mechanisms surrounding the role of HPV in cancer development are several. It is believed that viral protein E6 binds to and leads to ubiquitination of p53 a well-known tumor suppressor protein. p53 is a mediator of apoptosis and plays an important role in stimulating cell cycle arrest after DNA damage [151]. Mutations in p53 gene are frequent in most malignancies. In fact, it is estimated that p53 gene mutations occur in nearly 50% of tumors [152]. In cells with DNA damage, p53 arrests the cell cycle until the damage has been repaired. If this does not occur, p53 induces apoptosis or senescence. None of these events can occur in cells that express HPV protein E6. Binding with E6 leads to degradation of p53 protein through ubiquitination and the cells with E6 expression are functionally equal to cells that have lost p53 gene through e.g. loss of heterozygosity.

HPV protein E7 targets the retinoblastoma 1 protein (pRb) for degradation [153], causing increased cell proliferation and overexpression of p16 protein through a disrupted feedback loop [154]. pRb arrests cell cycle progression after binding and inactivating members of the E2F family of transcription factors [155]. pRb specifically inhibits the G1-S transition in response to DNA damage.

Uncontrolled cell division and accumulation of mutations and chromosomal abnormalities are increased in the absence of either p53 or pRb proteins; all of these effects can be expected in cells infected with HPV. Importantly, DNA damage induces expression of viral proteins E1, E6, and E7 [156-159] ; their presence coupled with DNA replication and DNA

double-strand breaks promotes viral integration [160-162]. Although DNA integration is not a part of the normal HPV life cycle, high-risk HPV (HR-HPV) DNA is often integrated into the human genome [163]. The sites of integration are distributed throughout the genome at sites where DNA double strand break repair failed [164]. A recent study reported a direct association between HPV integration and host genomic instability [165]. Additionally, E6 and E7 proteins from high risk HPVs such as HPV16 promote gene amplification, structural chromosomal alterations and centrosome replication errors leading to aneuploidy and polyploidy. Thus, HPV immortalized cell lines often show gain and loss of whole chromosomes [166, 167].

5.3 HPV and Head and Neck Cancer

Head and neck cancer (HNC) cases account for over 500,000 global cancer cases annually [168]. The most common type of HNC is head and neck squamous cell carcinoma (HNSCC), which includes cancers of the oral and nasal cavity, larynx, hypopharynx, and oropharynx. HNC is typically associated with tobacco use and alcohol consumption; however, in recent years HPV has been increasingly implicated as the causative agent of HNC [169]. In 2008, human papilloma virus (HPV) was thought to be the causative agent in up to 20% of all HNSCC, particularly of the oropharynx, originating in the tonsil or at the base of the tongue, and since then that number has been increasing at a rate of 0.8% annually as the percentage of cases attributed to smoking and alcohol are slowly declining [170-173]. Oropharynx (OPC) tumors account for approximately 60% of all HNC cases [174-176] and approximately 50%-80% of OPSCC's are associated with HPV-positive status [177, 178]. It is estimated that HPV will

eventually become the primary etiology for head and neck cancer in the United States. This category of HNC will be the main topic for further discussion.

HPV-positive (HPV+) HNC tumors are distinctly different from HPV-negative (HPV-) HNC tumors. Patients with HPV+ tumors are younger in age, often non-smokers, and non-alcohol drinkers [176]. Despite a more aggressive clinical presentation, HPV status is the strongest predictor of localized cancer and predictor of loco-regional control (LRC), decreased risk of recurrence regardless of age, stage, or gender and overall survival (OS) [179-184]. Specifically, HPV+ OPCs have a 58% reduction in mortality risk and a 62% lower risk of cancer progression compared to HPV- tumors [181, 182].

5.4 Radiation response differences between HPV+ and HPV- HNSCC

One explanation for improved clinical outcomes seen in HPV+ HNC (specifically oropharyngeal cancer) is an increased sensitivity to chemotherapy and radiation treatment [182, 183, 185, 186]. Conversely, HPV- tumors carry frequent p53 mutations that confer chemoradioresistance [187]. DNA mutations in HPV+ and HPV- HNSCC cell lines occur by different mechanisms, which illustrates the reasons for the increased treatment sensitivity of HPV+ OPCs [188]. The enhanced responsiveness to radiation and chemotherapy of HPV+ cancer cells may be caused by cell cycle dysregulation and impaired DNA repair. For example, HPV protein E6 induces p53 degradation which in turn leads to failure to express p21 in response to DNA damage which in turn does not arrest the cells to allow them to repair the DNA [144, 147]. Irradiated HPV+ cell lines progress faster through S-phase, showing a more distinct accumulation in G2/M phase of the cell cycle. The abnormal cell cycle checkpoint activation is

accompanied by a more pronounced increase in cell death after irradiation. HPV+ cell lines are more sensitive to radiation than HPV- cell lines, possibly due to radiation-induced cell cycle arrest [189]. In HPV+ (and p16+) head and neck cancer patients, p16 expression correlates with radiation sensitivity. Furthermore, studies have shown that HPV+ tumors are more sensitive to DNA-damaging agents than HPV- tumors [190].

While the relationship between HPV-induced oncogenesis, tumor sensitivity to radiotherapy, and improved clinical outcomes is still being investigated, the standard treatment for HPV+ and HPV- OPC continues to be similar. The combination of better prognosis and younger age of HPV+ OPCs has led to increasing interest in treatment de-escalation and to the development of HPV status specific therapies. Thus, many patients with HPV+ OPC may not require the aggressive radiotherapy given to HNSCC patients today. It is expected that new recommendations for treatment strategies for HPV+ cases will include dose reduction for radiotherapy. Nevertheless, prospective trials are under way to determine whether therapy can be stratified solely on the basis of HPV status [191-193].

5.5 HPV and XFM

Radiation treatment is a standard of care for more than 50% of all cancer patients; however, variation in response to therapy is significant. Healthy tissues and organs differ in radiation sensitivity, but the same organ generally has similar sensitivity to irradiation in healthy human population. Cancer cells on the other hand, often differ from each other quite significantly even for the same tumor type; these differences can be attributed to great genetic variation among cancers and even within the same tumor after clonal expansion. However, in head and

neck cancer it has been noticed that HPV infection generally correlates with greater radiation sensitivity.

Investigation of elemental differences between tissues from HPV+ and HPV- head and neck cancers may, if any differences are found to be consistent, reflect HPV status and/or radiosensitivity/radioresistance of these cancers. We decided to explore the elemental makeup of head and neck cancers with this idea in mind. Nevertheless, such XFM investigation of head and neck cancers should be accompanied by complete information about HPV status, and also be supplemented with (i) studies of other tumors with different radiation sensitivity status but without HPV involvement, and (ii) studies of other tumors with viral involvement but without changes in radiation sensitivity. If we manage to correlate elemental content or distribution pattern either with HPV status or with radiation sensitivity, we could develop elemental imaging into a new tool to predict treatment outcomes. This would allow further "personalization" of radiation treatments to impact cancer care and quality of life for millions of people.

5.6 Results

Patient head and neck cancer samples at our disposal were previously tested by immunohistochemistry for expression of p16 protein. While correlation between HPV+ status and p16 + status is high, their coincidence is not absolute. Therefore, we developed protocols to test these samples for presence of high risk (HR) HPV by *in situ* DNA hybridization (ISH). Tissue samples from 34 patients were organized into tissue microarrays (TMAs), and these TMAs were used for ISH. HPV positive status was demonstrated by development of blue color indicating successful hybridization of high risk HPV DNA probe (Figure 5.1). HPV negative

samples showed no change of color; positive and negative controls suggested by the probe and kit manufacturer were used at the same time.

Patient samples were imaged by X-ray fluorescence microscopy (Figures 5.2 and 5.3). Two examples of fine scans of a pair of samples – one from an HPV- and one from an HPV+ head and neck cancer are presented. In each case both tumor and surrounding normal tissue were imaged. In the HPV- tissue sample there was no discernable differences in elemental composition between tumor and non-tumor tissue (Figure 5.3). In the HPV+ tissue sample, on the contrary (Figure 5.2), concentration of Zn in cells was higher in area corresponding to tumor than in adjacent non-tumor cells. Finally, the overall Zn signal in HPV- sample is much reduced in comparison with HPV+ sample. However, in HPV- sample Phosphorus (P) (highest in cell nuclei, Figure 5.3) correlates well with “patches” of tumor tissue (red arrow).

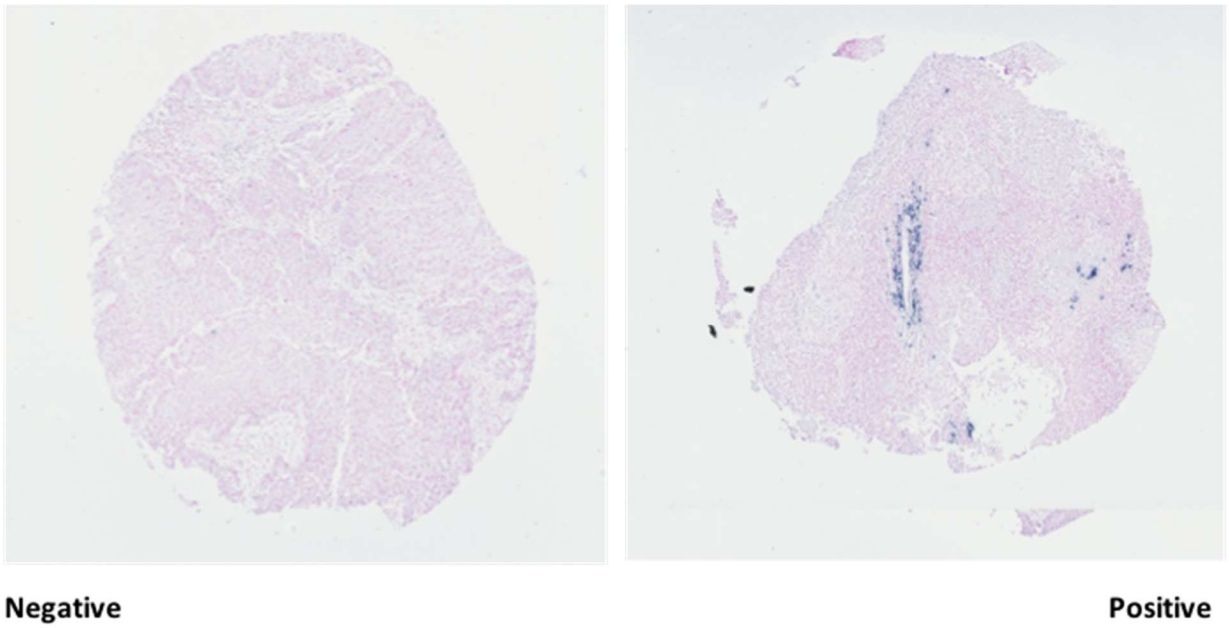

Figure 5.1. *In situ* hybridization staining of HPV DNA. Two tissue "dots" from a head and neck cancer tissue microarray are shown, as examples of representative *in situ* hybridization results for HPV- (left) and HPV+ (right) tissues. Dark blue nuclei in HPV+ sample correspond to cells containing HPV DNA from high risk HPV virus types.

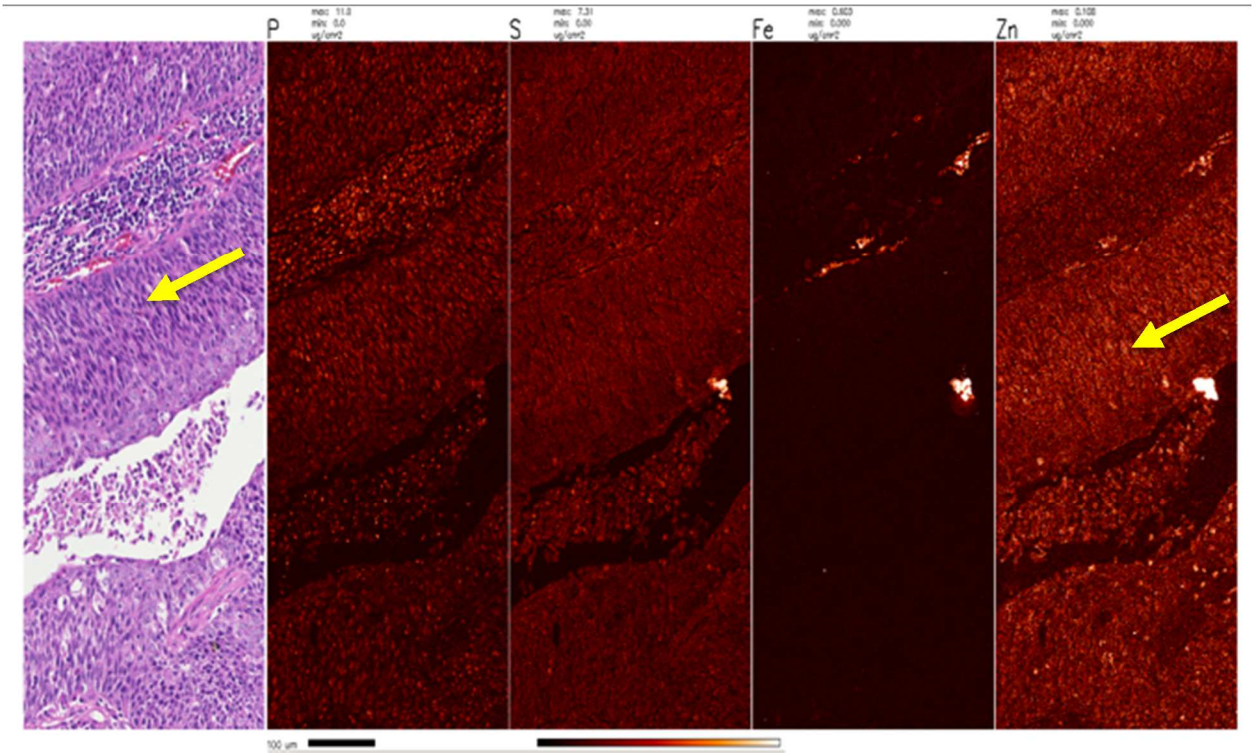

Figure 5.2. XFM image of HPV+ head and neck cancer tissue. The leftmost image is an optical micrograph of H&E stained tumor tissue with tumor spread indicated by medium purple area of the slide (arrow). X-ray fluorescence microscopy of the same sample was done and elemental maps for P, S, Fe and Zn are shown as labeled; scale bar is 200 microns; color range black (lowest signal) to white (brightest signal). Tumor area from H and E image (arrow) shows that the matching elemental map area (arrow) is a region with highest Zn signal**.**

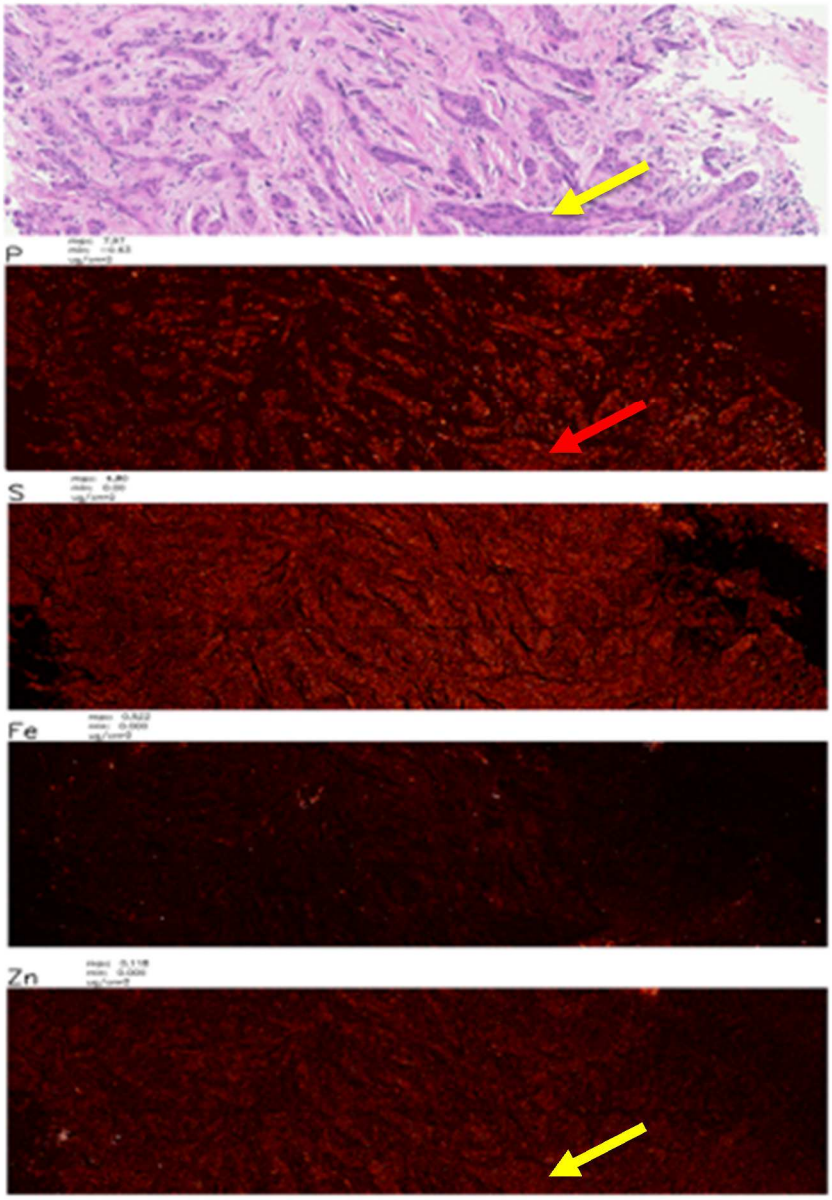

Figure 5.3. XFM image of HPV- head and neck cancer tissue. HPV- (p16-) case: topmost image is an optical micrograph with tumor spread in patient sample stained by H and E (medium purple areas of the slide, arrow). X-ray fluorescence microscopy of the same sample (elemental maps for P, S, Fe and Zn. As above, elemental maps for P, S, Fe and Zn) are shown as labeled; scale bar 200 microns; color range black (lowest signal) to white (brightest signal). Tumor area from H and E image (yellow arrow) and the matching area of elemental map for Zn show no increase of Zn signal (yellow arrow), while P is increased (red arrow).

5.7 Conclusions

Elemental concentrations in cancer cells vary significantly between different patient cases, even for the same cancer type, with Zn often playing contradictory roles in cells. The role of viral infections in elemental perturbations is not established, although their role in cancer development and response to radiation therapy are becoming more understood.

We have attempted to investigate changes in elemental composition due to viral infections. Since HPV proteins E6 and E7 are Zn binding proteins and because cancer development in HPV+ patients depends on activity of these proteins, it is probable that that may explain the increased Zn concentration in HPV+ cases we observed in our XFM analysis. It may be advantageous for HPV+ HNC to have higher Zn concentration as zinc acquisition has been shown to be important for cancer [194] although one study presenting bulk evaluation of head and neck tissues from HPV- cases suggested that pre-tumor biopsies had less Zn than their counterparts [75]. Specifically, Zn levels affect cellular health and this element has numerous and sometimes contradictory roles in cancer initiation, progression, termination, and potentially prevention. Zn is involved in cell growth and division, protein structure, enzymatic activity, and regulatory functions [195]. The presence of zinc in a number of biological processes lends itself to the idea that changes in zinc status may play a significant role in cellular dysfunction, including the development and/or progression of cancer. Evidence in support of this idea is extensive. Zinc is essential for cell proliferation [196, 197], and is important for tumor growth [198, 199], as the absence of zinc leads to cell cycle arrest [196]. Zinc is important to rapidly dividing cancer cells. Other studies have shown that zinc is necessary for both RNA and DNA stability through its interactions with Zn binding proteins [200, 201]. Cancer cells develop

mechanisms to shut down zinc efflux and maintain intracellular concentrations when availability is reduced [202].

It is interesting to note that Zn is increased in HPV+ HNC tissue but not in HPV- HNC [75]. The latter is in agreement with many other cancer types. Malignancies in liver, gallbladder, prostate, lung, cervix tissue, as well as uterine myeloma are associated with a decrease in tissue zinc concentrations compared to non-cancerous tissues [203-210]. Conversely, in breast cancer patients there has been an increase in zinc tissue concentration in comparison with normal tissues [211, 212]. Additionally, not only do normal and malignant tissue types differ in zinc concentration, but cancerous breast cells tend to accumulate more zinc than immediately adjacent non-cancerous breast cells [213].

It is interesting to consider that concentrations of Zn possibly due to HPV infection in tissue may play a role in radiation sensitivity. For instance, it has been suggested that zinc deficiency may elevate levels of free radicals and an overall state of increased oxidative stress [214]. In prostate cancer, the addition of zinc has been associated with sensitization to cytotoxic agents [215]. Zinc has been implicated in mediating apoptotic cell death [216]. Both indirect and direct apoptotic effects of zinc have been demonstrated in cancerous cells. Evidence suggests that zinc induces cell growth arrest at G2/M in a dose dependent manner [217]. This indirect effect of zinc has been attributed to the role of this element in inducing the expression of p21, a cyclin-dependent kinase inhibitor known to govern cell progression at this phase [217]. Moreover, zinc may have a more direct effect on cell death [218].

Trace elements play an important role in diseases caused by viruses as some trace elements have been shown to exhibit antiviral activity or enhance the severity of viral infections.

For example, some trace elements have been shown to inhibit virus replication in the host cells, while others may enhance their virulence [219]. Therefore, it is a safe assumption that viruses have evolved mechanisms to modulate trace elemental concentration during the course of infection.

Specifically, trace elements have been shown to bind to proteins that serve essential functions for a virus [220, 221]. For example, HPV E6 and E7 proteins have Cys-X-X-Cys repeats that have a high-affinity for binding zinc [222]. The E6 protein of human papillomavirus 16 (HPV 16) has two putative zinc ion binding sites crucial for its function [223]. Although Zn is also a critical structural component of p53 in the case of HPV infection it may assist HPV in degradation of p53 [224].

Research investigating trace metals in head and neck cancer, in particular, is limited and research examining trace metal concentration and distribution in viral associated cancer is rare. One of the few studies by Abnet et al examined an association between Zn and esophageal cancer [75]. This team conducted a prospective case control study to investigate the association between long term incidence of esophageal cell carcinoma and element concentration in tissue sections from patients participating in a nutritional intervention. X-ray fluorescence spectroscopy was used to measure zinc, copper, iron, nickel and sulfur concentrations from biopsy specimens. Patients were followed for 16 years and the incidence of esophageal cancer was tracked and recorded. High concentration of zinc was significantly associated with reduced risk of developing esophageal squamous cell carcinoma suggesting that zinc deficiency contributes to the development of esophageal squamous cell carcinoma [75]. This study was the first study showing that X-ray fluorescence spectroscopy can be used to assess relationships between

elements and disease risk. While the work demonstrated a strong negative correlation between Zn and esophageal cancer it focused more on risk rather than elemental concentrations in already developed leaving this area open for investigation. Importantly – this study did not include investigation of HPV status, and based on the cohort selected for this study it most likely that the patients were HPV-.

HPV status and viral subtype can significantly affect cancer prognosis and treatment, and HPV status has now been established as a reliable prognostic biomarker for HNC [225]. Very often HPV+ HNCs are also p16-positive (p16+) [226]. p16 is used as an immunohistochemical (IHC) stain and is a surrogate marker for HPV. This is the case so often that most clinical practitioners use p16 IHC status as an indicator of prognosis in HNC and assume the p16+ cancers are identical to HPV+ HNC. It may be, however, that HPV+ HNC cases that are p16- have especially bad prognosis [227].

The debate regarding the preferred method of detecting HPV infection is still ongoing as guidelines for HPV detection have not been clearly defined, and methods for determining HPV status often vary between studies [228]. HPV detection by polymerase chain reaction (PCR) amplification of viral RNA from fresh or frozen tissues is widely accepted as the gold-standard method for determining HPV status [229]. HPV presence is detectable indirectly through the feedback loop that induces expression of the protein (p16) through IHC. Finally, HPV viruses can also be detected by their DNA through *in situ* hybridization (ISH) [230]. Though all three methods are able to detect HPV positive tissues, p16 IHC is more sensitive than HPV16 ISH, and it is technically easier to perform than HPV16 E6 mRNA quantification by quantitative real time polymerase chain reaction (qRT-PCR) [175]. It is also arguable that it may be the expression of

p16 that is making these cancers susceptible to radiation – the most important question from the perspective of patient prognosis. Finally, fluorescence *in situ* hybridization (FISH) detects HPV DNA with high specificity but relatively low sensitivity of 85–88% [231].

While investigation of relative merits of p16 and HPV status for patient prognosis is ongoing-we propose to add evaluation of elemental content in HNC to the list in prognostic factors. Advancements in elemental tissue imaging in recent years became possible because of XFM. Today, XFM can be used to image large (cm size) sections of tissue samples with resolution in tens of microns, and then the same samples can be reduced in size, shifted to a new instrument and imaged at sub-micron resolution. We have used this approach to obtain coarse (low resolution) and fine elemental maps of different head and neck cancer samples. We hope that this study may lead the way toward more extensive use of XFM in HNC prognosis.

CHAPTER 6: Discussion

6.1 Summary and Conclusions

XFM was used in this work for two different purposes – to investigate nanoparticle treated samples and to evaluate elemental differences between HPV+ and HPV- head and neck cancers. It is important to mention that in the course of these studies we accumulated data that could also be used to investigate if and how cell stress may induce cellular elemental changes. Both nanoparticles and viruses turn on cellular stress and it is not impossible that if this study could be expanded to include hundreds of samples we could make conclusions about stress induced elemental changes in general.

Different techniques to evaluate elemental content in nanoparticle treated cells were used in this work: ICP-MS for bulk nanoparticle sample analysis and XFM for precise elemental mapping of cell samples in 2D. In addition, two new nanoparticle staining approaches for immunocytochemistry (ICC) were developed in order to enable complementary nanoparticle imaging by optical microscopy. Human patient samples from head and neck cancer, on the other hand, were investigated for HPV presence by ISH and elemental content of such samples explored by XFM. This work documents how a concerted effort to evaluate elemental content of biological samples and image the distribution of specific biological molecules in the same samples provides not only cross-validation of these imaging techniques but a new depth of understanding in biology: elemental content and biomolecule content of single cells and tissue samples depend on each other.

TiO_2 nanoparticles have unique physical properties; when activated by photons of high energy (UV light or ionizing radiation) they release ROS and cause DNA damage in the form of double stranded DNA breaks. Therefore, TiO_2 nanoparticles could be useful radiosensitizers and

increase sensitivity to radiation therapy. Targeting these nanoparticles to different subcellular locations could still increase the benefits from nanoparticle caused radiosensitization, however these studies are limited by the need to image and verify subcellular targeting of nanoparticles in large numbers of cells. Previous techniques to label and detect TiO_2 nanoparticles relied on light imaging with co-confirmation of a Ti signal with XFM. These techniques have been suboptimal. Therefore, we developed three *in situ* labeling and detection techniques. Initially, we exploited the free hydroxyl groups on TiO_2 to conjugate a fluorescein-biotin molecule and then used the high affinity of streptavidin and biotin to use Streptavidin-Cy3 as secondary detection step. We found that Streptavidin-Cy3 can detect fluorescein-biotin coated TiO_2 nanoparticles. This labeling and detection technique was successful. There was sufficient retention of fluorescein-biotin on NPs after cellular treatment. However, this approach for TiO_2 nanoparticle labeling and detection is sensitive but not very selective as we observed weak overlap between fluorescein-biotin and streptavidin-Cy3 when NPs were detected *in situ* with streptavidin-Cy3. Because of the lack of selectivity XFM was still necessary to detect and confirm NP's location. We assumed that the lack of selectivity (by way of weak overlap between fluorescein (green) and streptavidin-Cy3 (red) was due to weak OH bonds between TiO_2 and fluorescein, therefore we developed a dopamine-biotin label and streptavidin-Alexa 488 detection system. Dopamine conjugates to TiO_2 through two hydroxyl bonds rather than one making the bond stronger and there is less potential for detachment once inside of cells. Once again, we exploited the high affinity bond between biotin and streptavidin and used Streptavidin-Alexa 488 as the detection molecule. While streptavidin-Alexa 488 can detect dopamine-biotin labeled TiO_2 nanoparticles, this technique was too sensitive and again not selective enough because the background levels of

biotin in cells without nanoparticles were too high to differentiate between the background and TiO_2 nanoparticles and TiO_2 aggregates.

Finally, we modified the well-known CLICK chemistry labeling and detection system to label TiO_2 nanoparticles with azide and used fluorescently labeled alkyne-Alexa 488 to detect TiO_2 nanoparticles and nanoparticle aggregates. This labeling and detection technique was successful in that we were able to detect TiO_2 nanoparticles using a single-step labeling and detection; this was unlike the Streptavidin-Cy3 secondary labeling and both faster and more selective. The absence of cellular azide moieties led to low background compared to the dopamine-biotin and streptavidin-Alexa 488 labeling and detection. CLICK system was both selective and sensitive as only TiO_2 nanoparticles and nanoparticle aggregates fluoresced. The fluorescent signal co-registered with the Ti signal as confirmed through XFM. Moreover, even in ICC we noted that when nanoparticle and detection molecule concentrations increased so did the fluorescent signal and intensity ratio (fluorescent signal divided by the cell area). While the success of CLICK chemistry labeling and detection system satisfied our objectives, this labeling comes with some caveats. This includes the introduction of a high amount of copper into cells since the reaction is copper-catalyzed. CLICK chemistry may interfere with the ability to stain other cellular components, such as the cytoskeleton so it may not be suitable for certain combination research experiments. In addition, because the reaction involved possibly toxic levels of copper it cannot be used for live cell imaging. Nevertheless, CLICK chemistry can be used to image TiO_2 nanoparticles in fixed cells without the need to confirm NP location with XFM imaging.

Nanoparticles cause cellular stress that leads to cell death and increased sensitivity to radiation therapy; nanoparticle induced cellular stress and radiation in synergy lead to increased cell death. Similarly, HPV causes cellular stress through several mechanisms including inactivation of tumor suppressors p53 and Rb. While removal of these tumor suppressor proteins makes HPV+ cells susceptible to cancer development, activation of these same pathways leads to a feedback loop that increases production of a different tumor suppressor protein p16. It is most likely the presence of p16 that makes HPV+ cancers sensitive to radiation therapy. This example of collateral benefits of cellular stress is worth deeper examination. We compared the elemental composition of HPV+ HNC tissue and HPV- HNC tissue using XFM to begin to investigate possible elemental causes that may lead to differences in radiation responses of cancer tissues. Through XFM, we observed a unique phenotype in HPV+ HNC tissue where Zn concentration was greater compared to HPV- HNC tissue. It is still unclear if Zn increase is a product of accumulation of virally induced Zn binding proteins or if it is associated with other cellular proteins induced by cell stress (with or without a role in radiation sensitivity).

6.2 Future Directions

In conclusion, we have shown that it is possible to specifically and selectively label and detect TIO_2 in such way that XFM elemental confirmation and co-registration is not needed to verify nanoparticle location, internalization, and targeting. The future directions that will build upon this technique include (1) detecting label-free nanoparticles by treating cells with azide free nanoparticles and labeling them with dopamine-azide and then conducting the CLICK reaction and detecting nanoparticles *in situ*; (2) introducing the detection molecule *in vitro* outside of

cells, removing copper e.g. by dialysis and then treating cells with Alexa-labeled nanoparticles that have been introduced to the detection molecule prior to cellular treatment is also a possible next step; (3) since CLICK chemistry was successful in cells, it would be logical to now test the same technique in tissues; (4) for research projects where changes in Cu levels are monitored, a Cu free CLICK chemistry labeling and detecting system is needed.

Our work on HPV+ and HPV- HNC tissues demonstrates the need to continue to scan additional tissue samples and statistically analyze the differences in Zn concentration we observed in a collection of samples that is large enough to allow statistical analysis. In addition, we propose cross to correlate Zn rich regions with accumulation of E6 and E7 HPV proteins using laser capture microscopy and protein mass spectroscopy. Such a study would provide additional information regarding Zn concentration and the direct or indirect involvement of HPV in increasing the levels of Zn in HPV+ HNC tissue.

CHAPTER 7: Materials and Methods

7.1 Nanoparticle synthesis

TiO_2 nanoparticles were synthesized by applying a low-temperature alkaline hydrolysis approach according to Abbas and others [32], dialyzed in water at 4 °C, and stored at 4 °C.

7.2 Synthesis of fluorescein-biotin Nanoparticle Coating

TiO_2 nanoparticles with an average diameter of 6nm were synthesized by a low-temperature alkaline hydrolysis route as described previously and were dialyzed and stored at 4 °C in 10 mM Na_2HPO_4 buffer at pH 5.7. The molar ratio of fluorescein (FITC)-biotin (5(6)-(Biotinamidohexanoylamido-pentylthioureidylfluorescein; B8889, Sigma-Aldrich) to TiO_2 nanoparticles was such that 30% of the nanoparticle surface was covered by FITC-biotin. Binding was performed over a period of 16h in the presence of 1M glucose. Addition of glucose was performed in order to coat the nanoparticle surface and aid the uptake of nanoparticles. This degree of surface coverage of nanoparticles was used to ensure that all of the FITC-biotin molecules attached to the nanoparticle surface.

7.3 Synthesis of Azide Surface Coating

The SQ Peptide Synthesis Core facility of Northwestern University prepared for us a 95% pure dopamine-PEG_4-azide molecule; synthesis was performed using an NHS ester group on azido-PEG_4-NHS (Click Chemistry Tools) and amino group of dopamine (Sigma-Aldrich). This molecule was used to coat the surface of TiO_2 nanoparticles prior to cell treatment. The ratio of estimated TiO_2 nanoparticle surface sites and dopamine was 1:1. Upon mixing, the clear

and colorless nanoparticle solution changed to a clear and light brown solution, similar to the color change induced by dopamine binding alone, which occurs immediately upon mixing and conjugation of dopamine to nanoparticles [4]. Nanoparticles were dialyzed in 100 mM sodium phosphate buffer in dialysis tubing with 2 kDa pores. This ensured that the unbound dopamine-azide molecules (<0.5 kDa) were removed from the nanoparticle solution prior to use in cells.

7.4 Synthesis of dopamine-biotin Nanoparticle Coating

Nanoparticles used in this work were produced according to the procedure published by Abbas and others [32]. $TiCl_4$ solution was cooled to -20°C and added slowly dropwise and under vigorous steering to 40x volume of deionized water cooled to 1°C. Work was done in a chemical hood to enable removal of HCl gas that forms in this reaction. After steering overnight TiO_2 colloid was dialyzed in water at 1°C over a period of several days; this resulted in production of nanoparticles of 5nm on average (see e.g. Figure 1.2).

7.5 Nanoparticle characterization

Cryo-TEM: Bare TiO_2 nanoparticles and azide-coated nanoparticles were diluted 1:50, plunge frozen in liquid ethane, and imaged using a transmission electron microscope (TEM) in the Biological Imaging Facility (BIF) at Northwestern University. The average size of NPs was found to be 5 nm ±2.9 nm (Figure 3.2).

Dynamic Light Scattering: Bare TiO_2 nanoparticles and azide-coated nanoparticles were diluted 1:100 or 1:200 in dH_2O and assayed for hydrodynamic diameter size using Malvern capillary cells on the Zetasizer Nano ZSP in the Northwestern University Analytical BioNanoTechnology Equipment Core (ANTEC) facility.

Zeta Potential: Bare TiO_2 nanoparticles and azide-coated nanoparticles were diluted 1:100 or 1:200 in dH_20 and assayed for zeta potentials using Malvern capillary cells on the Zetasizer Nano ZSP in the Northwestern University ANTEC facility.

7.6 Calculating NP concentrations

The concentration of TiO_2 NPs in solution was measured at the Northwestern University Quantitative Bioelemental Imaging Center on a X Series II Inductively Coupled Plasma-Mass Spectrometer (Thermo Scientific, West Palm Beach, FL) and compared to seven standards ranging from 0 ppb to 50 ppb titanium or iron with 3 ppb indium internal controls included in all samples and standards. Calculation of NP molarity based on ICP-MS and Cryo-TEM sizing data was done as outlined below:

Assumptions:

1. Perfectly spherical NPs with a total volume ($V_T = V_{TiO2} + V_{Fe}$)
2. All Ti atoms are bonded with oxygen as TiO_2, therefore the mole ratio of Ti to TiO_2 is 1:1

Method:

1. Calculate volume of TiO_2:

$$\frac{4}{3} \times \pi \times \left(\frac{D_T}{2}\right)^3 = V_{TiO2}$$

$$\frac{4}{3} \times \pi \times \left(\frac{x\ nm}{2}\right)^3 = V_{TiO2}$$

2. Calculate mass of TiO_2 per particle using density of anatase TiO2 ($\rho_{ana} = 3.88\ g/cm^3$) and volume of TiO_2:

$$\frac{m_{TiO2}}{par\square icle} = \rho_{ana} \times V_{TiO2}$$

3. Calculate moles of TiO_2 per particle using molar mass of TiO2:

$$\frac{m_{TiO2}}{particle} \div \frac{79.88\ g}{mol}$$

4. Convert ICP-MS concentration from g/mL of Ti to mol/L of Ti:

$$x\frac{g}{mL} \times 1000\frac{mL}{L} \div 47.88\frac{g}{mol}$$

5. Divide the mol/L of Ti from ICP-MS by mol/particle of Ti from step 3 to get particles/L
6. Convert particles/L to mol/L by dividing by Avogadro's number

Equation if you want to just plug in values:

$$\frac{[\boldsymbol{Ti}]_{\boldsymbol{ICP-MS}}}{\left[\frac{\boldsymbol{\rho_{ana}(V_T - V_{Fe})}}{\boldsymbol{MW_{TiO2}}}\right]\boldsymbol{N_A}} = [\boldsymbol{TiO2\ NPs}]$$

Simplified versions of the equation:

$$\frac{[Ti]_{ICP-MS}}{\left[\frac{\pi\rho_{ana}(D_T{}^3 - D_{Fe}{}^3)}{6 \times MW_{TiO2}}\right]N_A} = [TiO2\ NPs]$$

$$\frac{\boldsymbol{6 \times MW_{TiO2}}}{\boldsymbol{\pi\rho_{ana}N_A}} \times \frac{[\boldsymbol{Ti}]_{\boldsymbol{ICP-MS}}}{\boldsymbol{D_T{}^3 - D_{Fe}{}^3}} = [\boldsymbol{TiO2\ NPs}]$$

7.7 Cell culture

For Fluorescein-biotin and Streptavidin-Cy3 experiments, MCF-7 cells were maintained at 37 °C with 5% CO_2. Roswell Park Memorial Institute (RPMI) 1640 media was supplemented with 10% fetal bovine serum (FBS), 2 mM L-glutamine, 10 mM HEPES, 100 I.U. mL^{-1} penicillin, 100 μg mL^{-1} streptomycin, 1X non-essential amino acids, 0.25 μg mL^{-1} amphotericin B, and 0.1 mg mL^{-1} insulin (Sigma-Aldrich). Prior to treatment with nanoparticles, MCF-7 cells were placed in serum-free RPMI 1640 medium for 1 h. Next, the cells were treated with 0.12 μM of TiO_2 nanoparticles coated with FITC-biotin (Sigma-Aldrich) overnight. The cells were washed with phosphate-buffered saline (PBS) solution and 200 mM of acidic glycine (pH 4.0) in order to reduce surface-bound nanoparticles. The cells labeled by FITC were collected using fluorescence-activated cell sorting (FACS) by the DakoCytomation MoFlo flow cytometer (Dako) and seeded on formvar-coated gold electron microscopy grids (Electron Microscopy Sciences) to allow for cell adherence. After 3h, the cells were washed in PBS and fixed in 4% paraformaldehyde.

For CLICK Chemistry experiments, HeLa cells were obtained from the American Type Culture Collection (ATCC). The cell line was maintained at 37°C with 5% CO_2 in Dulbecco's Modified Eagle's Medium (DMEM) supplemented with 10% FBS and 1% penicillin and streptomycin. For visualization by confocal microscopy, ~50,000 HeLa cells were cultured on glass slides (BioGenex barrier slides XT134-SL) overnight. These slides were washed with 1X PBS and placed in serum-free DMEM for 1 h. About 50,000 HeLa cells were seeded per barrier slide within a surface area of 1000 mm^2. Cells were treated with dopamine-PEG_4-azide-coated TiO_2 nanoparticles diluted in serum-free DMEM. The final TiO_2 concentration was 0.2 μg mL^{-1}

or, for nanoparticles averaging 5nm in diameter, approximately 0.16nM nanoparticles. Cells and nanoparticles were incubated at 37 °C for 1h. As a control, we included cells without nanoparticles. After nanoparticle incubation, cells were washed once with cold acidic glycine (200 mM, pH 4.0) and then washed twice with PBS with calcium and magnesium. Cells were then fixed in 4% formaldehyde in 1X PBS for 10 mins.

7.8 Nanoparticle Detection with Streptavidin-Cy3

Samples were washed and treated with 25 μM of Cy3-labeled streptavidin (Sigma-Aldrich) for 1h. At the same time, nuclear DNA was stained by Hoechst 33342 (Invitrogen). Finally, the cells were washed and imaged on the LSM 510 UV Meta Microscope (Carl Zeiss Inc.) using lasers of 405, 488, and 543 nm to excite Hoechst, FITC, and Cy3, respectively. Bandpass filters of 420–480, 475–525, and 530–600 nm were used in conjunction with the appropriate excitation lasers. After visualization of the samples with fluorescence microscopy, the position of the cells was noted, and the samples were further prepared for XFM analysis. Position of the cells was noted, and the samples were further prepared for XFM analysis.

7.9 Nanoparticle Detection with CLICK Chemistry

The CLICK chemistry reaction was adapted from the manufacturer's protocol provided for labeling of azide-conjugated proteins. Following fixation, cells were washed three times for 3 min each with 1X PBS and permeabilized with 0.5% triton-X in PBS for 10 min at room temperature. Then, cells were rinsed three times for 3 min each with 1X PBS and blocked with

2% bovine serum albumin (BSA) in 1X PBS for 20 min at room temperature. A cocktail of the CLICK reagents (Life Technologies CLICK chemistry kit C10269) was prepared in the following proportions: 30 μL of 100 mM $CuSO_4$, 150 μL of 20 mg mL^{-1} Reactive Additive Buffer (Component C), 1,260 μL of 1X Cell Reaction Buffer, and 0.67 μM as the final concentration of alkyne-Alexa Fluor 488 (Life Technologies A10267). Cells were incubated with 300 μL of the CLICK reagent mixture per slide (1000 mm^2 surface area) for 30 min. Then, slides were washed three times for 3 min with 1X PBS, blocked for 10 min in 2% BSA, and then incubated with Hoechst 1:2500 in PBS for 10 min.

7.10 Nanoparticle Detection with Streptavidin-Alexa 488

Following fixation cells were washed 3x for 3 minutes each in 1xPBS and permeabilized in 1xPBS + 0.2% Triton X-100 for 5 minutes at room temperature. Cells were then washed 3x for 3 minutes each in 1xPBS and blocked in 1X TBST + 2% Bovine Serum Albumin (BSA) for 20 minutes at room temperature. Streptavidin-Alexa 488 was diluted 25uL/mL in 500uL 1X PBS and the mixture of Streptavidin and 1X PBS was added to cells. Cells incubated for 1hr at room temperature. Then cells were washed 3x for 3 minutes each in 1X PBS and blocked in 1X TBST + 2% BSA for 20 mins at room temperature. Cells were washed 1x for 3 min in 1X PBS and stained with diluted Hoechst at 1:2500 in 1xPBS. Cell ere then incubated at room temperature for 10 minutes and excess liquid off was drained off of slides**.** Slides were mounted cover slips and a drop of prolong gold anti-fade reagent and seal with clear nail polish.

7.11 Confocal Microscopy Imaging of Nanoparticles and Image Analysis

MCF-7 cells treated first with TiO_2 nanoparticles coated with FITC-biotin were washed, fixed in 4% paraformaldehyde, and then treated with 25 μM of Cy3-labeled streptavidin (Streptavidin−Cy3™ from *Streptomyces avidinii*, Sigma-Aldrich) for 1 h. At the same time, nuclear DNA was stained by Hoechst 33342 (Invitrogen). The samples were imaged on the LSM 510 UV Meta Microscope (Carl Zeiss Inc.). To allow visualization of cell nuclei by Hoechst staining, FITC, and Cy3, lasers of 405, 488, and 543 nm were used. The detection of Hoechst, FITC, and Cy3 emissions were facilitated by bandpass filters of 420–480, 475–525, and 530–600 nm, respectively. After visualization of the samples with fluorescence microscopy, the position of the cells was noted, and the samples were further prepared for XFM analysis.

After CLICK labeling and Hoechst staining of nuclear DNA, slides with azide-dopamine nanoparticle-treated HeLa cells were washed three times for 3 min in PBS, drained of excess PBS, and covered with anti-fade mounting medium (Prolong Gold; Life Technologies); glass coverslips were applied and sealed with clear nail polish. Cells were visualized using the Nikon A1R Confocal Microscope at the Northwestern University Center for Advanced Microscopy using 405-nm and 488-nm lasers with bandpass filters of 420–480 nm and 505–530 nm, respectively. In addition, Z stack slices were taken every 0.22 μm. Identical microscope settings were used for all comparison images (e.g., Fig. 3.8). Nikon Elements Software was used to analyze fluorescence intensity signals and signal areas (Table 3.2).

7.12 X-Ray Fluorescence Microscopy (XFM)

Imaging of cells by XFM at room temperature requires that they are prepared on suitable substrate and imaged only after they have been completely dried. Therefore, all confocal imaging had to be performed prior to XFM. We used two X-ray imaging instruments at the Advanced Photon Source (APS) Synchrotron at Argonne National Laboratory (ANL). One of them (X-ray microprobe) is located at the 2-ID-D beamline, while the other (Bionanoprobe) resides at the LS-CAT beamline. Monochromatic hard X-rays (~10 keV) were used at 2-ID-D; fluorescent X-ray emission was detected by a germanium detector (LEGe Detector, Canberra). The cells were raster scanned with a step size of 500 nm and dwell time of 2 sec per step (Figs. 1 and 2). These data were fitted against elemental NBS standards 1832 and 1833 using MAPS software [27]. Elemental quantification and elemental 2D maps were calculated using the MAPS program [232]. At the Bionanoprobe instrument, monochromatic 10 keV hard X-rays were used as well. However, they were focused to a spot size of ~85 nm using Fresnel zone plates. The fluorescence spectra at each scan step was collected with a four-element silicon drift detector (Vortex ME-4, SII Nanotechnology). Data were fitted and quantified by comparison to a standard reference material (RF8-200-S2453, AXO Dresden GmbH) using the MAPS program [232].

7.13 High Risk HPV DNA *in situ* Hybridization

To cross compare p16 expression with HPV status we explored the use of HPV high risk *in situ* hybridization as a method to detect HPV DNA. We developed the HPV high risk *in situ* hybridization protocol in our laboratory using the Zyto*Fast* PLUS CISH Implementation Kit (Zytovision T-1061-40). We obtained tissue microarrays from tumor tissues collected from 34

patients who presented with head and neck cancer at Northwestern University Department of Radiation Oncology. Each patient's tumor tissue was previously evaluated for p16 presence through p16 immunohistochemistry (data not shown). After p16 status was determined, paraffin blocks of patient head and neck tissue was used to make tissue microarrays. Tissue microarrays were de-paraffinized at 70 ºC for 10 minutes, soaked in xylene for 5 minutes two times and 100% ethanol for 1 minute three times and air dried at room temperature for 10 minutes. Then we added 3 drops of Pepsin Solution to slides and incubated slides for 20 minutes at 37 ºC. After incubation, slides were soaked in a covered staining jar of 95 ºC EDTA solution for 15 minutes. Afterwards, slides were dipped in dH_2O and excess water was drained off. Slides were dried until they were slightly dry but not completely dry. Then we applied 15uL of digoxigenin-labeled HPV high risk DNA probe in hybridization solution to each slide, covered the solution with a coverslip and sealed the coverslip with rubber cement. Slides were then placed on a 75 ºC heating block for 5 minutes then incubated at 37 ºC overnight. Following overnight probe hybridization, coverslips were removed and slides were washed in 1X TBS wash buffer at 55 ºC for 5 minutes. Next slides were washed in 1X TBS wash buffer at room temperature for 1 minute. We then applied 2 drops of Rabbit-Anti-DIG to slides and incubated slides at 37 ºC for 30 minutes and washed slides in 1X TBS wash buffer at room temperature for 1min three times. Then we applied 2 drops of Anti-Rabbit-AP-Polymer to slides and incubated slides at 37 ºC for 30 minutes and washed slides in 1X TBS wash buffer at room temperature for 1min three times. Next, we applied 2 drops of NBT/BCIP solution to slides and incubated slides at 37 ºC for 40 minutes and then washed slides in dH_20 for 2 minutes three times. We then added Nuclear Red Counterstain to slides and incubated for 2-5 minutes and washed slides in dH_2O for 1 minute.

Slides were then dehydrated in 70% ethanol, 85% ethanol, 95% ethanol, and 100% ethanol two times for 2 minutes each. Then slides were cleared in xylene for 2 minutes two times and air dried for 15 minutes. Finally, we added 1-4 drops of mounting solution and covered each slide with a coverslip and sealed. Slides of tumor microarrays were then imaged on Nanozoomer and blue staining confirmed HPV status. Imaged microarrays were then compared to previously attained p16 IHC data.

7.14 HPV HNC XFM Scanning

In preparation for XFM, HNC tissue samples were thin sectioned and placed on Ultralene membrane on "tissue sample holders" suitable for high throughput XFM imaging at the APS beamline 8BMB. XFM of these tissue samples was conducted in the same manner as single cell XFM, using fly scans, this time with 30 micron step size (low resolution imaging). Data was analyzed as before – elemental quantification was done using MAPS software and areas corresponding to tumor and stroma identified by a pathologist. Subsections of these tissue samples were extracted and re-mounted on sample holders suitable for higher resolution XFM imaging at 2IDE microprobe. After fly scans and elemental quantification detailed tissue features could be seen, with maps of different elements replicating cell and tissue features (e.g. see Figures 5.2 and 5.3).

REFERENCES

1. Dimitrijevic, N.M., Z.V. Saponjic, B.M. Rabatic, and T. Rajh, *Assembly and charge transfer in hybrid TiO(2) architectures using biotin-avidin as a connector.* J Am Chem Soc, 2005. **127**(5): p. 1344-1345.
2. Liu, J.Q., L. de la Garza, L.G. Zhang, N.M. Dimitrijevic, X.B. Zuo, D.M. Tiede, and T. Rajh, *Photocatalytic probing of DNA sequence by using TiO2/dopamine-DNA triads.* Chemical Physics, 2007. **339**(1-3): p. 154-163.
3. Paunesku, T., T. Rajh, G. Wiederrecht, J. Maser, S. Vogt, N. Stojicevic, M. Protic, B. Lai, J. Oryhon, M. Thurnauer, and G. Woloschak, *Biology of TiO2-oligonucleotide nanocomposites.* Nat Mater, 2003. **2**(5): p. 343-346.
4. Rajh, T., L.X. Chen, K. Lukas, T. Liu, M.C. Thurnauer, and D.M. Tiede, *Surface restructuring of nanoparticles: An efficient route for ligand-metal oxide crosstalk.* Journal of Physical Chemistry B, 2002. **106**(41): p. 10543-10552.
5. Urdaneta, I., A. Keller, O. Atabek, J.L. Palma, D. Finkelstein-Shapiro, P. Tarakeshwar, V. Mujica, and M. Calatayud, *Dopamine Adsorption on TiO2 Anatase Surfaces.* Journal of Physical Chemistry C, 2014. **118**(35): p. 20688-20693.
6. Vega-Arroyo, M., P.R. LeBreton, T. Rajh, P. Zapol, and L.A. Curtiss, *Density functional study of the TiO2-dopamine complex.* Chemical Physics Letters, 2005. **406**(4-6): p. 306-311.
7. Endres, P.J., T. Paunesku, S. Vogt, T.J. Meade, and G.E. Woloschak, *DNA-TiO2 nanoconjugates labeled with magnetic resonance contrast agents.* J Am Chem Soc, 2007. **129**(51): p. 15760-15761.
8. Thurn, K.T., T. Paunesku, A. Wu, E.M. Brown, B. Lai, S. Vogt, J. Maser, M. Aslam, V. Dravid, R. Bergan, and G.E. Woloschak, *Labeling TiO2 nanoparticles with dyes for optical fluorescence microscopy and determination of TiO2-DNA nanoconjugate stability.* Small, 2009. **5**(11): p. 1318-1325.
9. Ye, L., R. Pelton, and M.A. Brook, *Biotinylation of TiO(2) nanoparticles and their conjugation with streptavidin.* Langmuir, 2007. **23**(10): p. 5630-5637.
10. Thurn, K.T., E. Brown, A. Wu, S. Vogt, B. Lai, J. Maser, T. Paunesku, and G.E. Woloschak, *Nanoparticles for applications in cellular imaging.* Nanoscale Res Lett, 2007. **2**(9): p. 430-441.
11. Wu, A., T. Paunesku, Z. Zhang, S. Vogt, B. Lai, J. Maser, V. Yaghmai, D. Li, R.A. Omary, and G.E. Woloschak, *A Multimodal Nanocomposite for Biomedical Imaging.* AIP Conf Proc, 2011. **1365**: p. 379.
12. Arora, H.C., M.P. Jensen, Y. Yuan, A. Wu, S. Vogt, T. Paunesku, and G.E. Woloschak, *Nanocarriers enhance Doxorubicin uptake in drug-resistant ovarian cancer cells.* Cancer Res, 2012. **72**(3): p. 769-778.
13. Bazak, R., J. Ressl, S. Raha, C. Doty, W. Liu, B. Wanzer, S.A. Salam, S. Elwany, T. Paunesku, and G.E. Woloschak, *Cytotoxicity and DNA cleavage with core-shell nanocomposites functionalized by a KH domain DNA binding peptide.* Nanoscale, 2013. **5**(23): p. 11394-11399.
14. Brown, E.M., T. Paunesku, A. Wu, K.T. Thurn, B. Haley, J. Clark, T. Priester, and G.E. Woloschak, *Methods for assessing DNA hybridization of peptide nucleic acid-titanium dioxide nanoconjugates.* Anal Biochem, 2008. **383**(2): p. 226-235.

15. Kurepa, J., T. Paunesku, S. Vogt, H. Arora, B.M. Rabatic, J. Lu, M.B. Wanzer, G.E. Woloschak, and J.A. Smalle, *Uptake and distribution of ultrasmall anatase TiO2 Alizarin red S nanoconjugates in Arabidopsis thaliana.* Nano Lett, 2010. **10**(7): p. 2296-2302.
16. Paunesku, T., T. Ke, R. Dharmakumar, N. Mascheri, A. Wu, B. Lai, S. Vogt, J. Maser, K. Thurn, B. Szolc-Kowalska, et al., *Gadolinium-conjugated TiO2-DNA oligonucleotide nanoconjugates show prolonged intracellular retention period and T1-weighted contrast enhancement in magnetic resonance images.* Nanomedicine, 2008. **4**(3): p. 201-207.
17. Paunesku, T., S. Vogt, B. Lai, J. Maser, N. Stojicevic, K.T. Thurn, C. Osipo, H. Liu, D. Legnini, Z. Wang, C. Lee, and G.E. Woloschak, *Intracellular distribution of TiO2-DNA oligonucleotide nanoconjugates directed to nucleolus and mitochondria indicates sequence specificity.* Nano Lett, 2007. **7**(3): p. 596-601.
18. Rajh, T., N.M. Dimitrijevic, and E.A. Rozhkova, *Titanium dioxide nanoparticles in advanced imaging and nanotherapeutics.* Methods Mol Biol, 2011. **726**: p. 63-75.
19. Thurn, K.T., H. Arora, T. Paunesku, A. Wu, E.M. Brown, C. Doty, J. Kremer, and G. Woloschak, *Endocytosis of titanium dioxide nanoparticles in prostate cancer PC-3M cells.* Nanomedicine, 2011. **7**(2): p. 123-130.
20. Yuan, Y., S. Chen, T. Paunesku, S.C. Gleber, W.C. Liu, C.B. Doty, R. Mak, J. Deng, Q. Jin, B. Lai, et al., *Epidermal growth factor receptor targeted nuclear delivery and high-resolution whole cell X-ray imaging of Fe3O4@TiO2 nanoparticles in cancer cells.* ACS Nano, 2013. **7**(12): p. 10502-10517.
21. Kotsokechagia, T., N.M. Zaki, K. Syres, P. de Leonardis, A. Thomas, F. Cellesi, and N. Tirelli, *PEGylation of Nanosubstrates (Titania) with Multifunctional Reagents: At the Crossroads between Nanoparticles and Nanocomposites.* Langmuir, 2012. **28**(31): p. 11490-11501.
22. Zhang, A.P. and Y.P. Sun, *Photocatalytic killing effect of TiO2 nanoparticles on Ls-174-t human colon carcinoma cells.* World J Gastroenterol, 2004. **10**(21): p. 3191-3193.
23. Hall, E.J., *Radiobiology for the radiologist*. 2d ed. xiii, 460 pages.
24. Roots, R. and S. Okada, *Estimation of Life Times and Diffusion Distances of Radicals Involved in X-Ray-Induced DNA Strand Breaks or Killing of Mammalian Cells.* Radiation Research, 1975. **64**(2): p. 306-320.
25. Tachikawa, T., Y. Asanoi, K. Kawai, S. Tojo, A. Sugimoto, M. Fujitsuka, and T. Majima, *Photocatalytic cleavage of single TiO2/DNA nanoconjugates.* Chemistry, 2008. **14**(5): p. 1492-1498.
26. Wamer, W.G., J.J. Yin, and R.R. Wei, *Oxidative damage to nucleic acids photosensitized by titanium dioxide.* Free Radic Biol Med, 1997. **23**(6): p. 851-858.
27. McMahon, S.J., H. Paganetti, and K.M. Prise, *Optimising element choice for nanoparticle radiosensitisers.* Nanoscale, 2016. **8**(1): p. 581-589.
28. Fujishima, A. and K. Honda, *Electrochemical photolysis of water at a semiconductor electrode.* Nature, 1972. **238**(5358): p. 37-38.
29. Dimitrijevic, N.M., E. Rozhkova, and T. Rajh, *Dynamics of localized charges in dopamine-modified TiO(2) and their effect on the formation of reactive oxygen species.* J Am Chem Soc, 2009. **131**(8): p. 2893-2899.

30. Monopoli, M.P., C. Aberg, A. Salvati, and K.A. Dawson, *Biomolecular coronas provide the biological identity of nanosized materials.* Nat Nano, 2012. **7**(12): p. 779-786.
31. Paunesku, T., S. Gutiontov, K. Brown, and G.E. Woloschak, *Radiosensitization and nanoparticles.* Cancer Treat Res, 2015. **166**: p. 151-171.
32. Abbas, Z., J.P. Holmberg, A.K. Hellstrom, M. Hagstrom, J. Bergenholtz, M. Hassellov, and E. Ahlberg, *Synthesis, characterization and particle size distribution of TiO2 colloidal nanoparticles.* Colloids and Surfaces a-Physicochemical and Engineering Aspects, 2011. **384**(1-3): p. 254-261.
33. Brown, K., T. Thurn, L. Xin, W. Liu, R. Bazak, S. Chen, B. Lai, S. Vogt, C. Jacobsen, T. Paunesku, and G. Woloschak, *Intracellular in situ Labeling of TiO2 Nanoparticles for Fluorescence Microscopy Detection.* Nano Research, 2017. **in press**.
34. [cited 2017 October 1, 2017]; Available from: https://ncl.cancer.gov/resources/assay-cascade-protocols.
35. Kirz, J., *Mapping the distribution of particular atomic species.* Annals of the New York Academy of Sciences, 1980. **342**(1): p. 273--287.
36. Sparks, J.C.J., *X-ray fluorescence microprobe for chemical analysis.* 1980: p. 459--512.
37. Marvin, R.G., J.L. Wolford, M.J. Kidd, S. Murphy, J. Ward, E.L. Que, M.L. Mayer, J.E. Penner-Hahn, K. Haldar, and T.V. O'Halloran, *Fluxes in "free" and total zinc are essential for progression of intraerythrocytic stages of Plasmodium falciparum.* Chem Biol, 2012. **19**(6): p. 731-741.
38. Bancroft, L.W. and A. Stevens, *Theory and practice of histological techniques*. 2015/05/04 ed. 1996, New York: Churchill Livingston.
39. Petibois, C., *Imaging methods for elemental, chemical, molecular, and morphological analyses of single cells.* Anal Bioanal Chem, 2010. **397**(6): p. 2051-2065.
40. Chen, S., J. Deng, Y. Yuan, C. Flachenecker, R. Mak, B. Hornberger, Q. Jin, D. Shu, B. Lai, J. Maser, et al., *The Bionanoprobe: hard X-ray fluorescence nanoprobe with cryogenic capabilities.* J Synchrotron Radiat, 2014. **21**(Pt 1): p. 66-75.
41. Chen, S., T. Paunesku, Y. Yuan, Q. Jin, B. Hornberger, C. Flachenecker, B. Lai, K. Brister, C. Jacobsen, G. Woloschak, and S. Vogt, *The Bionanoprobe: Synchrotron-based Hard X-ray Fluorescence Microscopy for 2D/3D Trace Element Mapping.* Micros Today, 2015. **23**(3): p. 26-29.
42. Jin, Q., T. Paunesku, B. Lai, S.C. Gleber, S.I. Chen, L. Finney, D. Vine, S. Vogt, G. Woloschak, and C. Jacobsen, *Preserving elemental content in adherent mammalian cells for analysis by synchrotron-based x-ray fluorescence microscopy.* J Microsc, 2017. **265**(1): p. 81-93.
43. Finney, L.A. and Q. Jin, *Preparing adherent cells for X-ray fluorescence imaging by chemical fixation.* J Vis Exp, 2015(97).
44. Berg, J.M. and Y. Shi, *The galvanization of biology: a growing appreciation for the roles of zinc.* Science, 1996. **271**(5252): p. 1081-1085.
45. Whitaker, M., *Calcium microdomains and cell cycle control.* Cell Calcium, 2006. **40**(5-6): p. 585-592.
46. Yruela, I., *Transition metals in plant photosynthesis.* Metallomics, 2013. **5**(9): p. 1090-1109.

47. Chandra, S., D. Gross, Y.C. Ling, and G.H. Morrison, *Quantitative imaging of free and total intracellular calcium in cultured cells.* Proc Natl Acad Sci U S A, 1989. **86**(6): p. 1870-1874.
48. Wolford, J.L., Y. Chishti, Q. Jin, J. Ward, L. Chen, S. Vogt, and L. Finney, *Loss of pluripotency in human embryonic stem cells directly correlates with an increase in nuclear zinc.* PLoS One, 2010. **5**(8): p. e12308.
49. McRae, R., B. Lai, and C.J. Fahrni, *Subcellular redistribution and mitotic inheritance of transition metals in proliferating mouse fibroblast cells.* Metallomics, 2013. **5**(1): p. 52-61.
50. Finney, L., S. Vogt, T. Fukai, and D. Glesne, *Copper and angiogenesis: unravelling a relationship key to cancer progression.* Clin Exp Pharmacol Physiol, 2009. **36**(1): p. 88-94.
51. Finney, L., S. Mandava, L. Ursos, W. Zhang, D. Rodi, S. Vogt, D. Legnini, J. Maser, F. Ikpatt, O.I. Olopade, and D. Glesne, *X-ray fluorescence microscopy reveals large-scale relocalization and extracellular translocation of cellular copper during angiogenesis.* Proc Natl Acad Sci U S A, 2007. **104**(7): p. 2247-2252.
52. O'Connor, N. and R.B. Silver, *Ratio imaging: practical considerations for measuring intracellular Ca2+ and pH in living cells.* Methods Cell Biol, 2007. **81**: p. 415-433.
53. Roe, M.W., J.J. Lemasters, and B. Herman, *Assessment of Fura-2 for measurements of cytosolic free calcium.* Cell Calcium, 1990. **11**(2-3): p. 63-73.
54. Dodani, S.C., D.W. Domaille, C.I. Nam, E.W. Miller, L.A. Finney, S. Vogt, and C.J. Chang, *Calcium-dependent copper redistributions in neuronal cells revealed by a fluorescent copper sensor and X-ray fluorescence microscopy.* Proc Natl Acad Sci U S A, 2011. **108**(15): p. 5980-5985.
55. Kehr, S., M. Malinouski, L. Finney, S. Vogt, V.M. Labunskyy, M.V. Kasaikina, B.A. Carlson, Y. Zhou, D.L. Hatfield, and V.N. Gladyshev, *X-ray fluorescence microscopy reveals the role of selenium in spermatogenesis.* J Mol Biol, 2009. **389**(5): p. 808-818.
56. Ceko, M.J., K. Hummitzsch, N. Hatzirodos, R.J. Rodgers, and H.H. Harris, *Quantitative elemental analysis of bovine ovarian follicles using X-ray fluorescence imaging.* Metallomics, 2015. **7**(5): p. 828-836.
57. James, S.A., M.D. de Jonge, D.L. Howard, A.I. Bush, D. Paterson, and G. McColl, *Direct in vivo imaging of essential bioinorganics in Caenorhabditis elegans.* Metallomics, 2013. **5**(6): p. 627-635.
58. Bourassa, D., S.C. Gleber, S. Vogt, C.H. Shin, and C.J. Fahrni, *MicroXRF tomographic visualization of zinc and iron in the zebrafish embryo at the onset of the hatching period.* Metallomics, 2016. **8**(10): p. 1122-1130.
59. Bourassa, D., S.C. Gleber, S. Vogt, H. Yi, F. Will, H. Richter, C.H. Shin, and C.J. Fahrni, *3D imaging of transition metals in the zebrafish embryo by X-ray fluorescence microtomography.* Metallomics, 2014. **6**(9): p. 1648-1655.
60. Surowka, A.D., P. Wrobel, D. Adamek, E. Radwanska, and M. Szczerbowska-Boruchowska, *Synchrotron radiation based X-ray fluorescence shows changes in the elemental composition of the human substantia nigra in aged brains.* Metallomics, 2015. **7**(11): p. 1522-1531.

61. Punshon, T., S. Chen, L. Finney, L. Howard, B.P. Jackson, M.R. Karagas, and K. Ornvold, *High-resolution elemental mapping of human placental chorionic villi using synchrotron X-ray fluorescence spectroscopy.* Anal Bioanal Chem, 2015. **407**(22): p. 6839-6850.
62. Vogt, S., *MAPS: A set of software tools for analysis and visualization of 3D X-ray fluorescence data sets.* Journal De Physique Iv, 2003. **104**: p. 635-638.
63. Szczerbowska-Boruchowska, M., A. Krygowska-Wajs, and D. Adamek, *Elemental micro-imaging and quantification of human substantia nigra using synchrotron radiation based x-ray fluorescence--in relation to Parkinson's disease.* J Phys Condens Matter, 2012. **24**(24): p. 244104.
64. House, M.J., A.J. Fleming, M.D. de Jonge, D. Paterson, D.L. Howard, J.P. Carpenter, D.J. Pennell, and T.G. St Pierre, *Mapping iron in human heart tissue with synchrotron x-ray fluorescence microscopy and cardiovascular magnetic resonance.* J Cardiovasc Magn Reson, 2014. **16**: p. 80.
65. Kinoshita, H., Y. Hori, T. Fukumoto, T. Ohigashi, K. Shinohara, Y. Hayashi, and Y. Ku, *Novel assessment of hepatic iron distribution by synchrotron radiation X-ray fluorescence microscopy.* Med Mol Morphol, 2010. **43**(1): p. 19-25.
66. Bhattacharjee, A., H. Yang, M. Duffy, E. Robinson, A. Conrad-Antoville, Y.W. Lu, T. Capps, L. Braiterman, M. Wolfgang, M.P. Murphy, L. Yi, S.G. Kaler, S. Lutsenko, and M. Ralle, *The Activity of Menkes Disease Protein ATP7A Is Essential for Redox Balance in Mitochondria.* J Biol Chem, 2016. **291**(32): p. 16644-16658.
67. Kinebuchi, M., A. Matsuura, T. Kiyono, Y. Nomura, and S. Kimura, *Diagnostic copper imaging of Menkes disease by synchrotron radiation-generated X-ray fluorescence analysis.* Sci Rep, 2016. **6**: p. 33247.
68. Das, A., V. Sudhahar, G.F. Chen, H.W. Kim, S.W. Youn, L. Finney, S. Vogt, J. Yang, J. Kweon, B. Surenkhuu, M. Ushio-Fukai, and T. Fukai, *Endothelial Antioxidant-1: a Key Mediator of Copper-dependent Wound Healing in vivo.* Sci Rep, 2016. **6**: p. 33783.
69. Flinn, J.M., P. Kakalec, R. Tappero, B. Jones, and I. Lengyel, *Correlations in distribution and concentration of calcium, copper and iron with zinc in isolated extracellular deposits associated with age-related macular degeneration.* Metallomics, 2014. **6**(7): p. 1223-1228.
70. James, S.A., Q.I. Churches, M.D. de Jonge, I.E. Birchall, V. Streltsov, G. McColl, P.A. Adlard, and D.J. Hare, *Iron, Copper, and Zinc Concentration in Abeta Plaques in the APP/PS1 Mouse Model of Alzheimer's Disease Correlates with Metal Levels in the Surrounding Neuropil.* ACS Chem Neurosci, 2016.
71. Leskovjan, A.C., A. Kretlow, A. Lanzirotti, R. Barrea, S. Vogt, and L.M. Miller, *Increased brain iron coincides with early plaque formation in a mouse model of Alzheimer's disease.* Neuroimage, 2011. **55**(1): p. 32-38.
72. Miller, L.M., Q. Wang, T.P. Telivala, R.J. Smith, A. Lanzirotti, and J. Miklossy, *Synchrotron-based infrared and X-ray imaging shows focalized accumulation of Cu and Zn co-localized with beta-amyloid deposits in Alzheimer's disease.* J Struct Biol, 2006. **155**(1): p. 30-37.

73. Chandler, P., B.S. Kochupurakkal, S. Alam, A.L. Richardson, D.I. Soybel, and S.L. Kelleher, *Subtype-specific accumulation of intracellular zinc pools is associated with the malignant phenotype in breast cancer.* Mol Cancer, 2016. **15**: p. 2.
74. Cui, Y., S. Vogt, N. Olson, A.G. Glass, and T.E. Rohan, *Levels of zinc, selenium, calcium, and iron in benign breast tissue and risk of subsequent breast cancer.* Cancer Epidemiol Biomarkers Prev, 2007. **16**(8): p. 1682-1685.
75. Abnet, C.C., B. Lai, Y.L. Qiao, S. Vogt, X.M. Luo, P.R. Taylor, Z.W. Dong, S.D. Mark, and S.M. Dawsey, *Zinc concentration in esophageal biopsy specimens measured by x-ray fluorescence and esophageal cancer risk.* J Natl Cancer Inst, 2005. **97**(4): p. 301-306.
76. Ducic, T., T. Paunesku, S. Chen, M. Ninkovic, S. Speling, C. Wilke, B. Lai, and G. Woloschak, *Structural and elemental changes in glioblastoma cells in situ: complementary imaging with high resolution visible light- and X-ray microscopy.* Analyst, 2017. **142**(2): p. 356-365.
77. Song, H., X. Ren, and P. Liu, *Distribution and inhibition effect of Seleno-L-Methionine on 4T1 mouse mammary carcinoma.* Int J Physiol Pathophysiol Pharmacol, 2015. **7**(2): p. 76-86.
78. Leoni, L., A. Dhyani, P. La Riviere, S. Vogt, B. Lai, and B.B. Roman, *beta-Cell subcellular localization of glucose-stimulated Mn uptake by X-ray fluorescence microscopy: implications for pancreatic MRI.* Contrast Media Mol Imaging, 2011. **6**(6): p. 474-481.
79. Mihucz, V.G., F. Meirer, Z. Polgari, A. Reti, G. Pepponi, D. Ingerle, N. Szoboszlai, and C. Streli, *Iron overload of human colon adenocarcinoma cells studied by synchrotron-based X-ray techniques.* J Biol Inorg Chem, 2016. **21**(2): p. 241-249.
80. Ravel, B. and M. Newville, *ATHENA, ARTEMIS, HEPHAESTUS: data analysis for X-ray absorption spectroscopy using IFEFFIT.* J Synchrotron Radiat, 2005. **12**(Pt 4): p. 537-541.
81. Jansen, S.A., T. Paunesku, X. Fan, G.E. Woloschak, S. Vogt, S.D. Conzen, T. Krausz, G.M. Newstead, and G.S. Karczmar, *Ductal carcinoma in situ: X-ray fluorescence microscopy and dynamic contrast-enhanced MR imaging reveals gadolinium uptake within neoplastic mammary ducts in a murine model.* Radiology, 2009. **253**(2): p. 399-406.
82. Mustafi, D., S.C. Gleber, J. Ward, U. Dougherty, M. Zamora, E. Markiewicz, D.C. Binder, T. Antic, S. Vogt, G.S. Karczmar, and A. Oto, *IV Administered Gadodiamide Enters the Lumen of the Prostatic Glands: X-Ray Fluorescence Microscopy Examination of a Mouse Model.* AJR Am J Roentgenol, 2015. **205**(3): p. W313-319.
83. Mustafi, D., J. Ward, U. Dougherty, M. Bissonnette, J. Hart, S. Vogt, and G.S. Karczmar, *X-ray fluorescence microscopy demonstrates preferential accumulation of a vanadium-based magnetic resonance imaging contrast agent in murine colonic tumors.* Mol Imaging, 2015. **14**.
84. George, S.J., S.M. Webb, J.L. Abraham, and S.P. Cramer, *Synchrotron X-ray analyses demonstrate phosphate-bound gadolinium in skin in nephrogenic systemic fibrosis.* Br J Dermatol, 2010. **163**(5): p. 1077-1081.
85. Antony, S., J.B. Aitken, S. Vogt, B. Lai, T. Brown, L. Spiccia, and H.H. Harris, *X-ray fluorescence imaging of single human cancer cells reveals that the N-heterocyclic*

ligands of iodinated analogues of ruthenium anticancer drugs remain coordinated after cellular uptake. J Biol Inorg Chem, 2013. **18**(7): p. 845-853.

86. Thompson, C.M., J. Seiter, M.A. Chappell, R.V. Tappero, D.M. Proctor, M. Suh, J.C. Wolf, L.C. Haws, R. Vitale, L. Mittal, C.R. Kirman, S.M. Hays, and M.A. Harris, *Synchrotron-based imaging of chromium and gamma-H2AX immunostaining in the duodenum following repeated exposure to Cr(VI) in drinking water.* Toxicol Sci, 2015. **143**(1): p. 16-25.
87. Ramsay, S.C., N., de Jonge, MD., Howard, D. , *Examination of trafficking of phagocytosed colloid particles in neutrophils using synchrotron-based X-ray fluorescence microscopy (XFM).* J Biol Phys, 2011. **37**: p. 493-506.
88. Aryal, B.P., D. Gorman-Lewis, T. Paunesku, R.E. Wilson, B. Lai, S. Vogt, G.E. Woloschak, and M.P. Jensen, *Plutonium uptake and distribution in mammalian cells: molecular vs. polymeric plutonium.* Int J Radiat Biol, 2011. **87**(10): p. 1023-1032.
89. Gorman-Lewis, D., B.P. Aryal, T. Paunesku, S. Vogt, B. Lai, G.E. Woloschak, and M.P. Jensen, *Direct determination of the intracellular oxidation state of plutonium.* Inorg Chem, 2011. **50**(16): p. 7591-7597.
90. Jensen, M.P., B.P. Aryal, D. Gorman-Lewis, T. Paunesku, B. Lai, S. Vogt, and G.E. Woloschak, *Submicron hard X-ray fluorescence imaging of synthetic elements.* Anal Chim Acta, 2012. **722**: p. 21-28.
91. Jensen, M.P., D. Gorman-Lewis, B. Aryal, T. Paunesku, S. Vogt, P.G. Rickert, S. Seifert, B. Lai, G.E. Woloschak, and L. Soderholm, *An iron-dependent and transferrin-mediated cellular uptake pathway for plutonium.* Nat Chem Biol, 2011. **7**(8): p. 560-565.
92. Carozzi, V.A., A. Canta, and A. Chiorazzi, *Chemotherapy-induced peripheral neuropathy: What do we know about mechanisms?* Neurosci Lett, 2015. **596**: p. 90-107.
93. Chiorazzi, A., S. Semperboni, and P. Marmiroli, *Current View in Platinum Drug Mechanisms of Peripheral Neurotoxicity.* Toxics, 2015. **3**(3): p. 304-321.
94. Eljack, N.D., H.Y. Ma, J. Drucker, C. Shen, T.W. Hambley, E.J. New, T. Friedrich, and R.J. Clarke, *Mechanisms of cell uptake and toxicity of the anticancer drug cisplatin.* Metallomics, 2014. **6**(11): p. 2126-2133.
95. Gil, S., A. Carmona, G. Martinez-Criado, A. Leon, Y. Prezado, and M. Sabes, *Analysis of platinum and trace metals in treated glioma rat cells by X-ray fluorescence emission.* Biol Trace Elem Res, 2015. **163**(1-2): p. 177-183.
96. Hall, M.D., G.J. Foran, M. Zhang, P.J. Beale, and T.W. Hambley, *XANES determination of the platinum oxidation state distribution in cancer cells treated with platinum(IV) anticancer agents.* J Am Chem Soc, 2003. **125**(25): p. 7524-7525.
97. Refaat, T., D. West, S. El Achy, V. Parimi, J. May, L. Xin, K.R. Harris, W. Liu, M.B. Wanzer, L. Finney, et al., *Distribution of Iron Oxide Core-Titanium Dioxide Shell Nanoparticles in VX2 Tumor Bearing Rabbits Introduced by Two Different Delivery Modalities.* Nanomaterials, 2016. **6**(8).
98. Liu, T., I. Kempson, M. de Jonge, D.L. Howard, and B. Thierry, *Quantitative synchrotron X-ray fluorescence study of the penetration of transferrin-conjugated gold nanoparticles inside model tumour tissues.* Nanoscale, 2014. **6**(16): p. 9774-9782.

99. Nuester, J., M. Newville, and B.S. Twining, *Distributions of iron, phosphorus and sulfur along trichomes of the cyanobacteria Trichodesmium.* Metallomics, 2014. **6**(6): p. 1141-1149.
100. Labrenz, M., G.K. Druschel, T. Thomsen-Ebert, B. Gilbert, S.A. Welch, K.M. Kemner, G.A. Logan, R.E. Summons, G. De Stasio, P.L. Bond, B. Lai, S.D. Kelly, and J.F. Banfield, *Formation of sphalerite (ZnS) deposits in natural biofilms of sulfate-reducing bacteria.* Science, 2000. **290**(5497): p. 1744-1747.
101. Yu, R., B. Lai, S. Vogt, and K. Chandran, *Elemental profiling of single bacterial cells as a function of copper exposure and growth phase.* PLoS One, 2011. **6**(6): p. e21255.
102. Ingall, E.D., J.M. Diaz, A.F. Longo, M. Oakes, L. Finney, S. Vogt, B. Lai, P.L. Yager, B.S. Twining, and J.A. Brandes, *Role of biogenic silica in the removal of iron from the Antarctic seas.* Nat Commun, 2013. **4**: p. 1981.
103. Nayuki, K., B. Chen, R. Ohtomo, and Y. Kuga, *Cellular Imaging of Cadmium in Resin Sections of Arbuscular Mycorrhizas Using Synchrotron Micro X-ray Fluorescence.* Microbes and Environments, 2014. **29**(1): p. 60-66.
104. Terzano, R., M. Alfeld, K. Janssens, B. Vekemans, T. Schoonjans, L. Vincze, N. Tomasi, R. Pinton, and S. Cesco, *Spatially resolved (semi)quantitative determination of iron (Fe) in plants by means of synchrotron micro X-ray fluorescence.* Anal Bioanal Chem, 2013. **405**(10): p. 3341-3350.
105. Punshon, T., K. Hirschi, J. Yang, A. Lanzirotti, B. Lai, and M.L. Guerinot, *The role of CAX1 and CAX3 in elemental distribution and abundance in Arabidopsis seed.* Plant Physiol, 2012. **158**(1): p. 352-362.
106. Zhang, J., S. Tian, L. Lu, M.J. Shohag, H. Liao, and X. Yang, *Lead tolerance and cellular distribution in Elsholtzia splendens using synchrotron radiation micro-X-ray fluorescence.* J Hazard Mater, 2011. **197**: p. 264-271.
107. Lin, C.Y., J.E. Jakes, B.S. Donohoe, P.N. Ciesielski, H. Yang, S.C. Gleber, S. Vogt, S.Y. Ding, W.A. Peer, A.S. Murphy, M.C. McCann, M.E. Himmel, M.P. Tucker, and H. Wei, *Directed plant cell-wall accumulation of iron: embedding co-catalyst for efficient biomass conversion.* Biotechnol Biofuels, 2016. **9**: p. 225.
108. Zhang, L., S. Dong, and L. Zhu, *Fluorescent dyes of the esculetin and alizarin families respond to zinc ions ratiometrically.* Chemical Communications, 2007(19): p. 1891-1893.
109. Zhang, X., F. Wang, B. Liu, E.Y. Kelly, M.R. Servos, and J. Liu, *Adsorption of DNA Oligonucleotides by Titanium Dioxide Nanoparticles.* Langmuir, 2014. **30**(3): p. 839-845.
110. Paunesku, T., S. Vogt, J. Maser, B. Lai, and G. Woloschak, *X-ray fluorescence microprobe imaging in biology and medicine.* J Cell Biochem, 2006. **99**(6): p. 1489-1502.
111. Corezzi, S., L. Urbanelli, P. Cloetens, C. Emiliani, L. Helfen, S. Bohic, F. Elisei, and D. Fioretto, *Synchrotron-based X-ray fluorescence imaging of human cells labeled with CdSe quantum dots.* Anal Biochem, 2009. **388**(1): p. 33-39.
112. Russell-Jones, G., K. McTavish, J. McEwan, J. Rice, and D. Nowotnik, *Vitamin-mediated targeting as a potential mechanism to increase drug uptake by tumours.* J Inorg Biochem, 2004. **98**(10): p. 1625-1633.

113. Vadlapudi, A.D., R.K. Vadlapatla, and A.K. Mitra, *Sodium dependent multivitamin transporter (SMVT): a potential target for drug delivery.* Curr Drug Targets, 2012. **13**(7): p. 994-1003.
114. Townsend, S.A., G.D. Evrony, F.X. Gu, M.P. Schulz, R.H. Brown, and R. Langer, *Tetanus toxin C fragment-conjugated nanoparticles for targeted drug delivery to neurons.* Biomaterials, 2007. **28**(34): p. 5176-5184.
115. Kobayashi, H., H. Sakahara, K. Endo, M. Hosono, Z.S. Yao, S. Toyama, and J. Konishi, *COMPARISON OF THE CHASE EFFECTS OF AVIDIN, STREPTAVIDIN, NEUTRAVIDIN, AND AVIDIN-FERRITIN ON A RADIOLABELED BIOTINYLATED ANTITUMOR MONOCLONAL-ANTIBODY.* Japanese Journal of Cancer Research, 1995. **86**(3): p. 310-314.
116. Amblard, F., J.H. Cho, and R.F. Schinazi, *Cu(I)-Catalyzed Huisgen Azide–Alkyne 1,3-Dipolar Cycloaddition Reaction in Nucleoside, Nucleotide, and Oligonucleotide Chemistry.* Chemical Reviews, 2009. **109**(9): p. 4207-4220.
117. Meldal, M. and C.W. Tornøe, *Cu-Catalyzed Azide–Alkyne Cycloaddition.* Chemical Reviews, 2008. **108**(8): p. 2952-3015.
118. Cardiel, A.C., M.C. Benson, L.M. Bishop, K.M. Louis, J.C. Yeager, Y. Tan, and R.J. Hamers, *Chemically Directed Assembly of Photoactive Metal Oxide Nanoparticle Heterojunctions via the Copper-Catalyzed Azide-Alkyne Cycloaddition "Click" Reaction.* ACS Nano, 2012. **6**(1): p. 310-318.
119. Tao, P., Y. Li, A. Rungta, A. Viswanath, J. Gao, B.C. Benicewicz, R.W. Siegel, and L.S. Schadler, *TiO2 nanocomposites with high refractive index and transparency.* Journal of Materials Chemistry, 2011. **21**(46): p. 18623-18629.
120. Upadhyay, A.P., D.K. Behara, G.P. Sharma, M. Gyanprakash, R.G.S. Pala, and S. Sivakumar, *Fabricating Appropriate Band-Edge-Staggered Heterosemiconductors with Optically Activated Au Nanoparticles via Click Chemistry for Photoelectrochemical Water Splitting.* Acs Sustainable Chemistry & Engineering, 2016. **4**(9): p. 4511-4520.
121. Yadav, S.K., S.R. Madeshwaran, and J.W. Cho, *Synthesis of a hybrid assembly composed of titanium dioxide nanoparticles and thin multi-walled carbon nanotubes using "click chemistry".* Journal of Colloid and Interface Science, 2011. **358**(2): p. 471-476.
122. McRae, R., B. Lai, and C.J. Fahrni, *Copper redistribution in Atox1-deficient mouse fibroblast cells.* J Biol Inorg Chem, 2010. **15**(1): p. 99-105.
123. Dieterich, D.C., A.J. Link, J. Graumann, D.A. Tirrell, and E.M. Schuman, *Selective identification of newly synthesized proteins in mammalian cells using bioorthogonal noncanonical amino acid tagging (BONCAT).* Proc Natl Acad Sci U S A, 2006. **103**(25): p. 9482-9487.
124. Clark, P.M., J.F. Dweck, D.E. Mason, C.R. Hart, S.B. Buck, E.C. Peters, B.J. Agnew, and L.C. Hsieh-Wilson, *Direct in-gel fluorescence detection and cellular imaging of O-GlcNAc-modified proteins.* J Am Chem Soc, 2008. **130**(35): p. 11576-11577.
125. Salic, A. and T.J. Mitchison, *A chemical method for fast and sensitive detection of DNA synthesis in vivo.* Proc Natl Acad Sci U S A, 2008. **105**(7): p. 2415-2420.

126. Malalasekera, A.P., H. Wang, T.N. Samarakoon, D.N. Udukala, A.S. Yapa, R. Ortega, T.B. Shrestha, H. Alshetaiwi, E.J. McLaurin, D.L. Troyer, and S.H. Bossmann, *A nanobiosensor for the detection of arginase activity.* Nanomedicine, 2016.
127. Park, J., N.R. Kadasala, S.A. Abouelmagd, M.A. Castanares, D.S. Collins, A. Wei, and Y. Yeo, *Polymer-iron oxide composite nanoparticles for EPR-independent drug delivery.* Biomaterials, 2016. **101**: p. 285-295.
128. Paunesku, T., S. Gutiontov, K. Brown, and G.E. Woloschak, *Radiosensitization and Nanoparticles*, in *Nanotechnology-Based Precision Tools for the Detection and Treatment of Cancer*, C.A. Mirkin, et al., Editors. 2015, Springer International Publishing: Cham. p. 151-171.
129. Laha, D., A. Pramanik, J. Maity, A. Mukherjee, P. Pramanik, A. Laskar, and P. Karmakar, *Interplay between autophagy and apoptosis mediated by copper oxide nanoparticles in human breast cancer cells MCF7.* Biochimica et Biophysica Acta (BBA) - General Subjects, 2014. **1840**(1): p. 1-9.
130. Alarifi, S., D. Ali, S. Alkahtani, and R.S. Almeer, *ROS-Mediated Apoptosis and Genotoxicity Induced by Palladium Nanoparticles in Human Skin Malignant Melanoma Cells.* Oxid Med Cell Longev, 2017. **2017**: p. 8439098.
131. Nejdl, L., J. Kudr, A. Moulick, D. Hegerova, B. Ruttkay-Nedecky, J. Gumulec, K. Cihalova, K. Smerkova, S. Dostalova, S. Krizkova, M. Novotna, P. Kopel, and V. Adam, *Platinum nanoparticles induce damage to DNA and inhibit DNA replication.* PLoS One, 2017. **12**(7): p. e0180798.
132. Falaschetti, C.A., T. Paunesku, J. Kurepa, D. Nanavati, S.S. Chou, M. De, M. Song, J.T. Jang, A. Wu, V.P. Dravid, J. Cheon, J. Smalle, and G.E. Woloschak, *Negatively charged metal oxide nanoparticles interact with the 20S proteasome and differentially modulate its biologic functional effects.* ACS Nano, 2013. **7**(9): p. 7759-7772.
133. Lundqvist, M., J. Stigler, T. Cedervall, T. Berggård, M.B. Flanagan, I. Lynch, G. Elia, and K. Dawson, *The Evolution of the Protein Corona around Nanoparticles: A Test Study.* ACS Nano, 2011. **5**(9): p. 7503-7509.
134. McBride, W.H., K.S. Iwamoto, R. Syljuasen, M. Pervan, and F. Pajonk, *The role of the ubiquitin//proteasome system in cellular responses to radiation.* Oncogene, 2003. **22**(37): p. 5755-5773.
135. Li, Y.-J., A.L. Perkins, Y. Su, Y. Ma, L. Colson, D.A. Horne, and Y. Chen, *Gold nanoparticles as a platform for creating a multivalent poly-SUMO chain inhibitor that also augments ionizing radiation.* Proceedings of the National Academy of Sciences, 2012. **109**(11): p. 4092-4097.
136. Yasui, H., R. Takeuchi, M. Nagane, S. Meike, Y. Nakamura, T. Yamamori, Y. Ikenaka, Y. Kon, H. Murotani, M. Oishi, Y. Nagasaki, and O. Inanami, *Radiosensitization of tumor cells through endoplasmic reticulum stress induced by PEGylated nanogel containing gold nanoparticles.* Cancer Letters, 2014. **347**(1): p. 151-158.
137. Yamamori, T., S. Meike, M. Nagane, H. Yasui, and O. Inanami, *ER stress suppresses DNA double-strand break repair and sensitizes tumor cells to ionizing radiation by stimulating proteasomal degradation of Rad51.* FEBS Letters, 2013. **587**(20): p. 3348-3353.

138. Wilson, R., Z. Xiaojing, G. Linghong, S. Andrew, H. Xiuying, X. Yeping, G. Sunil, P. Samir, S. Xuejun, C. Jie, M. Ronald, and Z.X. James, *Gold nanoparticle sensitize radiotherapy of prostate cancer cells by regulation of the cell cycle.* Nanotechnology, 2009. **20**(37): p. 375101.
139. Mirjolet, C., A.L. Papa, G. Crehange, O. Raguin, C. Seignez, C. Paul, G. Truc, P. Maingon, and N. Millot, *The radiosensitization effect of titanate nanotubes as a new tool in radiation therapy for glioblastoma: a proof-of-concept.* Radiother Oncol, 2013. **108**(1): p. 136-142.
140. Mackey, M.A. and M.A. El-Sayed, *Chemosensitization of Cancer Cells via Gold Nanoparticle-Induced Cell Cycle Regulation.* Photochemistry and photobiology, 2014. **90**(2): p. 306-312.
141. Wolfe, T., D. Chatterjee, J. Lee, J.D. Grant, S. Bhattarai, R. Tailor, G. Goodrich, P. Nicolucci, and S. Krishnan, *Targeted gold nanoparticles enhance sensitization of prostate tumors to megavoltage radiation therapy in vivo.* Nanomedicine, 2015. **11**(5): p. 1277-1283.
142. Parkin, D.M., *The global health burden of infection-associated cancers in the year 2002.* International Journal of Cancer, 2006. **118**(12): p. 3030-3044.
143. Moore, P.S. and Y. Chang, *Why do viruses cause cancer? Highlights of the first century of human tumour virology.* Nature reviews. Cancer, 2010. **10**(12): p. 878-889.
144. Morales-Sanchez, A. and E.M. Fuentes-Panana, *Human viruses and cancer.* Viruses, 2014. **6**(10): p. 4047-4079.
145. Zheng, Z.M. and C.C. Baker, *Papillomavirus genome structure, expression, and post-transcriptional regulation.* Front Biosci, 2006. **11**: p. 2286-2302.
146. Trottier, H. and A.N. Burchell, *Epidemiology of Mucosal Human Papillomavirus Infection and Associated Diseases.* Public Health Genomics, 2009. **12**(5-6): p. 291-307.
147. zur Hausen, H., *Papillomaviruses and cancer: from basic studies to clinical application.* Nat Rev Cancer, 2002. **2**(5): p. 342-350.
148. Giampieri, S. and A. Storey, *Repair of UV-induced thymine dimers is compromised in cells expressing the E6 protein from human papillomaviruses types 5 and 18.* British Journal of Cancer, 2004. **90**(11): p. 2203-2209.
149. Longworth, M.S. and L.A. Laimins, *Pathogenesis of human papillomaviruses in differentiating epithelia.* Microbiol Mol Biol Rev, 2004. **68**.
150. Suzich, J.A., S.J. Ghim, F.J. Palmer-Hill, W.I. White, J.K. Tamura, J.A. Bell, J.A. Newsome, A.B. Jenson, and R. Schlegel, *Systemic immunization with papillomavirus L1 protein completely prevents the development of viral mucosal papillomas.* Proceedings of the National Academy of Sciences, 1995. **92**(25): p. 11553-11557.
151. Levine, A.J., *p53, the Cellular Gatekeeper for Growth and Division.* Cell, 1997. **88**(3): p. 323-331.
152. Hollstein, M., D. Sidransky, B. Vogelstein, and C.C. Harris, *p53 mutations in human cancers.* Science, 1991. **253**(5015): p. 49.
153. Münger, K., B.A. Werness, N. Dyson, W.C. Phelps, E. Harlow, and P.M. Howley, *Complex formation of human papillomavirus E7 proteins with the retinoblastoma tumor suppressor gene product.* The EMBO Journal, 1989. **8**(13): p. 4099-4105.

154. Song, S., A. Liem, J.A. Miller, and P.F. Lambert, *Human Papillomavirus Types 16 E6 and E7 Contribute Differently to Carcinogenesis.* Virology, 2000. **267**(2): p. 141-150.
155. Khidr, L. and P.L. Chen, *RB, the conductor that orchestrates life, death and differentiation.* Oncogene, 2006. **25**(38): p. 5210-5219.
156. Kessis, T.D., D.C. Connolly, L. Hedrick, and K.R. Cho, *Expression of HPV16 E6 or E7 increases integration of foreign DNA.* Oncogene, 1996. **13**.
157. Yu, T., M.J. Ferber, T.H. Cheung, T.K. Chung, Y.F. Wong, and D.I. Smith, *The role of viral integration in the development of cervical cancer.* Cancer Genet Cytogenet, 2005. **158**.
158. Williams Vonetta, M., M. Filippova, V. Filippov, J. Payne Kimberly, and P. Duerksen-Hughes, *Human Papillomavirus Type 16 E6* Induces Oxidative Stress and DNA Damage.* J Virol, 2014. **88**.
159. Sakakibara, N., R. Mitra, and A.A. McBride, *The papillomavirus E1 helicase activates a cellular DNA damage response in viral replication foci.* J Virol, 2011. **85**.
160. Moody, C.A. and L.A. Laimins, *Human Papillomaviruses Activate the ATM DNA Damage Pathway for Viral Genome Amplification upon Differentiation.* PLOS Pathogens, 2009. **5**(10): p. e1000605.
161. Spardy, N., K. Covella, E. Cha, E.E. Hoskins, S.I. Wells, A. Duensing, and S. Duensing, *HPV-16 E7 attenuates DNA damage checkpoint control by increasing the proteolytic turnover of claspin.* Cancer Research, 2009. **69**(17): p. 7022-7029.
162. King, L.E., J.C. Fisk, E.S. Dornan, M.M. Donaldson, T. Melendy, and I.M. Morgan, *Human papillomavirus E1 and E2 mediated DNA replication is not arrested by DNA damage signalling.* Virology, 2010. **406**(1): p. 95-102.
163. Schmitz, M., C. Driesch, L. Jansen, I.B. Runnebaum, and M. Dürst, *Non-Random Integration of the HPV Genome in Cervical Cancer.* PLoS One, 2012. **7**(6): p. e39632.
164. Dall, K.L., C.G. Scarpini, I. Roberts, D.M. Winder, M.A. Stanley, B. Muralidhar, M.T. Herdman, M.R. Pett, and N. Coleman, *Characterization of Naturally Occurring HPV16 Integration Sites Isolated from Cervical Keratinocytes under Noncompetitive Conditions.* Cancer Research, 2008. **68**(20): p. 8249.
165. Akagi, K., L. Jingfeng, R. Tatevik, and H.P.N. Broutian, *Genome-wide analysis of HPV integration in human cancers reveals recurrent, focal genomic instability.* Genome Res, 2014. **24**.
166. Duensing, S. and K. Münger, *The Human Papillomavirus Type 16 E6 and E7 Oncoproteins Independently Induce Numerical and Structural Chromosome Instability.* Cancer Research, 2002. **62**(23): p. 7075.
167. Duensing, S., L.Y. Lee, A. Duensing, J. Basile, S.-o. Piboonniyom, S. Gonzalez, C.P. Crum, and K. Münger, *The human papillomavirus type 16 E6 and E7 oncoproteins cooperate to induce mitotic defects and genomic instability by uncoupling centrosome duplication from the cell division cycle.* Proceedings of the National Academy of Sciences, 2000. **97**(18): p. 10002-10007.
168. Jemal, A., F. Bray, M.M. Center, J. Ferlay, E. Ward, and D. Forman, *Global cancer statistics.* CA Cancer J Clin, 2011. **61**(2): p. 69-90.
169. Humans, I.W.G.o.t.E.o.C.R.t., *Human papillomaviruses.* Iarc Monographs on the Evaluation of Carcinogenic Risks to Humans, 1995. **64**: p. 1-378.

170. Adelstein, D.J., *Redefining the role of induction chemotherapy in head and neck cancer.* J Clin Oncol, 2008. **26**(19): p. 3117-3119.
171. Chaturvedi, A.K., E.A. Engels, W.F. Anderson, and M.L. Gillison, *Incidence Trends for Human Papillomavirus–Related and –Unrelated Oral Squamous Cell Carcinomas in the United States.* Journal of Clinical Oncology, 2008. **26**(4): p. 612-619.
172. Chaturvedi, A.K., E.A. Engels, R.M. Pfeiffer, B.Y. Hernandez, W. Xiao, E. Kim, B. Jiang, M.T. Goodman, M. Sibug-Saber, W. Cozen, et al., *Human Papillomavirus and Rising Oropharyngeal Cancer Incidence in the United States.* Journal of Clinical Oncology, 2011. **29**(32): p. 4294-4301.
173. Pytynia, K.B., K.R. Dahlstrom, and E.M. Sturgis, *Epidemiology of HPV-associated oropharyngeal cancer.* Oral Oncology, 2014. **50**(5): p. 380-386.
174. The Cancer Genome Atlas, N., *Comprehensive genomic characterization of head and neck squamous cell carcinomas.* Nature, 2015. **517**(7536): p. 576-582.
175. Shi, W., H. Kato, B. Perez-Ordonez, M. Pintilie, S. Huang, A. Hui, B. O'Sullivan, J. Waldron, B. Cummings, J. Kim, et al., *Comparative Prognostic Value of HPV16 E6 mRNA Compared With In Situ Hybridization for Human Oropharyngeal Squamous Carcinoma.* Journal of Clinical Oncology, 2009. **27**(36): p. 6213-6221.
176. O'Sullivan, B., S.H. Huang, L.L. Siu, J. Waldron, H. Zhao, B. Perez-Ordonez, I. Weinreb, J. Kim, J. Ringash, A. Bayley, et al., *Deintensification Candidate Subgroups in Human Papillomavirus–Related Oropharyngeal Cancer According to Minimal Risk of Distant Metastasis.* Journal of Clinical Oncology, 2013. **31**(5): p. 543-550.
177. Bratman, S.V., J.P. Bruce, B. O'Sullivan, and et al., *Human papillomavirus genotype association with survival in head and neck squamous cell carcinoma.* JAMA Oncology, 2016. **2**(6): p. 823-826.
178. Ndiaye, C., M. Mena, L. Alemany, M. Arbyn, X. Castellsagué, L. Laporte, F.X. Bosch, S. de Sanjosé, and H. Trottier, *HPV DNA, E6/E7 mRNA, and p16INK4a detection in head and neck cancers: a systematic review and meta-analysis.* The Lancet Oncology, 2014. **15**(12): p. 1319-1331.
179. Andl, T., T. Kahn, A. Pfuhl, T. Nicola, R. Erber, C. Conradt, W. Klein, M. Helbig, A. Dietz, H. Weidauer, and F.X. Bosch, *Etiological Involvement of Oncogenic Human Papillomavirus in Tonsillar Squamous Cell Carcinomas Lacking Retinoblastoma Cell Cycle Control.* Cancer Research, 1998. **58**(1): p. 5.
180. Mellin, H., S. Friesland, R. Lewensohn, T. Dalianis, and E. Munck-Wikland, *Human papillomavirus (HPV) DNA in tonsillar cancer: Clinical correlates, risk of relapse, and survival.* International Journal of Cancer, 2000. **89**(3): p. 300-304.
181. Fakhry, C., W.H. Westra, S. Li, A. Cmelak, J.A. Ridge, H. Pinto, A. Forastiere, and M.L. Gillison, *Improved Survival of Patients With Human Papillomavirus–Positive Head and Neck Squamous Cell Carcinoma in a Prospective Clinical Trial.* JNCI: Journal of the National Cancer Institute, 2008. **100**(4): p. 261-269.
182. Ang, K.K., J. Harris, R. Wheeler, R. Weber, D.I. Rosenthal, P.F. Nguyen-Tân, W.H. Westra, C.H. Chung, R.C. Jordan, C. Lu, et al., *Human Papillomavirus and Survival of Patients with Oropharyngeal Cancer.* New England Journal of Medicine, 2010. **363**(1): p. 24-35.

183. Cmelak, A.J., *Current issues in combined modality therapy in locally advanced head and neck cancer.* Critical Reviews in Oncology / Hematology, 2012. **84**(2): p. 261-273.
184. O'Rorke, M.A., M.V. Ellison, L.J. Murray, M. Moran, J. James, and L.A. Anderson, *Human papillomavirus related head and neck cancer survival: A systematic review and meta-analysis.* Oral Oncology, 2012. **48**(12): p. 1191-1201.
185. Fakhry, C. and M.L. Gillison, *Clinical Implications of Human Papillomavirus in Head and Neck Cancers.* Journal of clinical oncology : official journal of the American Society of Clinical Oncology, 2006. **24**(17): p. 2606-2611.
186. Rischin, D., R.J. Young, R. Fisher, S.B. Fox, Q.-T. Le, L.J. Peters, B. Solomon, J. Choi, B. O'Sullivan, L.M. Kenny, and G.A. McArthur, *Prognostic Significance of p16INK4A and Human Papillomavirus in Patients With Oropharyngeal Cancer Treated on TROG 02.02 Phase III Trial.* Journal of Clinical Oncology, 2010. **28**(27): p. 4142-4148.
187. Perrone, F., S. Suardi, E. Pastore, P. Casieri, M. Orsenigo, S. Caramuta, G. Dagrada, M. Losa, L. Licitra, P. Bossi, et al., *Molecular and Cytogenetic Subgroups of Oropharyngeal Squamous Cell Carcinoma.* Clinical Cancer Research, 2006. **12**(22): p. 6643.
188. Arenz, A., F. Ziemann, C. Mayer, A. Wittig, K. Dreffke, S. Preising, S. Wagner, J.-P. Klussmann, R. Engenhart-Cabillic, and C. Wittekindt, *Increased radiosensitivity of HPV-positive head and neck cancer cell lines due to cell cycle dysregulation and induction of apoptosis.* Strahlentherapie und Onkologie, 2014. **190**(9): p. 839-846.
189. Kimple, R.J., M.A. Smith, G.C. Blitzer, A.D. Torres, J.A. Martin, R.Z. Yang, C.R. Peet, L.D. Lorenz, K.P. Nickel, A.J. Klingelhutz, P.F. Lambert, and P.M. Harari, *Enhanced Radiation Sensitivity in HPV-Positive Head and Neck Cancer.* Cancer Research, 2013. **73**(15): p. 4791.
190. Braakhuis, B.J.M., A. Senft, R. de Bree, J. de Vries, B. Ylstra, J. Cloos, D.J. Kuik, C.R. Leemans, and R.H. Brakenhoff, *Expression profiling and prediction of distant metastases in head and neck squamous cell carcinoma.* Journal of Clinical Pathology, 2006. **59**(12): p. 1254-1260.
191. Boscolo-Rizzo, P., A. Del Mistro, F. Bussu, V. Lupato, L. Baboci, G. Almadori, M.C. Da Mosto, and G. Paludetti, *New insights into human papillomavirus-associated head and neck squamous cell carcinoma.* Acta Otorhinolaryngologica Italica, 2013. **33**(2): p. 77-87.
192. Psyrri, A., C. Sasaki, M. Vassilakopoulou, G. Dimitriadis, and T. Rampias, *Future Directions in Research, Treatment and Prevention of HPV-Related Squamous Cell Carcinoma of the Head and Neck.* Head and Neck Pathology, 2012. **6**(Suppl 1): p. 121-128.
193. Brotherston, D.C., I. Poon, T. Le, M. Leung, A. Kiss, J. Ringash, J. Balogh, J. Lee, and J.R. Wright, *Patient preferences for oropharyngeal cancer treatment de-escalation.* Head & Neck, 2013. **35**(2): p. 151-159.
194. Achary, M.P., W. Jaggernauth, E. Gross, A. Alfieri, H.P. Klinger, and B. Vikram, *Cell lines from the same cervical carcinomabut with different radiosensitivities exhibit different cDNA microarray patterns of gene expression.* Cytogenetic and Genome Research, 2000. **91**(1-4): p. 39-43.
195. Fosmire, G.J., *Zinc toxicity.* Am J Clin Nutr, 1990. **51**(2): p. 225-227.

196. Prasad, A.S., F.W.J. Beck, L. Endre, W. Handschu, M. Kukuruga, and G. Kumar, *Zinc deficiency affects cell cycle and deoxythymidine kinase gene expression in HUT-78 cells.* Journal of Laboratory and Clinical Medicine, 1996. **128**(1): p. 51-60.
197. Paski, S.C. and Z. Xu, *Growth factor stimulated cell proliferation is accompanied by an elevated labile intracellular pool of zinc in 3T3 cells.* Canadian Journal of Physiology and Pharmacology, 2002. **80**(8): p. 790-795.
198. Takeda, A., K. Goto, and S. Okada, *Zinc depletion suppresses tumor growth in mice.* Biological Trace Element Research, 1997. **59**(1): p. 23-29.
199. DeWys, W. and W. Pories, *Inhibition of a spectrum of animal tumors by dietary zinc deficiency.* J Natl Cancer Inst, 1972. **48**(2): p. 375-381.
200. Stefanidou, M., C. Maravelias, A. Dona, and C. Spiliopoulou, *Zinc: a multipurpose trace element.* Archives of Toxicology, 2005. **80**(1): p. 1.
201. Fuwa, K., W.E.C. Wacker, R. Druyan, A.F. Bartholomay, and B.L. Vallee, *NUCLEIC ACIDS AND METALS, II: TRANSITION METALS AS DETERMINANTS OF THE CONFORMATION OF RIBONUCLEIC ACIDS.* Proceedings of the National Academy of Sciences of the United States of America, 1960. **46**(10): p. 1298-1307.
202. Dutta, A., M. Schaller, A.T. Franco, K. Sankavaram, B.J. Grattan, and H.C. Freake, *Zinc retention differs between primary and transformed cells in response to zinc deprivation.* The Journal of Nutritional Biochemistry, 2010. **21**(2): p. 162-170.
203. Gurusamy, K. and B.R. Davidson, *Trace element concentration in metastatic liver disease: a systematic review.* Journal of trace elements in medicine and biology : organ of the Society for Minerals and Trace Elements (GMS), 2007. **21**(3): p. 169-177.
204. Gupta, S.K., S.P. Singh, and V.K. Shukla, *Copper, zinc, and Cu/Zn ratio in carcinoma of the gallbladder.* Journal of Surgical Oncology, 2005. **91**(3): p. 204-208.
205. Zaichick, V.Y., T.V. Sviridova, and S.V. Zaichick, *Zinc in the human prostate gland: Normal, hyperplastic and cancerous.* International Urology and Nephrology, 1997. **29**(5): p. 565-574.
206. Henshall, S.M., D.E.H. Afar, K.K. Rasiah, L.G. Horvath, K. Gish, I. Caras, V. Ramakrishnan, M. Wong, U. Jeffry, J.G. Kench, et al., *Expression of the zinc transporter ZnT4 is decreased in the progression from early prostate disease to invasive prostate cancer[star].* Oncogene, 2003. **22**(38): p. 6005-6012.
207. Cunzhi, H., J. Jiexian, Z. Xianwen, G. Jingang, Z. Shumin, and D. Lili, *Serum and tissue levels of six trace elements and copper/zinc ratio in patients with cervical cancer and uterine myoma.* Biological Trace Element Research, 2003. **94**(2): p. 113-122.
208. Franklin, R.B., B. Milon, P. Feng, and L.C. Costello, *Zinc and zinc transporters in normal prostate function and the pathogenesis of prostate cancer.* Frontiers in Biosciences, 2005. **10**.
209. Liang, J.-Y., Y.-Y. Liu, J. Zou, R.B. Franklin, L.C. Costello, and P. Feng, *Inhibitory effect of zinc on human prostatic carcinoma cell growth.* The Prostate, 1999. **40**(3): p. 200-207.
210. Diez, M., M. Arroyo, F.J. Cerdan, M. Munoz, M.A. Martin, and J.L. Balibrea, *Serum and tissue trace metal levels in lung cancer.* Oncology, 1989. **46**(4): p. 230-234.

211. Chakravarty, P.K., A. Ghosh, and J.R. Chowdhury, *Zinc in human malignancies.* Neoplasma, 1986. **33**(1): p. 85-90.
212. Mulay, I.L., R. Roy, B.E. Knox, N.H. Suhr, and W.E. Delaney, *Trace-metal analysis of cancerous and noncancerous human tissues.* J Natl Cancer Inst, 1971. **47**(1): p. 1-13.
213. Cui, Y., S. Vogt, N. Olson, A.G. Glass, and T.E. Rohan, *Levels of Zinc, Selenium, Calcium, and Iron in Benign Breast Tissue and Risk of Subsequent Breast Cancer.* Cancer Epidemiology Biomarkers & Prevention, 2007. **16**(8): p. 1682.
214. Taylor, C.G., W.J. Bettger, and T.M. Bray, *Effect of dietary zinc or copper deficiency on the primary free radical defense system in rats.* J Nutr, 1988. **118**(5): p. 613-621.
215. Uzzo, R.G., P. Leavis, W. Hatch, V.L. Gabai, N. Dulin, N. Zvartau, and V.M. Kolenko, *Zinc Inhibits Nuclear Factor-κB Activation and Sensitizes Prostate Cancer Cells to Cytotoxic Agents.* Clinical Cancer Research, 2002. **8**(11): p. 3579.
216. Truong-Tran, A.Q., L.H. Ho, F. Chai, and P.D. Zalewski, *Cellular zinc fluxes and the regulation of apoptosis/gene-directed cell death.* J Nutr, 2000. **130**(5S Suppl): p. 1459S-1466S.
217. Liang, J.Y., Y.Y. Liu, J. Zou, R.B. Franklin, L.C. Costello, and P. Feng, *Inhibitory effect of zinc on human prostatic carcinoma cell growth.* Prostate, 1999. **40**.
218. Feng, P., T.L. Li, Z.X. Guan, R.B. Franklin, and L.C. Costello, *Direct effect of zinc on mitochondrial apoptogenesis in prostate cells.* Prostate, 2002. **52**.
219. Chaturvedi, U.C., R. Shrivastava, and R.K. Upreti, *Viral infections and trace elements: A complex interaction.* Current Science, 2004. **87**(11): p. 1536-1554.
220. Yeung, K.S., N.A. Meanwell, Z. Qiu, D. Hernandez, S. Zhang, F. McPhee, S. Weinheimer, J.M. Clark, and J.W. Janc, *Structure-activity relationship studies of a bisbenzimidazole-based, Zn(2+)-dependent inhibitor of HCV NS3 serine protease.* Bioorg Med Chem Lett, 2001. **11**(17): p. 2355-2359.
221. Williams, M.C., R.J. Gorelick, and K. Musier-Forsyth, *Specific zinc-finger architecture required for HIV-1 nucleocapsid protein's nucleic acid chaperone function.* Proc Natl Acad Sci U S A, 2002. **99**(13): p. 8614-8619.
222. Barbosa, M.S., D.R. Lowy, and J.T. Schiller, *Papillomavirus polypeptides E6 and E7 are zinc-binding proteins.* J Virol, 1989. **63**(3): p. 1404-1407.
223. Degenkolbe, R., P. Gilligan, S. Gupta, and H.U. Bernard, *Chelating agents stabilize the monomeric state of the zinc binding human papillomavirus 16 E6 oncoprotein.* Biochemistry, 2003. **42**(13): p. 3868-3873.
224. Cho, Y., S. Gorina, P.D. Jeffrey, and N.P. Pavletich, *Crystal structure of a p53 tumor suppressor-DNA complex: understanding tumorigenic mutations.* Science, 1994. **265**(5170): p. 346.
225. Huang, S.H., W. Xu, J. Waldron, L. Siu, X. Shen, L. Tong, J. Ringash, A. Bayley, J. Kim, A. Hope, et al., *Refining American Joint Committee on Cancer/Union for International Cancer Control TNM Stage and Prognostic Groups for Human Papillomavirus–Related Oropharyngeal Carcinomas.* Journal of Clinical Oncology, 2015. **33**(8): p. 836-845.
226. Weinberger, P.M., Z. Yu, B.G. Haffty, D. Kowalski, M. Harigopal, J. Brandsma, C. Sasaki, J. Joe, R.L. Camp, D.L. Rimm, and A. Psyrri, *Molecular Classification Identifies a Subset of Human Papillomavirus–Associated Oropharyngeal Cancers With Favorable Prognosis.* Journal of Clinical Oncology, 2006. **24**(5): p. 736-747.

227. Galloway, T.J., Q.E. Zhang, P.F. Nguyen-Tan, D.I. Rosenthal, D. Soulieres, A. Fortin, C.L. Silverman, M.E. Daly, J.A. Ridge, J.A. Hammond, and Q.T. Le, *Prognostic Value of p16 Status on the Development of a Complete Response in Involved Oropharynx Cancer Neck Nodes After Cisplatin-Based Chemoradiation: A Secondary Analysis of NRG Oncology RTOG 0129.* Int J Radiat Oncol Biol Phys, 2016. **96**(2): p. 362-371.
228. Westra, W.H., *Detection of human papillomavirus (HPV) in clinical samples: Evolving methods and strategies for the accurate determination of HPV status of head and neck carcinomas.* Oral Oncology, 2014. **50**(9): p. 771-779.
229. Giuliani, L., A. Coletti, K. SyrjÄNen, C. Favalli, and M. Ciotti, *Comparison of DNA Sequencing and Roche Linear Array® in Human papillomavirus (HPV) Genotyping.* Anticancer Research, 2006. **26**(5B): p. 3939-3941.
230. Ward, M.J., T. Mellows, S. Harris, A. Webb, N.N. Patel, H.J. Cox, K. Piper, C.H. Ottensmeier, G.J. Thomas, and E.V. King, *Staging and treatment of oropharyngeal cancer in the human papillomavirus era.* Head & Neck, 2015. **37**(7): p. 1002-1013.
231. Wierzbicka, M., K. Szyfter, P. Milecki, K. Skladowski, and R. Ramlau, *The rationale for HPV-related oropharyngeal cancer de-escalation treatment strategies.* Contemp Oncol (Pozn), 2015. **19**(4): p. 313-322.
232. Vogt, S., *MAPS : A set of software tools for analysis and visualization of 3D X-ray fluorescence data sets.* J. Phys. IV France, 2003. **104**: p. 635-638.